



**Ana Carolina Costa Amorim**

Bachelor of Science

**Development of a Osirix plug-in for non-gaussian  
diffusion MRI data: application to Breast.**

Dissertation submitted in partial fulfillment  
of the requirements for the degree of

Master of Science in  
**Biomedical Engineering**

Adviser: Hugo Alexandre Ferreira, Assistant Professor, Faculty of  
Sciences of the University of Lisbon

Co-adviser: Rita G. Nunes, Assistant Investigator, Faculty of Sci-  
ences of the University of Lisbon

Examination Committee

Chairperson: Assistant Professor Carla Quintão  
Raporteurs: Adjunt Professor Margarida Ribeiro  
Assistant Professor Hugo Ferreira



FACULDADE DE  
CIÊNCIAS E TECNOLOGIA  
UNIVERSIDADE NOVA DE LISBOA

September, 2016



## **Development of a Osirix plug-in for non-gaussian diffusion MRI data: application to Breast.**

Copyright © Ana Carolina Costa Amorim, Faculty of Sciences and Technology, NOVA University of Lisbon.

The Faculty of Sciences and Technology and the NOVA University of Lisbon have the right, perpetual and without geographical boundaries, to file and publish this dissertation through printed copies reproduced on paper or on digital form, or by any other means known or that may be invented, and to disseminate through scientific repositories and admit its copying and distribution for non-commercial, educational or research purposes, as long as credit is given to the author and editor.



*To my mom.*



## ACKNOWLEDGEMENTS

First and foremost, I would like to express my greatest gratitude to my adviser and co-adviser, Prof. Hugo Ferreira and Prof. Rita G. Nunes. Thank you for having the patience and listening to all of my doubts, questions and struggles. Thank you so much for giving me the opportunity to work with you, I truly enjoyed it!

Secondly, I would also like to give a big thank you to Filipa Borlinhas and Luísa Nogueira, who gave me images to work with and also valuable tips and information.

Thank you also to everyone in IBEB who helped me throughout these months. I really enjoyed the companionship, the amazing team work spirit, the long lunches and, in the last weeks, dinners and the elucidating discussions on how to write a thesis. It really motivated me to keep coming back to IBEB and work.

On a more personal note, I would like to thank everyone who helped me through all of these years. A big thank you to Patricia Paulino, who even though I only met two years ago, helped me so much and is someone I can call a good friend. I would also like to thank everyone who lived with me and had to deal with me, specially to my best friends Raquel Martins and Marina Teixeira. And of course, I want to give a shoutout to my second family, Mario, Ramalho, Miguel, Boiça, JR, Barreto and Vasco.

There is also an association that I have been a part of called BEST to which I would like to say a big thank you. Every single person in it is amazing and even though I have only been there for one year, I will miss it deeply.

Last but not least, I want to give the biggest of thank you to my mother. She is the one that always tells me that I can accomplish anything. Thank you so much for believing in me and for all of the amazing and wise advices. You are not only my mother but also my best friend.





## ABSTRACT

---

Breast cancer is the second leading cause of death by cancer and is the second type of cancer that is the most common among women, causing the death of 1500 women, every year, in Portugal. Over the past decades, with the improvement of imaging techniques and therapeutics, breast cancer mortality rate has been decreasing substantially. One of the imaging techniques used is diffusion-weighted imaging (DWI), which is the magnetic resonance imaging method that is the most sensitive in detecting invasive breast cancer. There are several extensions of this technique that can be based on the premise that the environment is not homogeneous (non-Gaussian models).

The non-Gaussian models, take into account the presence of barriers and compartments that restrict the water molecules movement in the biological tissues, allowing the distinction between malignant and benign lesions in DWI. Taking into account that diffusion-weighted imaging is a non invasive method, the diagnosis through the application of these models can become an alternative to biopsy.

The main goal of this dissertation was the development of a OsiriX plug-in that performs the non-Gaussian diffusion analysis of DWI in magnetic resonance imaging data. Five non-Gaussian diffusion models were implemented in the application: diffusion kurtosis imaging, intravoxel incoherent motion, gamma distribution, truncated and stretched-exponential. Parametric maps and region-of interest (ROI) parametric values were obtained for each model. In order to fit the various non-Gaussian diffusion models, the Levenberg-Marquardt algorithm was used. This algorithm finds coefficients  $x$  to best fit the nonlinear function to the data. The  $x$  coefficients results in parametric maps that are able to identify the tumour and also distinguish between malignant and benign lesions provided a comparison with the literature. During the application development, these functionalities were also used to study the dependence of fitted parameters on the number of b-values used and on the image noise.

An interface was developed with Objective-C on Xcode for OsiriX where the user gets to choose from five diffusion models in order to obtain parameric maps or values. It also informs on the goodness of fit and it provides fitting plots of the data. The references of the models and extra information are also available in an help button.

Finally, the application was tested successfully with breast DWI images of benign and

---

malignant tumors.

**Keywords:** Diffusion Kurtosis Imaging, Intravoxel Incoherent Motion, Gamma Distribution, Truncated, Stretched-Exponential, Plug-in, OsiriX

---

## RESUMO

---

O cancro da mama é a segunda causa de morte por cancro e é o segundo tipo de cancro mais comum entre as mulheres, matando todos os anos 1500 mulheres só em Portugal. Nos últimos anos, com a melhoria das técnicas de imagem e terapêutica, a taxa de mortalidade do cancro da mama tem diminuído substancialmente. Uma das técnicas de imagem usadas é a imagem ponderada em difusão (DWI), que é o método da imagem por ressonância magnética mais sensível na detecção de cancro da mama invasivo. Existem várias extensões desta técnica que se baseiam na premissa que o ambiente não é homogéneo (modelos não-Gaussianos).

Os modelos não-Gaussianos, têm em conta a presença de barreiras e compartimentos que restringem o movimento das moléculas de água nos tecidos biológicos, permitindo assim a distinção entre lesões malignas e benignas numa imagem ponderada em difusão. Sendo a imagem ponderada em difusão um método não invasivo de imagem por ressonância magnética, o diagnóstico através da aplicação destes modelos pode se tornar uma alternativa à biópsia.

O principal objectivo desta dissertação foi o desenvolvimento de um *plug-in* para o OsiriX que efectue a análise da difusão não-Gaussiana em dados de imagens de ressonância magnética. Foram implementados cinco modelos de difusão não-Gaussianos na aplicação: imagem por curtose de difusão, movimento incoerente intravoxel, distribuição gama, truncado e “stretched-exponential”. Foram obtidos mapas paramétricos e valores paramétricos correspondentes à região de interesse (ROI). De forma a fazer o ajuste dos vários modelos de difusão não Gaussianos, foi aplicado o algoritmo Levenberg-Marquardt. Este algoritmo procura coeficientes de  $x$  de forma a fazer o melhor ajuste da função não linear aos dados. Os coeficientes de  $x$  resultam em mapas paramétricos que conseguem identificar o tumor e também distinguir lesões malignas de benignas, fornecendo comparação com a literatura. Durante o desenvolvimento da aplicação, estas funcionalidades foram testadas de forma a estudar a dependência dos parâmetros ajustados aos valores de  $b$  usados e relação sinal-ruído.

Foi desenvolvida uma interface com a linguagem de programação Objective-C no Xcode para o OsiriX, onde o utilizador tem a oportunidade de escolher obter os valores ou mapas paramétricos de cinco modelos de difusão diferentes. Também informa

---

acerca da qualidade de ajuste e fornece as curvas de ajuste aos dados. No botão de ajuda aparecem as referências aos modelos utilizados e informação extra.

Em conclusão, o *plug-in* permite a visualização do tumor e a distinção entre lesões malignas e benignas.

**Palavras-chave:** Imagem por Curtose de Difusão, Movimento Incoerente Intravoxel, Distribuição Gama, Truncado, “stretched-exponential”, Plug-in, OsiriX, Modelos Não Gaussianos

---

# CONTENTS

<b>List of Figures</b>	<b>xv</b>
<b>List of Tables</b>	<b>xxi</b>
<b>List of Symbols</b>	<b>xxiii</b>
<b>Acronyms</b>	<b>xxv</b>
<b>1 Introduction</b>	<b>1</b>
1.1 Context and motivation . . . . .	1
1.2 Objectives . . . . .	2
1.3 Dissertation plan . . . . .	2
1.4 Dissertation outputs . . . . .	3
<b>2 Theoretic Underpinnings</b>	<b>5</b>
2.1 Breast anatomy . . . . .	5
2.1.1 Benign vs Malignant lesions . . . . .	6
2.2 MRI . . . . .	6
2.2.1 Diffusion and MRI . . . . .	7
2.2.2 Diffusion . . . . .	9
2.2.3 Diffusion Weighted Imaging . . . . .	9
2.3 Non-Gaussian Models . . . . .	11
2.3.1 Diffusion Kurtosis Imaging . . . . .	11
2.3.2 Intravoxel Incoherent Motion . . . . .	13
2.4 Statistical distribution models . . . . .	15
2.4.1 Gamma Distribution . . . . .	15
2.4.2 Truncated Gaussian Distribution . . . . .	16
2.4.3 Stretched-Exponential Model . . . . .	16
2.5 State-of-the-art . . . . .	17
2.5.1 State-of-the-art of Diffusion Kurtosis Imaging . . . . .	17
2.5.2 State-of-the-art of Intravoxel Incoherent Motion . . . . .	18
2.5.3 State-of-the-art of Gamma Distribution . . . . .	21
2.5.4 State-of-the-art of Truncated Gaussian Distribution . . . . .	24

2.5.5	State-of-the-art of Stretched-Exponential . . . . .	25
<b>3</b>	<b>Materials and Methods</b>	<b>27</b>
3.1	Dataset and Acquisitions . . . . .	27
3.2	Image Processing Tools . . . . .	28
3.2.1	Producing parametric maps . . . . .	28
3.2.2	Obtaining parametric values with a ROI . . . . .	31
3.3	Testing the plug-in in images with different $b$ -values and noise . . . . .	32
3.3.1	Different $b$ values . . . . .	32
3.3.2	Different amount of noise . . . . .	34
<b>4</b>	<b>Results and Discussion</b>	<b>35</b>
4.1	Parametric maps . . . . .	35
4.1.1	Interface . . . . .	35
4.1.2	DKI parametric maps . . . . .	38
4.1.3	IVIM parametric maps . . . . .	42
4.1.4	Gamma parametric maps . . . . .	45
4.1.5	Truncated parametric maps . . . . .	52
4.1.6	Stretched parametric maps . . . . .	54
4.1.7	Goodness-of-fit maps . . . . .	57
4.2	Parametric values obtained through ROIs . . . . .	59
4.2.1	Interface to obtain the parametric values . . . . .	59
4.2.2	Obtained parametric values . . . . .	60
4.3	Number of $b$ values and noise tests . . . . .	73
4.3.1	$b$ values test . . . . .	73
4.3.2	Noise tests . . . . .	88
<b>5</b>	<b>Conclusions and Future Work</b>	<b>101</b>
	<b>Bibliography</b>	<b>103</b>
<b>A</b>	<b>Testing <math>b</math> values and noise</b>	<b>109</b>
A.0.3	Goodness of fit maps for the first combination of $b$ values removal	109
A.0.4	Goodness of fit maps of the maps with the noise added . . . . .	110
<b>B</b>	<b>Poster</b>	<b>121</b>

## LIST OF FIGURES

2.1	Anatomy of the breast. . . . .	6
2.2	Application of a radiofrequency pulse causing spins to align with the higher energy state. . . . .	8
2.3	Pulse sequence diagram of a spin eco sequence. . . . .	10
2.4	Examples of images obtained with Diffusion Weighted Imaging (DWI). . . . .	11
2.5	Probability distributions with the variation of kurtosis values. . . . .	12
2.6	Plot of signal attenuation of a well-perfused tissue with increasing $b$ values. . . . .	14
2.7	Gamma distribution of five curves. . . . .	15
2.8	Parametric maps of a patient with malignant carcinoma. . . . .	18
2.9	Parametric maps of a patient with fibroadenoma. . . . .	19
2.10	Box plot distribution of the parameters by lesion type of $ADC$ (a) parameter using the mono-exponential model, and $MD$ (b) and $MK$ (c) parameters using the kurtosis model. . . . .	20
2.11	Box plots in breast lesions and normal tissue of $D$ (a), $f$ (b), $D^*$ (c) and $ADC$ (d). . . . .	21
2.12	Parametric maps ( $D$ , $f$ , $D^*$ and $ADC$ ) of a 25-year-old woman with a fibroadenoma(thin arrow) and a simple cyst in her left breast. . . . .	22
2.13	Parametric maps ( $D$ , $f$ , $D^*$ and $ADC$ ) of a 30-year-old woman with invasive ductal carcinoma. . . . .	23
2.14	Evaluation of two fractional areas corresponding to $frac < 1$ and $frac > 3$ that are considered to reflect the small cell component and perfusion, respectively. . . . .	24
2.15	a) Scatter plot of $frac > 3$ vs $frac < 1$ ; b) Scatter plot of $\theta$ vs $\kappa$ ; for the cancer and not cancer group. . . . .	24
4.1	Interface of the plug-in. . . . .	36
4.2	Warning that appears when the user presses the "OK" button, next to the parametric maps check boxes, and doesn't select which model to run. . . . .	36
4.3	Warning that appears when the user tries to run the models on a parametric map and not a DWI image. . . . .	37
4.4	Window that alerts the user to wait while the program is running. . . . .	37
4.5	Window that informs the user on the amount that was multiplied to which image and also the references of the models that were used. . . . .	38

---

4.6	Window that alerts the user that the process to produce parametric maps is complete. . . . .	38
4.7	Images of a breast with malignant tumor (invasive ductal carcinoma): a) DWI image with the $b$ value $50 \text{ s/mm}^2$ ; b) DWI image with the Wiener filter applied. . . . .	39
4.8	$MD$ parametric maps with an arrow indicating a malignant lesion. . . . .	40
4.9	$MK$ parametric maps with an arrow indicating a malignant lesion. . . . .	40
4.10	$MD$ parametric maps with an arrow indicating a benign lesion. . . . .	41
4.11	$MK$ parametric maps with an arrow indicating a benign lesion. . . . .	41
4.12	$D^*$ parametric maps with an arrow indicating a malignant lesion. . . . .	42
4.13	$D$ parametric maps with an arrow indicating a malignant lesion . . . . .	43
4.14	$f$ parametric maps that show higher values of perfusion around the tumor area. . . . .	43
4.15	$D^*$ parametric maps with an arrow indicating a benign lesion. . . . .	44
4.16	$D$ parametric maps with an arrow indicating a benign lesion. . . . .	44
4.17	$f$ parametric maps that show high diffusion near the tumor area. . . . .	45
4.18	$\theta$ parametric maps with an arrow indicating a malignant lesion. . . . .	46
4.19	$\kappa$ parametric maps with an arrow indicating a malignant lesion. . . . .	46
4.20	$S1$ parametric maps with an arrow indicating a malignant lesion. . . . .	47
4.21	$S2$ parametric maps with an arrow indicating a malignant lesion. . . . .	47
4.22	$S3$ parametric maps with an arrow indicating a malignant lesion. . . . .	48
4.23	$\theta$ parametric maps with an arrow indicating a benign lesion. . . . .	49
4.24	$\kappa$ parametric maps with an arrow indicating a benign lesion. . . . .	49
4.25	$S1$ parametric maps with an arrow indicating a benign lesion. . . . .	50
4.26	$S2$ parametric maps with an arrow indicating a benign lesion. . . . .	50
4.27	$S3$ parametric maps with an arrow indicating a benign lesion. . . . .	51
4.28	$\sigma$ parametric maps with an arrow indicating a malignant lesion. . . . .	52
4.29	$ADC$ parametric maps with an arrow indicating a malignant lesion. . . . .	53
4.30	$\sigma$ parametric maps with an arrow indicating a benign lesion. . . . .	53
4.31	$ADC$ parametric maps with an arrow indicating a benign lesion. . . . .	54
4.32	$DDC$ parametric maps with an arrow indicating a malignant lesion. . . . .	55
4.33	$\alpha$ parametric maps with an arrow indicating a malignant lesion. . . . .	55
4.34	$DDC$ parametric maps with an arrow indicating a benign lesion. . . . .	56
4.35	$\alpha$ parametric maps with an arrow indicating a benign lesion. . . . .	56
4.36	Goodness-of-fit maps for Diffusion Kurtosis Imaging (DKI), Gamma, Truncated and Stretched models applied to a breast with a malignant lesion. . . . .	57
4.37	Goodness-of-fit map for DKI, Gamma, Truncated and Stretched models applied to a breast with a benign lesion. . . . .	58
4.38	Goodness-of-fit maps for the Intravoxel Incoherent Motion (IVIM) models applied to a breast with a malignant lesion. . . . .	58
4.39	DWI image of a breast with a malignant lesion (invasive ductal carcinoma) with $b$ value of $1000 \text{ s/mm}^2$ exemplifying a drawn ROI in order to then run the program. . . . .	59



4.40	Alert that warns the user that the program can only run if on the displayed window is the image where the user draws the ROI. . . . .	60
4.41	Warning that alerts the user that the process to obtain the parametric values is done running. . . . .	60
4.42	Warning that appears when the user is trying to save the results obtained but without running a model first. . . . .	61
4.43	Results for the parametric values obtained through ROIS around the malignant tumor (invasive ductal carcinoma) area. . . . .	61
4.44	Results for the parametric values obtained through ROIS around the benign tumor (fibroadenoma) area. . . . .	62
4.45	Fitting plot for the DKI model of a DWI image of the breast with a malignant lesion. . . . .	63
4.46	Fitting plot for the DKI model of a DWI image of the breast with a benign lesion. . . . .	64
4.47	Fitting plot for the IVIM model of a DWI image of the breast with a malignant lesion. . . . .	65
4.48	Fitting plot for the IVIM model of a DWI image of the breast with a benign lesion. . . . .	66
4.49	Fitting plot for the Gamma model of a DWI image of the breast with a malignant lesion. . . . .	67
4.50	Fitting plot for the Gamma model of a DWI image of the breast with a benign lesion. . . . .	68
4.51	Fitting plot for the Truncated model of a DWI image of the breast with a malignant lesion. . . . .	69
4.52	Fitting plot for the Truncated model of a DWI image of the breast with a benign lesion. . . . .	70
4.53	Fitting plot for the Stretched model of a DWI image of the breast with a malignant lesion. . . . .	71
4.54	Fitting plot for the Stretched model of a DWI image of the breast with a benign lesion. . . . .	72
4.55	$MD$ maps of a breast with a malignant lesion which show the quality decrease when are applied with images with less $b$ values. . . . .	73
4.56	$MK$ maps of a breast with a malignant lesion which show the quality decrease when are applied with images with less $b$ values. . . . .	74
4.57	$D^*$ maps of a breast with a malignant lesion which show the quality increase when are applied with images with less $b$ values. . . . .	75
4.58	$D$ maps of a breast with a malignant lesion which show the quality decrease when are applied with images with less $b$ values. . . . .	76
4.59	$f$ maps of a breast with a malignant lesion which show the quality increase when are applied with images with less $b$ values. . . . .	77

4.60 $\theta$ maps of a breast with a malignant lesion which show the quality decrease when are applied with images with less $b$ values. . . . .	78
4.61 $\kappa$ maps of a breast with a malignant lesion which show the quality decrease when are applied with images with less $b$ values. . . . .	79
4.62 $S1$ maps of a breast with a malignant lesion which show the quality decrease when are applied with images with less $b$ values. . . . .	80
4.63 $S2$ maps of a breast with a malignant lesion which show the quality decrease when are applied with images with less $b$ values. . . . .	81
4.64 $S3$ maps of a breast with a malignant lesion which show the quality decrease when are applied with images with less $b$ values. . . . .	82
4.65 $\sigma$ maps of a breast with a malignant lesion which show the quality decrease when are applied with images with less $b$ values. . . . .	83
4.66 $ADC$ maps of a breast with a malignant lesion which show the quality decrease when are applied with images with less $b$ values. . . . .	84
4.67 $DDC$ maps of a breast with a malignant lesion which show the quality decrease when are applied with images with less $b$ values. . . . .	85
4.68 $\alpha$ maps of a breast with a malignant lesion which show the quality decrease when are applied with images with less $b$ values. . . . .	86
4.69 Goodness-of-fit map for DKI, Gamma, Truncated and Stretched models applied to a breast with a malignant lesion when the image with the $b$ value $1000 \text{ s/mm}^2$ was removed. . . . .	87
4.70 $MD$ maps (scalling factor of $1 \times 10^6$ and in $\text{mm}^2/\text{s}$ ) of a breast with a malignant lesion (invasive ductal carcinoma) which show the quality decrease when are applied to images with 10%, 15%, 20%, 25%, 30% and 35% amount of noise, respectively.. . . .	89
4.71 $MK$ maps (scalling factor of $1 \times 10^3$ with no units since it is dimensionless) of a breast with a malignant lesion (invasive ductal carcinoma) which show the quality decrease when are applied to images with 10%, 15%, 20%, 25%, 30% and 35% amount of noise, respectively. . . . .	90
4.72 $D^*$ maps (scalling factor of $1 \times 10^6$ and in $\text{mm}^2/\text{s}$ ) of a breast with a malignant lesion (invasive ductal carcinoma) which show the quality increase when are applied to images with 10%, 15%, 20%, 25%, 30% and 35% amount of noise, respectively. . . . .	91
4.73 $D$ maps (scalling factor of $1 \times 10^6$ and in $\text{mm}^2/\text{s}$ ) of a breast with a malignant lesion (invasive ductal carcinoma) which show the quality decrease when are applied to images with 10%, 15%, 20%, 25%, 30% and 35% amount of noise, respectively. . . . .	92
4.74 $f$ maps (scalling factor of $1 \times 10^4$ and in %) of a breast with a malignant lesion (invasive ductal carcinoma) which show the quality increase when are applied to images with 10%, 15%, 20%, 25%, 30% and 35% amount of noise, respectively. . . . .	93

4.75 $\theta$ maps (scaling factor of $1 \times 10^4$ and in $\text{mm}^2/\text{s}$ ) of a breast with a malignant lesion (invasive ductal carcinoma) which show the quality increase when applied to images with 10%, 15%, 20%, 25%, 30% and 35% amount of noise, respectively. . . . .	94
4.76 $\kappa$ maps (scaling factor of 10 and with no units since it is dimensionless) of a breast with a malignant lesion (invasive ductal carcinoma) which show the quality increase when applied to images with 10%, 15%, 20%, 25%, 30% and 35% amount of noise, respectively. . . . .	95
4.77 S1 maps (scaling factor of $1 \times 10^3$ and in %) of a breast with a malignant lesion (invasive ductal carcinoma) which show the quality decrease when are applied to images with 10%, 15%, 20%, 25%, 30% and 35% amount of noise, respectively. . . . .	95
4.78 S2 maps (scaling factor of $1 \times 10^3$ and in %) of a breast with a malignant lesion (invasive ductal carcinoma) which show the quality increase when are applied to images with 10%, 15%, 20%, 25%, 30% and 35% amount of noise, respectively. . . . .	96
4.79 S3 maps (scaling factor of $1 \times 10^3$ and in %) of a breast with a malignant lesion (invasive ductal carcinoma) which show the quality increase when are applied to images with 10%, 15%, 20%, 25%, 30% and 35% amount of noise, respectively. . . . .	96
4.80 $\sigma$ maps (scaling factor of $1 \times 10^5$ and in $\text{mm}^2/\text{s}$ ) of a breast with a malignant lesion (invasive ductal carcinoma) which show the quality increase when applied to images with 10%, 15%, 20%, 25%, 30% and 35% amount of noise, respectively. . . . .	97
4.81 ADC maps (scaling factor of $1 \times 10^4$ and in $\text{mm}^2/\text{s}$ ) of a breast with a malignant lesion (invasive ductal carcinoma) which show the quality increase when are applied to images with 10%, 15%, 20%, 25%, 30% and 35% amount of noise, respectively. . . . .	98
4.82 DDC maps (scaling factor of $1 \times 10^7$ and in $\text{mm}^2/\text{s}$ ) of a breast with a malignant lesion (invasive ductal carcinoma) which show the quality increase when are applied to images with 10%, 15%, 20%, 25%, 30% and 35% amount of noise, respectively. . . . .	99
4.83 $\alpha$ maps (scaling factor of $1 \times 10^4$ and with no units since it is dimensionless) of a breast with a malignant lesion (invasive ductal carcinoma) which show the quality increase when applied to images with 10%, 15%, 20%, 25%, 30% and 35% amount of noise, respectively. . . . .	100
A.1 Goodness-of-fit map (Goodness-of-fit maps (scaling factor of $1 \times 10^3$ ) for DKI, Gamma, Truncated and Stretched models applied to a breast with a malignant lesion (invasive ductal carcinoma) when the image with the $b$ value $600 \text{ s}/\text{mm}^2$ was removed. . . . .	109

A.2	Goodness-of-fit map (Goodness-of-fit maps (scaling factor of $1 \times 10^3$ ) for DKI, Gamma, Truncated and Stretched models applied to a breast with a malignant lesion (invasive ductal carcinoma) when the image with the $b$ value $2000 \text{ s/mm}^2$ was removed. . . . .	110
A.3	Goodness-of-fit map (Goodness-of-fit maps (scaling factor of $1 \times 10^3$ ) for DKI, Gamma, Truncated and Stretched models applied to a breast with a malignant lesion (invasive ductal carcinoma) when the image with the $b$ value $200 \text{ s/mm}^2$ was removed. . . . .	111
A.4	Goodness-of-fit map (Goodness-of-fit maps (scaling factor of $1 \times 10^3$ ) for DKI, Gamma, Truncated and Stretched models applied to a breast with a malignant lesion (invasive ductal carcinoma) when the image with the $b$ value $800 \text{ s/mm}^2$ was removed. . . . .	112
A.5	Goodness-of-fit map (Goodness-of-fit maps (scaling factor of $1 \times 10^3$ ) for DKI, Gamma, Truncated and Stretched models applied to a breast with a malignant lesion (invasive ductal carcinoma) when noise (10%) is added to the image. . . . .	113
A.6	Goodness-of-fit map (Goodness-of-fit maps (scaling factor of $1 \times 10^3$ ) for DKI, Gamma, Truncated and Stretched models applied to a breast with a malignant lesion (invasive ductal carcinoma) when noise (15%) is added to the image. . . . .	114
A.7	Goodness-of-fit map (Goodness-of-fit maps (scaling factor of $1 \times 10^3$ ) for DKI, Gamma, Truncated and Stretched models applied to a breast with a malignant lesion (invasive ductal carcinoma) when noise (20%) is added to the image. . . . .	115
A.8	Goodness-of-fit map (Goodness-of-fit maps (scaling factor of $1 \times 10^3$ ) for DKI, Gamma, Truncated and Stretched models applied to a breast with a malignant lesion (invasive ductal carcinoma) when noise (25%) is added to the image. . . . .	116
A.9	Goodness-of-fit map (Goodness-of-fit maps (scaling factor of $1 \times 10^3$ ) for DKI, Gamma, Truncated and Stretched models applied to a breast with a malignant lesion (invasive ductal carcinoma) when noise (30%) is added to the image. . . . .	117
A.10	Goodness-of-fit map (Goodness-of-fit maps (scaling factor of $1 \times 10^3$ ) for DKI, Gamma, Truncated and Stretched models applied to a breast with a malignant lesion (invasive ductal carcinoma) when noise (35%) is added to the image. . . . .	118
A.11	Goodness-of-fit map (Goodness-of-fit maps (scaling factor of $1 \times 10^3$ ) for IVIM applied to a breast with a malignant lesion (invasive ductal carcinoma) when several amounts of noise (10%, 15%, 20%, 25%, 30% and 35%) is added to the image. . . . .	119

## LIST OF TABLES

2.1	ADC (apparent diffusion coefficient), $MD$ (mean diffusivity) and $MK$ (mean kurtosis) parameters obtained by the two models of DWI (mono-exponential and diffusion kurtosis), and differences by lesion type [13] . . . . .	18
2.2	Values of pure diffusion coefficient ( $D$ ), microvascular volume fraction ( $f$ ), perfusion-related incoherent microcirculation ( $D^*$ ) and apparent diffusion coefficient $ADC$ of malignant and benign breast lesions [14]. . . . .	19
2.3	Sensitivity and specificity of IVIM parameters [14]. . . . .	19
2.4	Values of apparent diffusion coefficient when the b values approaches zero $ADC_0$ , kurtosis $K$ , a dimensionless parameter, apparent diffusion coefficient of a mono-exponential model $ADC_{mono}$ , the volume fraction of incoherently flowing blood $fIVIM$ , perfusion-related incoherent microcirculation $D^*$ and the volume fraction of incoherently flowing blood using a mono-exponential model $fIVIM_{mono}$ [37]. . . . .	22
2.5	Values of the Gamma distribution parameters: the statistical dispersion of the distribution $theta$ and the probability distribution shape $\kappa$ [15] . . . . .	23
3.1	Sequence details for acquisition of the DWI images that were tested. . . . .	28
3.2	Scaling factors for each map on matlab in order for the maps to be correctly read by OsiriX. The units are also presented. . . . .	30



## LIST OF SYMBOLS

$\theta$  Statistical dispersion of the distribution.

$\kappa$  Probability distribution shape.

$\sigma$  Width of the distribution.

$\alpha$  Stretching parameter.

$D$  Pure diffusion coefficient.

$DDC$  Distributed diffusion coefficient.

$D^*$  Perfusion-related incoherent microcirculation.

$MD$  Mean diffusivity type.

$MK$  Mean kurtosis.

$S1$  Diffusion coefficients  $< 1 \times 10^{-3} \text{mm}^2/\text{s}$  typical in tumor cells with restricted diffusion.

$S2$  Diffusion coefficients  $> 1 \times 10^{-3} \text{mm}^2/\text{s}$  and  $< 3 \times 10^{-3} \text{mm}^2/\text{s}$  water diffusion in other components not mentioned in  $S1$  and  $S3$ .

$S3$  Diffusion coefficients  $< 3 \times 10^{-3} \text{mm}^2/\text{s}$  which represents the perfusion.

$f$  Microvascular volume fraction.





## ACRONYMS

**CLUT** Color Look Up Table.

**DKI** Diffusion Kurtosis Imaging.

**DNA** Deoxyribonucleic Acid.

**DWI** Diffusion Weighted Imaging.

**EPI** Echo planar imaging.

**IVIM** Intravoxel Incoherent Motion.

**MRI** Magnetic Resonance Imaging.

**PDF** Probability Distribution Function.

**ROI** Region Of Interest.

**TDLU** Terminal Ductal Lobular Unit.



## INTRODUCTION

### 1.1 Context and motivation

Breast cancer is the second most common type of cancer that affects women and is the second cause of death by cancer [1]. In Portugal only, there are 1500 women dying from this disease [2]. Patients with history of benign breast tumors, early menarche, late menopause, use of oral contraceptives, hormone replacement therapy, high breast density and obesity have a higher risk of contracting the disease [3, 4].

With improved therapeutic and imaging techniques, in the last decades the breast cancer mortality rate has decreased substantially [5].

The Magnetic Resonance Imaging (Magnetic Resonance Imaging (MRI)) of the breast is an important medical imaging technique since it is the most sensitive method to detect invasive breast cancer in comparison with mammography and ultrasound [6]. It is based on the magnetic properties of the hydrogen nucleus in biological tissues and it provides multiplanar images of the breast [7]. It is used to detect breast cancer in high-risk patients for example, patients with mutations on the BRCA1 and BRCA2 genes. These genes are both tumor suppressing genes and their proteins are evolved in fundamental cellular processes, including the repair of double strands ruptures of Deoxyribonucleic Acid (DNA) [6]. In spite of only being responsible for 2% of all breast cancers, in case of the person having those gene mutations, the chances of someday contracting the disease are between 45% and 65% [6][8].

"American Cancer society" has guidelines of how a mamography should be performed and also about the usage of MRI [9]. For example, MRI should be performed when the person in question has a first degree relative with mutations in BRCA 1 and 2 and also has more than 20% risk of contracting breast cancer based on their family history. Another possible situation to use MRI is when the imaging diagnostic is performed through

conventional methods. It is proven that, in this case, are detected malignant tumors that were hidden in mammography in approximately 3% to 9% of those women [10]. It is important to highlight that MRI can't be performed on its own, but in conjunction with mammography since 12% of breast cancers, like carcinomas, can't be detected by this imaging technique[11].

Diffusion Weighted Imaging (DWI) is a MRI technique based on the movement of water molecules in tissues. The main goals of this technique are the study of lesion characterization and better detection of small size lesions [12]. There are several extensions of DWI, like for example diffusion kurtosis imaging (DKI). This extension assumes that the water molecules movement doesn't follow a Gaussian Probability Distribution Function (PDF). Biological tissues have natural barriers that are going to restrict the water molecules movement, thus diverting the PDF form from Gaussian. Kurtosis has the ability to identify how much the PDF diverts from the Gaussian shape, which gives information about the complexity of the tissues helping in lesion characterization [13]. Apart from the DKI, other non-Gaussian models have been studied for breast, like the Intravoxel Incoherent Motion (IVIM), and the Gamma distribution model [14, 15]. Other models like the Truncated Gaussian distribution and Stretched-Exponential model have also been studied for DWI, however only for prostate and brain tissues [16, 17, 18]. All of these models have been proven to differentiate between malignant and benign lesions or normal tissue and lesions.

## 1.2 Objectives

This dissertation aims to develop a plug-in for OsiriX, which is a medical imaging clinical software. The purpose of the plug-in is to identify in a magnetic diffusion weighted image whether a tumor is benign or malignant through the non-Gaussian models of diffusion already existing and apply them to real images of the breast. The development of the plug-in was accomplished at Instituto de Biofísica e Engenharia Biomédica (IBEB).

## 1.3 Dissertation plan

The present dissertation has been structured so as to first cover relevant theoretic underpinnings of diffusion MRI and non-Gaussian models. It also includes the state-of-the-art. Secondly, there will be mentioned the materials and methods used to perform this study, like dataset usage and image processing steps. Thirdly, the results and their discussion will be presented to the reader according to each non-Gaussian model and outcomes of the plug-in. In the end, there will be a conclusion and future work chapter that summarizes the dissertation outcomes and informs the reader on what can be improved in the plug-in in the future.

## **1.4 Dissertation outputs**

Throughout the development of this dissertation, an abstract of the work that was being developed was submitted and accepted in 8th Workshop on Biomedical Engineering (WBME) and in NOVA Biomedical Workshop. In both of these workshops it was displayed a poster shown in appendix A.



## THEORETIC UNDERPINNINGS

In this chapter, the theoretic concepts are being introduced that are needed to better understand the state-of-the-art and remaining chapters of this dissertation. Firstly there is a small section about the breasts anatomy and the differences between malignant and benign lesions. Then there is a brief introduction to MRI and DWI. The models that differ from DWI are presented next and are divided in two sections, the Non-Gaussian models and the Statistical distribution models. The Non-Gaussian models explain the DKI and IVIM models and the Statistical distribution models explain the Gamma, Truncated and Stretched models. Afterwards, there is the State-of-the-art with the investigation done with each model applied to breast, with the exception of Truncated and Stretched which have not been applied to breast yet.

### 2.1 Breast anatomy

Macroscopically, the breast can be divided in two main parts. The first one is the glandular tissue, which is responsible for the production of milk. The second part are all of the other tissues that form and support the breast, which include adipose tissue (fat), fascia (connective tissue) and muscles, as shown in Figure 2.1 [19].

From the microscopic point of view, the breast is focused on the Terminal Ductal Lobular Unit (TDLU), which is the functional unit of the breast. It is composed of two ducts, an intralobular terminal duct and an extralobular duct, and of acini (functional epithelial cells that produce milk). Benign breast diseases and breast carcinomas have more than 90% of probability of originating in those units. They have three layers, the basement membrane, the myoepithelial layer and the epithelial lining. The epithelial layer has, normally, the thickness of only one cell. Hyperplasia happens when this thickness increases to two or three cells. If the thickness keeps increasing, the proliferation becomes

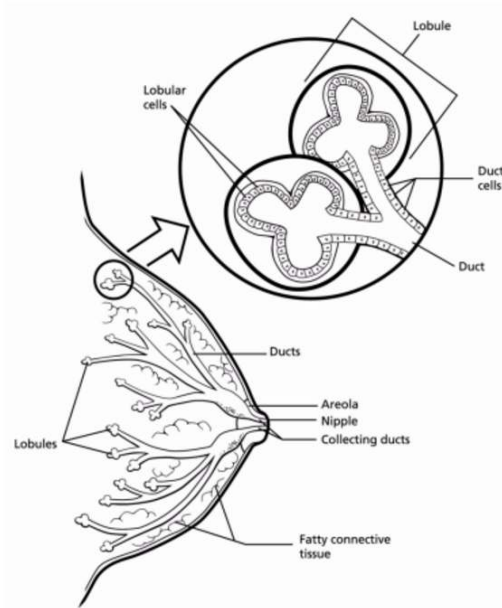


Figure 2.1: Anatomy of the breast. The female breast is constituted mainly of lobules (milk-producing glands), ducts (tubes that carry the milk from the lobules to the nipple), and stroma (fatty tissue and connective tissue surrounding the ducts and lobules, blood vessels, and lymphatic vessels). Adapted from [20]

categorized according to how many layers of cells are present and how atypical the cells appear. That way, it can range from atypical ductal hyperplasia to ductal carcinoma in situ. One barrier that prevents the spread of cancer is the epithelial layer. When this layer is breached, a carcinoma is labeled as invasive [19].

### 2.1.1 Benign vs Malignant lesions

Benign breast tumors tend to have a soft consistency and are mobile. Since they are slow-growing masses with a clear delimited margin or may be encapsulated their removal is easy and they rarely recur after removal. On the other hand, malignant tumors have irregular margins and are fast growing. They have an abnormal cell growth and can invade or spread to other parts of the body which defines them as cancer [21].

Although most benign tumors are not life-threatening, they have the potential to become malignant through tumor progression which is when there is an increase of the growth speed and invasiveness of the tumor cells [21].

## 2.2 MRI

### 2.2.1 Diffusion and MRI

MRI is a non invasive diagnostic technique that takes advantage of the natural magnetic properties of the human body. It uses hydrogen nuclei, which are present in water and



fat, to produce detailed anatomic images. A hydrogen nucleus is formed by only one proton which the axis, in the presence of a strong magnetic field, are forced to align either with or against the direction of the applied field. These two directions of alignment are a result of the existence of two possible energy levels that the protons can occupy inside a magnetic field. Since one of the levels has less energy than the other, the level with the lowest energy is going to have a number of protons higher than the level with the highest energy; this difference causes the net magnetization to be different from zero [22]. The frequency at which protons precess when a magnetic field is applied is determined by

$$\omega_0 = \gamma B_0 \quad (2.1)$$

where  $\omega_0$  is the Larmor frequency,  $\gamma$  is the gyromagnetic ratio of the atom and  $B_0$  is the magnitude of the applied magnetic field [23]. When radiofrequency energy at the Larmor frequency is applied, in a direction perpendicular to  $B_0$ , the magnetic vector is deflected causing the hydrogen nuclei to resonate. Subsequently, the magnetic vector is going to release the energy that was absorbed and returns to its resting state at a rate defined by the T1 and T2 relaxation times. As shown in Figure 2.2, a radiofrequency pulse of  $90^\circ$  is going to make the longitudinal magnetization in the tissue (vertical vector) become transverse (horizontal vector). Several radiofrequency pulses can be applied in order to emphasize the signal in the images, which happens as result of different tissues relaxing at different relaxation rates. Therefore, T1 will represent the amount of time that it takes for the magnetization to recover and align in the direction of the magnetic field, depending on the tissue in question, and T2 will be the duration of the transverse magnetization as protons wobble around the field. Due to heterogeneities of the local field, the protons wobble at different rates and the magnetic moment vectors of individual proton magnetic resonance signals begin to cancel each other out. The intensity of the signal will diminish as the transverse magnetization disappears [22].

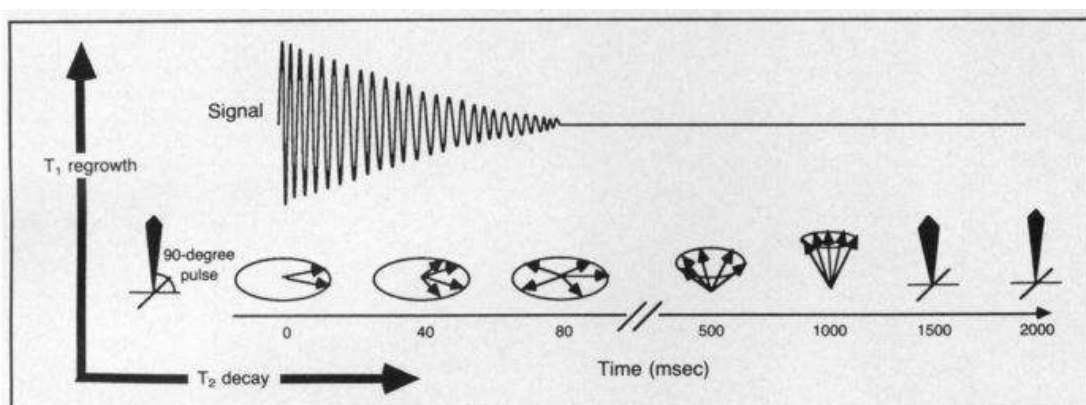


Figure 2.2: Application of a  $90^\circ$  radiofrequency pulse that will cause magnetization to flip and the spins to align with the higher energy state. The resting longitudinal magnetization will become transversal [22].

### 2.2.1.1 MRI and the Breast

MRI was proposed as a method to detect breast cancer in 1970. This discovery showed that T1 and T2 relaxation times of abnormal breast tissue were considerably different from normal tissue [5]. The contrast between tissues like fat, glandular tissue, lesions, etc, depends on the mobility and magnetic environment of the hydrogen atoms in the water and fat. These aspects define the intensity of the tissue signal in the image, which makes the parenchima, fat and lesion, in case of being present, even more evident [9]. Later, it was demonstrated that most breast cancers show a higher signal on T1- weighted images after the administration of gadolinium-based contrast [5]. This technique is highly sensitive (sensitivity between 71% and 100%). However, it is not enough to predict with precision which are the malign tumors, which means that it is necessary to resort to an invasive method called biopsy. Therefore, it became necessary to develop new non-invasive methods capable of predicting the histologic nature of the lesions [24].

### 2.2.1.2 Ultrasound and Mammography

The ultrasound imaging is the standard reference for differentiating between cysts and solid masses. However, this examination may lead to false results, specially in the absence of discrete mass. Since is difficult to distinguish between malignant and benign lesions due to ultrasound overlapping, biopsies are necessary, which in 70 % to 90 % of the cases have been proven to be unnecessary due to being benign tumors [7].

Mamography is the primary diagnostic tool for detection of breast cancer. However, its biggest disadvantage is that the produced image is two-dimensional, being the third dimension the thickness of the breast. This is projected onto a single plane, which can cause cancers to be obscured by overlying tissue, particularly in high-density breasts. The mammography in conjunction with the ultrasound imaging can increase the success rate in cancer detection by 50% [7].

It has been shown that MRI has higher sensitivity than 2D mammography which made it into a screening tool that can contribute in the early detection of cancer, specially in high-risk patients. However, it can't be performed by its own, but in conjunction with mammography since 12% of breast cancers, like carcinomas, can't be detected by this imaging technique[11].

## 2.2.2 Diffusion

In order to better understand how diffusion MRI works, it is useful to understand the physical principles of water diffusion. This phenomenon was seen for the first time by Robert Brown. He found that a big amount of molecules, in an environment without obstacles, have a random motion with a change of direction after a collision. This phenomenon is called Brownian movement, and was later theoretically proven by Einstein.

He showed that this random motion of the water molecules could be described by a Probability Distribution Function (PDF) which, in the absence of flow or barriers, is a Gaussian distribution centered around zero [25]. This means that the probability for a molecule to travel a short distance, or even not to move, is higher than the probability to travel a longer distance [26]. Therefore, the higher the mobility of the water molecules, the wider the Gaussian distribution will be [25].

### 2.2.3 Diffusion Weighted Imaging

DWI is a MRI technique that is non invasive and that allows the characterization and quantification of the molecular water diffusion in tissues [27]. It is typically performed using a T2 weighted spin-echo prepared Echo planar imaging (EPI) sequence, that is used due to its short acquisition times, which minimizes movement artifacts [28]. The diffusion preparation module uses two gradients that allow to measure diffusion. The first gradient pulse changes the magnetization of every water molecule, while the second gradient pulse completely removes this alteration, which will only happen as long as the water molecule remains at its original location. However, if moving spins experience an incomplete rephasing between diffusion gradients, it will lead to a diffusion-dependent signal attenuation. This means that if the water molecule makes any movement when these pulses are applied, it will lead to incomplete restoration of the water magnetization causing a decrease of the MR image signal. The loss of diffusion signal is controlled by the  $b$  value. The greater the mobility implies less MRI signal [29].

The  $b$  value parameter is given by Equation 2.2:

$$b = \gamma^2 G^2 \delta^2 (\Delta - \delta/3) \quad (2.2)$$

where  $\gamma$  is the proton gyromagnetic ratio,  $G$  is the gradient strength,  $\delta$  is the duration of the gradient and  $\Delta$  is the time between the application of the two diffusion gradients, as indicated in Figure 2.3 [30].

The magnetic resonance signal is reduced in intensity proportionally to water mobility. This is described by the Equation 2.3. Where  $S(b)$  is the intensity of the signal for different  $b$  values and  $S(0)$  is the intensity of the signal for a zero  $b$  value, or in other words, when there isn't a diffusion gradient applied [28].

$$\ln[S(b)] = \ln[S(0)] - bADC \quad (2.3)$$

The  $b$  value is then used to estimate the for each voxel of the image [31]. In general, the Apparent Diffusion Coefficient ( $ADC$ ) is defined as the surface area that delimits the volume that the water molecules can occupy, having into account the displacement during a certain period of time ( $\Delta$ ). It depends strongly on the interaction of the water molecules with its adjacent structures, rather on intrinsic diffusion properties [30].

The standard diffusion sequence can generate two types of images (Figure 2.4). The first are T2 weighted images that are obtained without any diffusion gradients ( $S(0)$ )

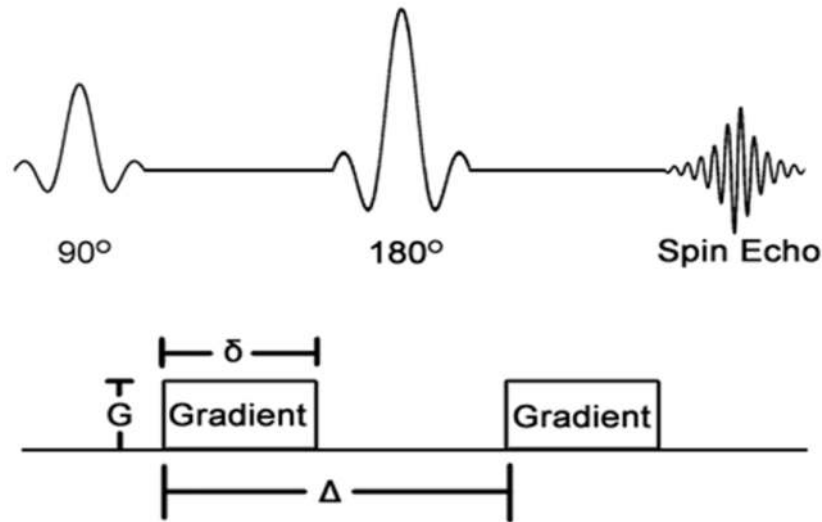


Figure 2.3: Pulse sequence diagram of a spin echo sequence. There are two diffusion-sensitizing gradients inserted before and after a  $180^\circ$  radiofrequency refocusing pulse. The important factors that define the degree of diffusion-sensitization are the gradient amplitude ( $G$ ), duration ( $\delta$ ), and the time between the two sensitizing gradients ( $\Delta$ )[28].

and the second are images that reflect the water mobility, which are diffusion weighted obtained with diffusion gradients ( $S(b)$ ). Diagnostic information can be disguised by long T2 signal, that is an artifact also known as "T2 shine through". The parametric ADC map is created in order to facilitate diffusion quantification, since it doesn't have the T2 shine through effects. In Figure 2.4 it is also possible to deduce that an area with restricted diffusion is more intense in a weighted image than in an ADC map [28]. Therefore, the ADC value decreases in the presence of malign tumors, since the bigger cellular density that exists in the tumoral tissue, in comparison with normal tissue, restricts the diffusion of the water molecules, which means that the ADC value can be used to detect and monitor the tumor [31].

Previous studies have shown a decrease on the number of false positive results with the DWI technique, having a sensitivity of 84% and a specificity of 79% [5]. However, this model is based on the assumption that the environment is homogeneous and since sometimes the benign and malign lesions can't be distinguished due to the overlap of their diffusion coefficients, there is a need to develop techniques that offer a better characterization of breast cancer tissues in a way to assist the classification and differential diagnosis of breast lesions [27].

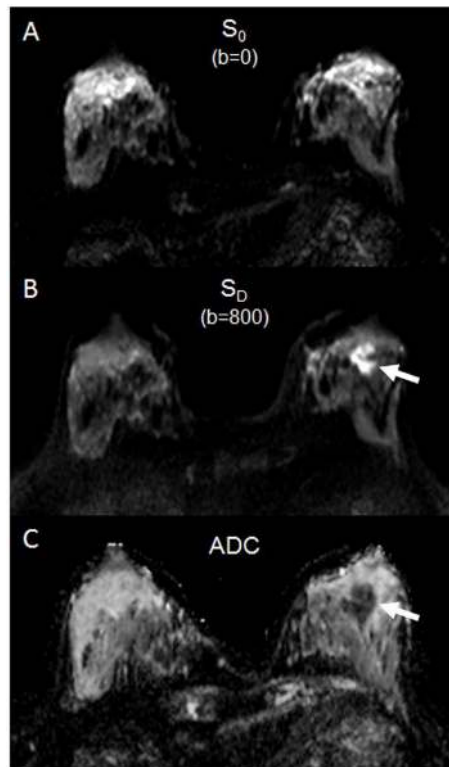


Figure 2.4: Examples of images obtained with DWI. A is  $S_0$  with  $b = 0s/mm^2$  and B is  $S_b$  with  $b = 800s/mm^2$ . Image C is an ADC map. The arrow points towards a tumor that in A and B appears hyperintense and in C appears hypointense, exhibiting low diffusion [28].

## 2.3 Non-Gaussian Models

### 2.3.1 Diffusion Kurtosis Imaging

The DWI model is able to characterize the average diffusion displacement of the water molecules in a three-dimensional space. However, it is not capable to provide specific information about the environment in which the water spins are located. That means that it is able to evince the shortness of the water diffusion distance, but it can't substantiate if the short distance is due to a more viscous environment or due to the presence of biological barriers like cellular membranes [32]. Thus, these techniques have some limitations, such as assuming that water diffusion follows a Gaussian distribution. It has already been proven that these models are not enough to characterize biological tissues because of barriers and compartments that restrict the water movement. This deviation from the Gaussian behavior can be quantified through the use of a non-dimensional metric called excess kurtosis, or kurtosis. Because the deviation from the Gaussian movement changes with the complexity of the tissue, kurtosis is a direct measure of the degree of tissue complexity [13, 33, 34, 35].

As is shown in Fig 2.5, if the kurtosis  $K$  has a positive value, the distribution is more concentrated around the mean value, making it more peaked than the Gaussian distribution. This means that in terms of diffusion it has a higher probability of occurring

small displacements than hindered diffusion. On the other hand, if  $K$  has a negative value, the tails of the distribution are wider and its peak lower, which means that the probability of small displacements would be lower than Gaussian diffusion, which is not expected in biological tissues since there isn't fully restricted diffusion. In spite of  $K$  being able to be positive or negative, in biological tissues  $K$  has been shown to have only positive values since one rather expects the imaged volume to consist of a mixture of hindered and restricted compartments [25].

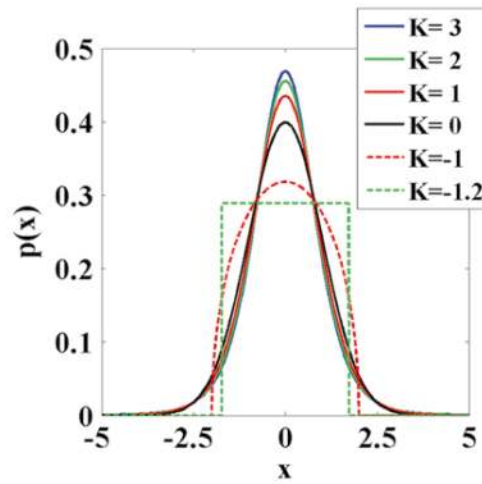


Figure 2.5: Probability distributions with the variation of kurtosis values [25].

The Diffusion Kurtosis Imaging (DKI) is an extension of the DWI model introduced by Jensen and Helpern in 2005 [13, 34, 36]. This model includes the kurtosis and diffusion coefficients and their estimation requires the use of high  $b$  values, that increase the duration of the exam in order to observe the non-Gaussian behavior of the water molecules diffusion [13, 36].

$$\ln[S(b)] = \ln[S(0)] - bMD + \frac{1}{6}b^2MD^2MK + O(b^3) \quad (2.4)$$

In order to obtain the kurtosis diffusion parameters, the equation (2.4) is used, where  $MD$  is the average diffusion,  $MK$  the average kurtosis and  $O(b^3)$  the error associated with the measurement. Both equations ((2.3) and (2.4)) are identical when  $MK$  is similar to zero and the  $ADC$  is similar to  $MD$  [13]. It should be noticed that unlike what occurs in equation 2.3, the kurtosis variable in equation 2.4 appears as part of a term depending on  $b^2$ , which means that the signal won't decay linearly with the  $b$  value [25]. When  $MK$  has a positive value, the PDF has a sharper peak, which means that lesions with a more complex micro-structure (malign) manifest higher  $MK$  values, unlike benign lesions [13, 27].

### 2.3.2 Intravoxel Incoherent Motion

An important aspect of diffusion MRI is its sensitivity to perfusion since the flow of blood water in randomly oriented capillaries is similar to diffusion – named intravoxel incoherent motion (IVIM) effect [37]. IVIM is a technique that uses low  $b$ -values (i.e., 0–1000  $\text{s}/\text{mm}^2$ ) DWI to separate the estimation of tissue perfusion and diffusivity, followed by biexponential curve fitting [14]. At low  $b$  values (e.g., 100  $\text{s}/\text{mm}^2$ ), the measured signal attenuation comes from not only the water diffusion in tissues, but also from microcirculation in capillaries [38].

This type of diffusion depends on the displacement speed of the flowing blood, the vascular architecture and the  $b$  values, which affect the signal attenuation in each imaging voxel. However, the amount of signal attenuation from pseudo-diffusion (microcirculatory perfusion of blood within capillaries with no specific orientation) is bigger than tissue diffusion due to the large distances of proton displacement while motion-probing gradients are being applied. This means that at low  $b$  values, pseudo-diffusion has a relatively high contribution to the DW-MRI signal and at high  $b$  values it accounts for only a small proportion [38].

Figure 2.6 shows a plot of signal attenuation of a well-perfused tissue (liver parenchyma) with increasing  $b$  values from a healthy person. It is possible to see in the figure that there is a steeper slope of signal attenuation when the  $b$  values are low. Since protons in flowing blood have larger diffusion distances and the signal is attenuated by small weightings (e.g.,  $<100 \text{ s}/\text{mm}^2$ ), the steep slope can be justified by microcapillary perfusion. When larger  $b$  values (e.g.,  $>100 \text{ s}/\text{mm}^2$ ) are being applied, the signal attenuation of the perfusing protons is almost complete, hence microcapillary perfusion will have a lower contribution to the signal. Therefore, in figure 2.6, at larger  $b$  values the slope of signal attenuation is less steep and is more reflective of tissue diffusivity [38].

Consequently, from the IVIM model is possible to obtain the following parameters: pure diffusion coefficient ( $D$ ), perfusion-related incoherent microcirculation ( $D^*$ ), which is considered proportional to the mean capillary segment length and average blood velocity, and microvascular volume fraction ( $f$ ) as it is shown in Equation (2.5) [14].

$$\frac{S(b)}{S(0)} = (1 - f)\exp(-bD) + f\exp[-b(D^* + D)] \quad (2.5)$$

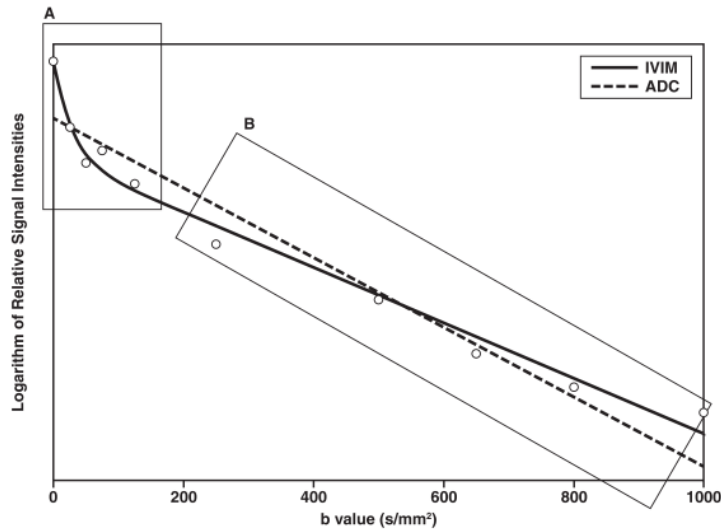


Figure 2.6: The plot shows the logarithm of relative signal intensity versus  $b$  value from normal liver parenchyma from an healthy 30-year-old man. Within the A box there is a decrease in plotted signal values at low  $b$  values in comparison with a more gradual attenuation of signal at higher  $b$  values (box B). By applying intravoxel incoherent motion (IVIM) analysis, it is possible to obtain the signal attenuation biexponential behavior (solid line), while by using a simple monoexponential apparent diffusion coefficient (ADC) line fitted to the data (dotted line), a suboptimal characterization of the signal is obtained[38].

### 2.3.2.1 Intravoxel Incoherent Motion and Diffusion Kurtosis Imaging

Iima et al. [37] explored the potential of non-Gaussian diffusion and perfusion MRI. Since IVIM is used with low  $b$  values and DKI with high  $b$  values, both models were taken into account, creating an updated quantitative imaging framework.

When both models are joined, the final equation (Equation 2.6) is:

$$S(b) = S(0)f_{IVIM}\exp(-bD^*) + (1 - f_{IVIM})\exp[-bADC_0 + (bADC_0)^2K/6] \quad (2.6)$$

where, as it was referred before in 2.3.2,  $S(0)$  is theoretical signal when  $b$  is equal to zero;  $f_{IVIM}$  the (T1-,T2- weighted) volume fraction of incoherently flowing blood in the tissue;  $D^*$  perfusion-related incoherent microcirculation associated to the IVIM effect;  $ADC_0$  which is the ADC value when the  $b$  value approaches zero.  $K$  is the dimensionless kurtosis coefficient which characterizes the deviation from the Gaussian behavior and, consequently making it a direct measure of the tissues heterogeneity [37]. It is possible to see the similarities between equation (2.4), equation (2.5) and equation (2.6) [37].



## 2.4 Statistical distribution models

### 2.4.1 Gamma Distribution

The Gamma distribution model is based on a statistical approach that can be related to heterogeneous tissues considering that tumor tissue is a mixture of different tissues and perfusion components. It works by assuming that each tissue component has a certain *ADC* that matches a part of the *ADC* distribution [15, 39].

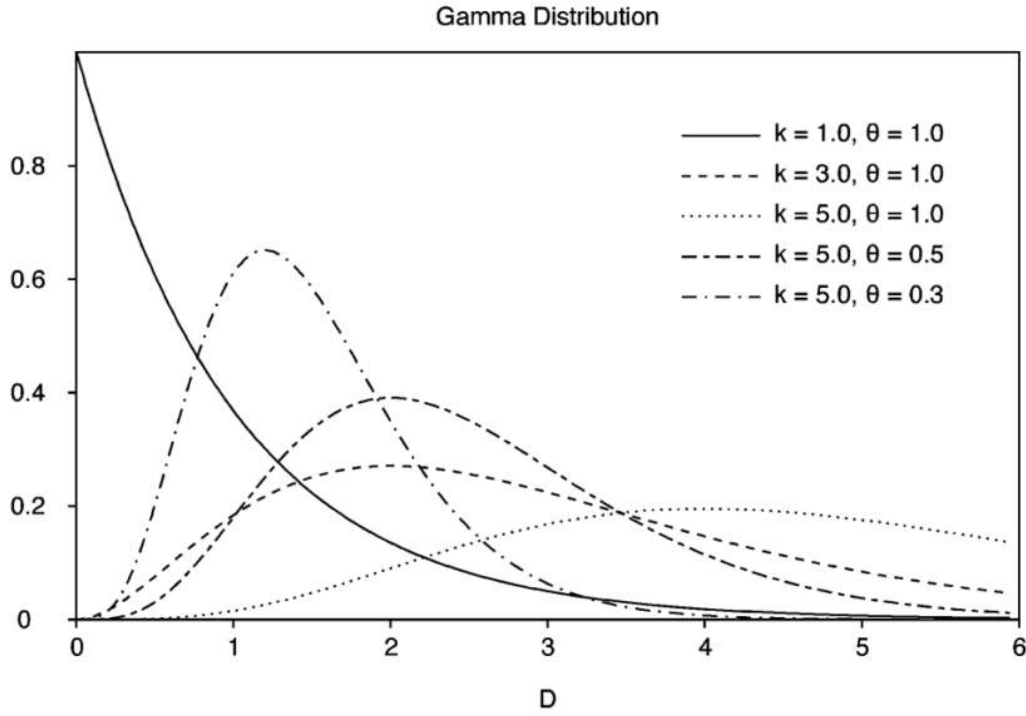


Figure 2.7: Gamma distribution of five curves, each with different parameters values. When the shape parameter  $\kappa$  and the scale parameter  $\theta$  changes, the distribution shape varies significantly [39].

This model has two main parameters that define the distribution: the  $\theta$  parameter, which shows the statistical dispersion of the distribution, and the  $\kappa$  parameter, that is responsible for the probability distribution shape [15, 39]. In Figure 2.7, the effect of the parameters on the distribution curves is clear. The distribution is given by Equation 2.7:

$$\rho(D) = \frac{1}{\Gamma(\kappa)\theta^\kappa} D^{\kappa-1} \exp\left(-\frac{D}{\theta}\right) \quad (2.7)$$

where  $\Gamma$  is the gamma function and  $D$ , the diffusion coefficient. When the diffusion coefficient is distributed according to this function, we obtain the following equation:

$$S(b) = S(0) \int_0^\infty \rho(D) \exp(-bD) dD = S(0) \frac{1}{(1 + \theta b)^\kappa} \quad (2.8)$$

where  $b$  is the  $b$  value. The  $\theta$  and  $\kappa$  can be estimated by curve-fitting of magnetic resonance diffusion data that is obtained by using multiple  $b$  values [39].

### 2.4.2 Truncated Gaussian Distribution

The truncated Gaussian distribution is a statistical model that reflects the consequences of a distribution of length scales for restrictions and hindrances to water diffusion, through a diffusion coefficient probability distribution which is defined by a mean value and a distribution width. This model assumes that a given voxel containing several cells, and intercellular and extracellular spaces, can be described as a sum of different spin packets. These packets have different  $ADC$  values since they originate from different positions, went through different trajectories and faced different restrictions and hindrances to displacement [40]. Under these assumptions, the signal can be described by Eq (2.9):

$$S = S_0 \exp\left(-bADC + \frac{1}{2}\sigma^2 b^2\right) \quad (2.9)$$

where  $\sigma$  is the width of the distribution. This model is able to fit the data with only two free parameters ( $ADC$  and  $\sigma$ ) that can quantify the diffusion heterogeneity by the width of the distribution of diffusion rates [18]. This model has not yet been applied to breast MRI.

### 2.4.3 Stretched-Exponential Model

The stretched-exponential model was first described by Bennet et al. [41] for brain imaging. It was presented as an alternative to the biexponential model of water diffusion that assumed the existence of two different proton pools inside of each voxel, which had different diffusion rates resulting in signal relaxation. The stretched-exponential model makes no assumption on the number of intravoxel proton pools, proposing that the signal attenuation came from a collection of uncoupled exponential decay processes, resulting in the following equation (2.10) :

$$\frac{S(b)}{S(0)} = \int_0^\infty \rho(D)e^{-bD} dD \quad (2.10)$$

which when described as a function of  $b$  results in equation (2.11):

$$\frac{S(b)}{S(0)} = \exp\{-(b \times DDC)^\alpha\} \quad (2.11)$$

where  $\alpha$  is the stretching parameter, which relates to intravoxel water diffusion heterogeneity, and  $DDC$  is the distributed diffusion coefficient, which represents the mean intravoxel diffusion rates [41, 42]. The  $\alpha$  parameter varies from zero to one. When it is close to one, it indicates that the apparent diffusion has high homogeneity, or mono-exponential diffusion-weighted signal decay. Inversely, if it is close to zero, it indicates non-exponential behavior due to high intravoxel diffusion heterogeneity. (It is important

to refer that when heterogeneity is mentioned in this model, it refers to intravoxel heterogeneity of exponential decay and not to intervoxel heterogeneity of diffusion coefficients). The *DDC* can be considered to be an individual *ADC* approximation weighted by the volume fraction of water in each part of the continuous distribution of *ADCs* [17, 41, 42].

This model has the ability to give an accurate description of the water diffusion in tissues since it is able to fit a variety of observed decay shapes using only two fit parameters [42].

## 2.5 State-of-the-art

Several studies have been made on the non gaussian models mentioned previously. In spite most of the models having been applied to breast, two of them have only been applied to the brain and the prostate (truncated and stretched models). In this section the reader will be able to see the results from the studies applied to these models. All of these models have proven to successfully detect malignant tumors being the reason for why they were adapted to produce parametric maps in this plugin.

### 2.5.1 State-of-the-art of Diffusion Kurtosis Imaging

Nogueira et al. [13] concluded in their study that there are significant differences between the *MD* and *MK* lesion types when the *DKI* model is applied. As is seen in Figure 2.10 and in Table 2.1, *MK* values are lower for benign lesions than for malignant lesions and *MD* values are higher for benign lesions than for malignant lesions [13]. This decrease of *MD* and increase of *MK* can be explained by the increase of cellularity observed in malignant tumors. If there are less barriers, like in the case of benign tumors, the diffusion of water molecules will be easier, thus *MD* values will be higher and the *MK* values will be lower, since it is approaching a Gaussian profile which is a characteristic of homogeneous environment. According to a study directed by Wu et al. [27] the sensitivity for *MD* and *MK* is respectively 79,3% and 84,2%. As for the specificity is 92,9% for both parameters. Wu also compared the results through parametric maps seen in Figure 2.8 of a patient with malignant carcinoma – infiltrating ductal carcinoma. In (a) and (b) shows a T2- weighted TSE image and a DW image when *b* is equal to zero where the lesion is easily seen. In (c) the lesion is seen darker, meaning that the *MD* values are lower and in (d) the lesion is seen lighter, which means that it has higher values of *MK*. These results are consistent with a malignant tumor. In Figure 2.9 shows also in a) and (b) a T2- weighted TSE image and a DWI image when *b* is equal to zero where the lesion is easily seen. In (c) the lesion is seen lighter, meaning that the *MD* values are higher, and in (d) the lesion is seen darker, which means that it has lower values of *MK*. Therefore, the same conclusion is reached as in Figure 2.8, that these results are consistent with a benign tumor.

However, the use of the kurtosis model requires long acquisition times, since it implies using high *b*-values with increased TE and complex post processing [13, 43] [33].

Table 2.1: *ADC* (apparent diffusion coefficient), *MD* (mean diffusivity) and *MK* (mean kurtosis) parameters obtained by the two models of DWI (mono-exponential and diffusion kurtosis), and differences by lesion type [13]

Mean	Benign (n=13)	Malignant (n=31)	$p^*$
$ADC^a$	$1.96 \pm 0.41$	$1.33 \pm 0.43$	0.017
$MD^a$	$2.17 \pm 0.42$	$1.52 \pm 0.50$	0.028
$MK^b$	$0.37 \pm 0.18$	$0.61 \pm 0.27$	0.017

<sup>a</sup> *ADC* and *MD* ( $\times 10^{-3} \text{mm}^2/\text{s}$ )

<sup>b</sup> *MK* is a dimensionless metric

\*Statistical differences

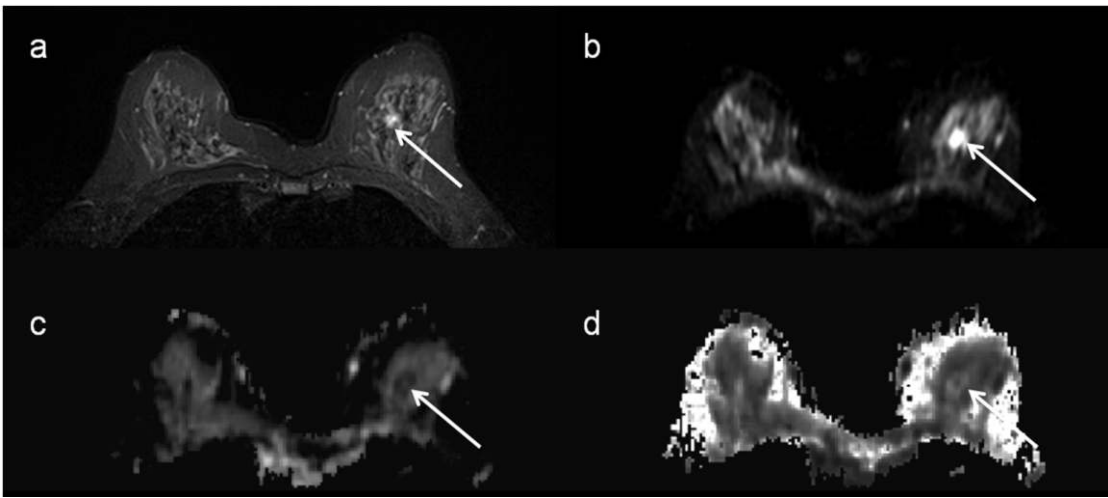


Figure 2.8: The white arrow indicates a malignant carcinoma (infiltrating ductal carcinoma) of a 51 year-in-old woman: a) T2-weighted Turbo spin echo (TSE) image; b) DW image at  $b=0$ ; c) *MD* - mean diffusion map; d) *MK* - mean kurtosis map [27].

### 2.5.2 State-of-the-art of Intravoxel Incoherent Motion

Liu et al. [14] found that  $D$  values of malignant tumors were significantly smaller than those of benign lesions, cysts and normal breast tissues, as seen on Table 2.2 and on Figure 2.11. Also, the  $ADC$  values and  $D$  values between malignant and benign tumors were different, concluding that the microperfusion effect did add information to the  $ADC$  value. The  $f$  values were higher in malignant tumors which supported the theory that malignant tumors have higher vascularity. This observation, in combination with the low  $D$  value, strongly suggests the presence of a malignant lesion. In the mean time,  $(D^*)$  did not show any significant differences between malignant and benign lesions, which may be caused by the varying vascularity among different tumor types. In Figure 2.11 there is also a comparison of the parameter values between malignant, benign, cyst and normal tissue. However, cyst, malignant, benign and normal tissue do not show significant differences. While in the malignant, benign and normal tissue, the parameters had significantly different values (except  $D^*$  as it was referred before). Liu also produced parametric maps (Figure

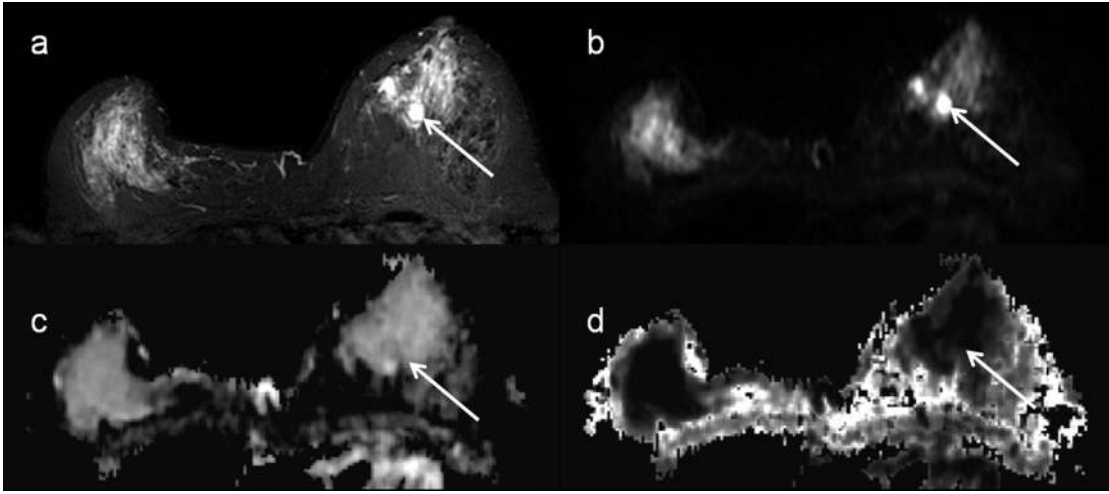


Figure 2.9: The white arrow indicates a benign lesion (fibroadenoma) of a 56 year-in-old woman: a) T2-weighted Turbo spin echo (TSE) image; b) DW image at  $b=0$ ; c)  $MD$  - mean diffusion map; d)  $MK$  - mean kurtosis map [27].

Table 2.2: Values of pure diffusion coefficient ( $D$ ), microvascular volume fraction ( $f$ ), perfusion-related incoherent microcirculation ( $D^*$ ) and apparent diffusion coefficient  $ADC$  of malignant and benign breast lesions [14].

	Malignant tumors (n = 40) Median (quartiles)	Benign lesions (n = 41) Median (quartiles)	$p$
$D$ ( $\times 10^{-3} \text{mm}^2/\text{s}$ )	0.85 (0.77, 0.98)	1.35 (1.26, 1.44)	0.000
$f$ (%)	10.34 (7.68, 11.88)	6.83 (4.72, 10.33)	0.000
$D^*$ ( $\times 10^{-3} \text{mm}^2/\text{s}$ )	94.71 (70.33, 113.23)	107.49 (83.20, 131.19)	0.000
$ADC$ ( $\times 10^{-3} \text{mm}^2/\text{s}$ )	0.95 (0.83, 1.06)	1.39 (1.32, 1.50)	0.000

Table 2.3: Sensitivity and specificity of IVIM parameters [14].

	Sensitivity (%)	Specificity (%)
$D$ ( $\times 10^{-3} \text{mm}^2/\text{s}$ )	90	92.68
$f$ (%)	87.50	53.66
$D^*$ ( $\times 10^{-3} \text{mm}^2/\text{s}$ )	85.00	41.46
$ADC$ ( $\times 10^{-3} \text{mm}^2/\text{s}$ )	92.50	90.24

2.12 and Figure 2.13) which were in agreement with the results already mentioned. In the figures, the  $D$ ,  $ADC$  and  $f$  maps, are darker for the malignant lesion, which means that it has low values, and brighter for the benign lesion, which means that it corresponds to higher values. The specificity and sensibility of the models are shown in Table 2.3.

According to a study for prostate cancer, the  $f$  values were significantly increased in tumors with  $b$  values below  $800 \text{ s}/\text{mm}^2$ . However, the  $f$  values became lower or indistinguishable from normal tissues with high  $b$  values [44]. Meaning that to obtain good parametric values, the images used can't have a bigger  $b$  value than  $800 \text{ s}/\text{mm}^2$ .

Liu et al. [14] in agreement with Sigmund et al. [45] concluded that avoiding vascular

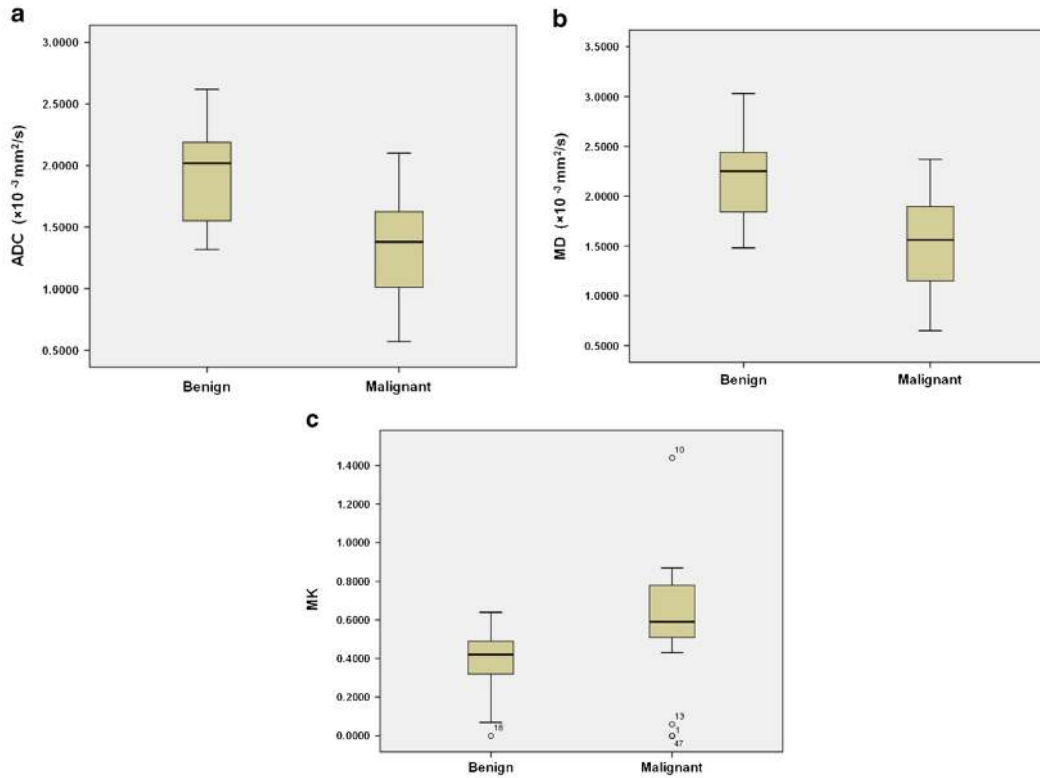


Figure 2.10: Box plot distribution of the parameters by lesion type of  $ADC$  (a) parameter using the mono-exponential model, and  $MD$  (b) and  $MK$  (c) parameters using the kurtosis model.  $MK$  is a dimensionless metric [13]

contributions made the differentiation between normal and malignant lesions more effective than with only  $ADC$  values. However, both works presented limitations. They had a small population of patients to examine which made the comparison between results more challenging. Another important limitation is the unknown suitable number of  $b$  values for breast IVIM (varying from six to ten in previous studies) making the selection of  $b$  values and reduction of their number crucial for an optimal procedure.

### 2.5.2.1 State-of-the-art of Intravoxel Incoherent Motion Diffusion Kurtosis Imaging

The results obtained by Iima et al. [37] are shown in Table 2.4. In order to show differences from non-Gaussian models and Gaussian models, the authors also compared the values obtained from the IVIM/DKI models with the ones from standard mono-exponential models ( $ADC_{mono}$  and  $fIVIM_{mono}$ ). In malignant lesions, the  $K$  (dimensionless parameter) was significantly higher and  $ADC_0$  lower than that in benign lesions. Although  $ADC_{mono}$  also showed differences between malignant and benign tumors or normal tissue, they were always smaller than  $ADC_{mono}$  values.  $fIVIM$  had higher values in malignant tumors than that in benign tumors and  $D^*$  and  $fIVIM_{mono}$  showed no significant difference between malignant and benign tumors. The specificity and sensitivity of the models are shown in Table 2.3.

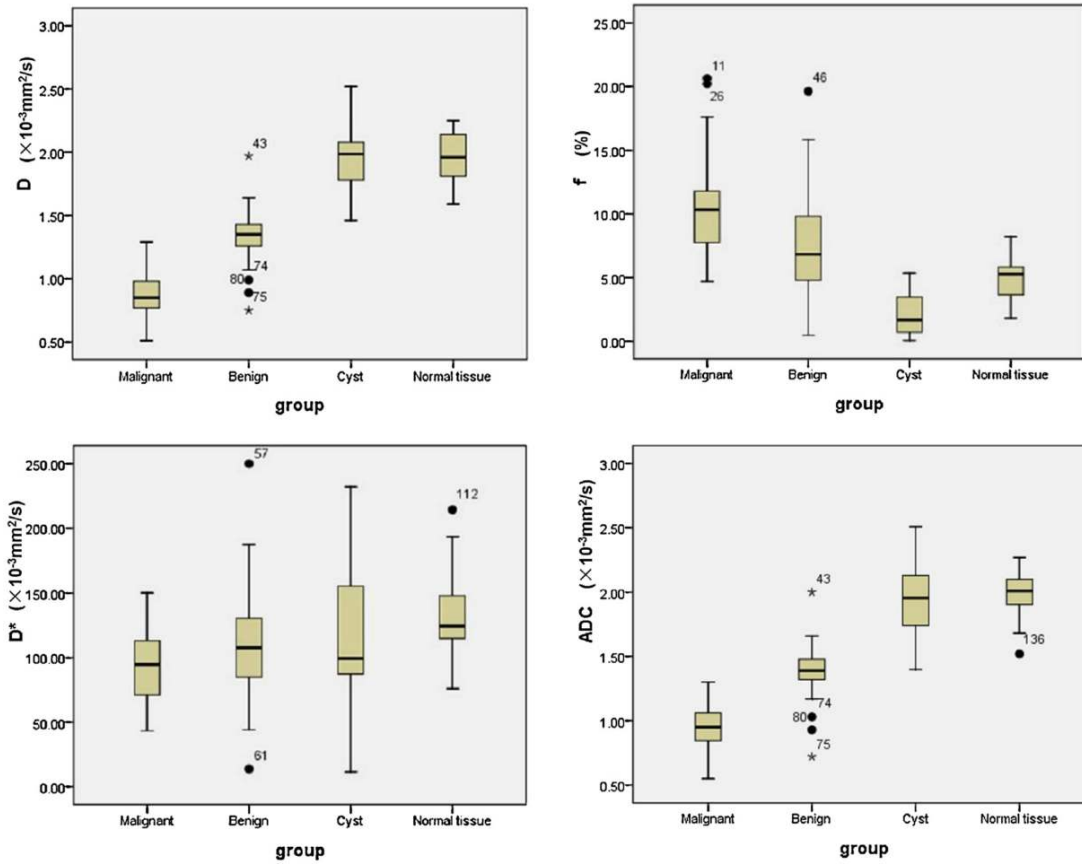


Figure 2.11: Box plots in breast lesions and normal tissue of  $D$  (a),  $f$  (b),  $D^*$  (c) and  $ADC$  (d). The line in a box represents median value [14].

In conclusion, both diffusion and perfusion parameters from this model were able to differentiate between malignant and benign tumors with high sensitivity and specificity. Which means that this study was able to estimate diffusion and perfusion parameters in one step [37]. However, the fitting approaches (such as the Marquardt-Levenberg algorithm) used to estimate the parameters, are very sensitive to noise. In order to resolve this issue, the equation is often divided in two steps. First estimating the diffusion parameters and then the perfusion parameters from the residual signal. Nonetheless, it assumes that the IVIM perfusion effects don't contribute to signal for  $b$  values above a certain cutoff value, which is not the case in spite of having a smaller contribution. Another drawback, is sensitivity of the algorithm towards the set of initial parameters that are required for the fitting process to begin. And like the other models, the population size in which the tests were made was very small [37].

### 2.5.3 State-of-the-art of Gamma Distribution

Borlinhas et al. [15] confirmed that both  $\theta$  and  $\kappa$  parameters can distinguish between malign and benign tumors. As shown in Table 2.5, in case of a malignant tumor,  $\theta$  will

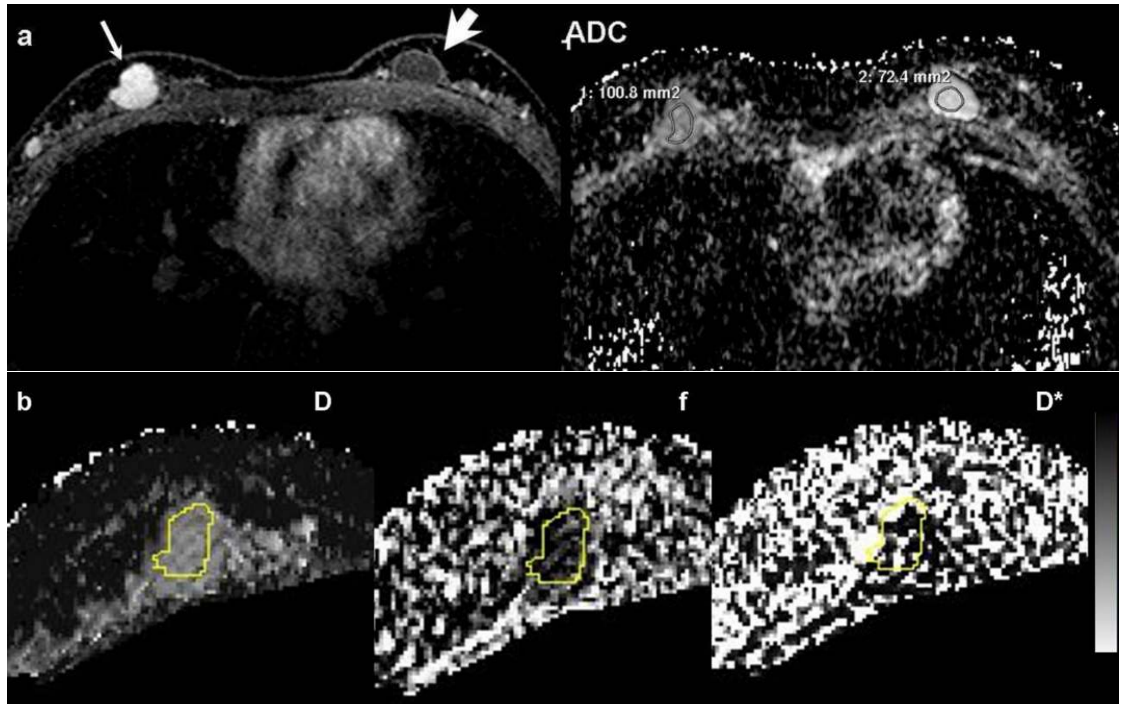


Figure 2.12: Parametric maps of a 25-year-old woman with a fibroadenoma (thin arrow) and a simple cyst in her left breast (thick arrow): pure diffusion coefficient ( $D$ ), microvascular volume fraction ( $f$ ), perfusion-related incoherent microcirculation ( $D^*$ ) and apparent diffusion coefficient  $ADC$  [14].

Table 2.4: Values of apparent diffusion coefficient when the  $b$  values approaches zero  $ADC_0$ , kurtosis  $K$ , a dimensionless parameter, apparent diffusion coefficient of a mono-exponential model  $ADC_{mono}$ , the volume fraction of incoherently flowing blood  $fIVIM$ , perfusion-related incoherent microcirculation  $D^*$  and the volume fraction of incoherently flowing blood using a mono-exponential model  $fIVIM_{mono}$  [37].

Parameter	Malignant	Benign	$p$
$ADC_0 (\times 10^{-3} \text{mm}^2/\text{s})$	1.05 (0.94–1.17)	1.73 (1.51–1.94)	<0.001
$K$	0.82 (0.70–0.94)	0.55 (0.42–0.68)	<0.05
$ADC_{mono} (\times 10^{-3} \text{mm}^2/\text{s})$	1.00 (0.88–1.11)	1.50 (1.35–1.66)	<0.001
$fIVIM\%$	12.3 (8.86–15.7)	5.00 (0.60–9.40)	<0.05
$D^* (\times 10^{-3} \text{mm}^2/\text{s})$	10.9 (5.95–15.9)	13.9 (5.96–21.9)	0.52
$fIVIM_{mono}\%$	8.63 (7.39–9.86)	8.66 (6.97–10.4)	1.00

have high values, the distribution will be more expanded; when  $\kappa$  is smaller, the shape of the distribution will be more altered. For benign tumors it would be the other way around,  $\theta$  will be lower, the distribution will be more compressed, and  $\kappa$  will be higher and the shape of the distribution will be less altered [39].

Oshio et al. [39] considered tumor tissue to include relatively small tumor cells, larger normal cells, extracellular fluid, and microcirculating blood within capillaries. He also argued that when  $ADC$  values are smaller than  $1.0 \text{mm}^2/\text{s}$  it can happen due to the



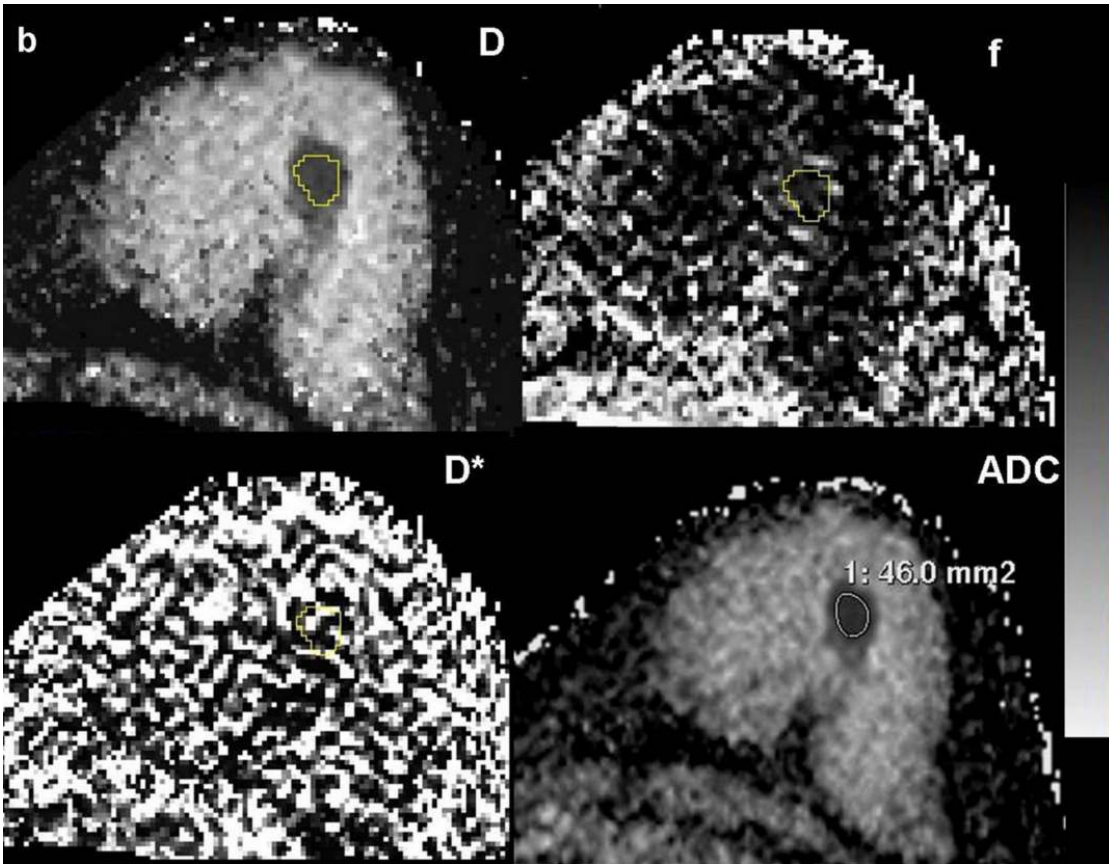


Figure 2.13: Parametric maps of a 30-year-old woman with invasive ductal carcinoma: b: IVIM parametric maps of pure diffusion coefficient ( $D$ ), microvascular volume fraction ( $f$ ), perfusion-related incoherent microcirculation ( $D^*$ ) and apparent diffusion coefficient ( $ADC$ ) maps [14].

Table 2.5: Values of the Gamma distribution parameters: the statistical dispersion of the distribution  $\theta$  and the probability distribution shape  $\kappa$  [15]

Parameters	Malignant	Benign
$\theta(\times 10^{-3} \text{mm}^2/\text{s})$	$1.23 \pm 0.52$	$4.29 \pm 1.90$
$\kappa$	$0.97 \pm 0.50$	$0.65 \pm 0.43$

presence of tumor cells with restricted diffusion. Also, if the  $ADC$  values are larger than  $3.0 \text{mm}^2/\text{s}$  it can happen due to perfusion and if they are between those two values, it is attributed to water diffusion in the other components. This way, for clinical evaluation, two fractional areas were evaluated. With  $\text{frac} < 1$  ( $D < 1.0 \text{mm}^2/\text{s}$ ) and  $\text{frac} > 3$  ( $D > 3.0 \text{mm}^2/\text{s}$ ) like is shown in Figure 2.14.

The results that were obtained and shown in Figure 2.15 were from prostate DWI images. In Image a), the cancer group (ca) and non cancer group (PZ) are distinct and separated. Unlike Image b) which the separation is not clearly visible [39].

This model has several advantages like: having a simple mathematical equation that is easy to handle; and the stability of the fitting process [39].

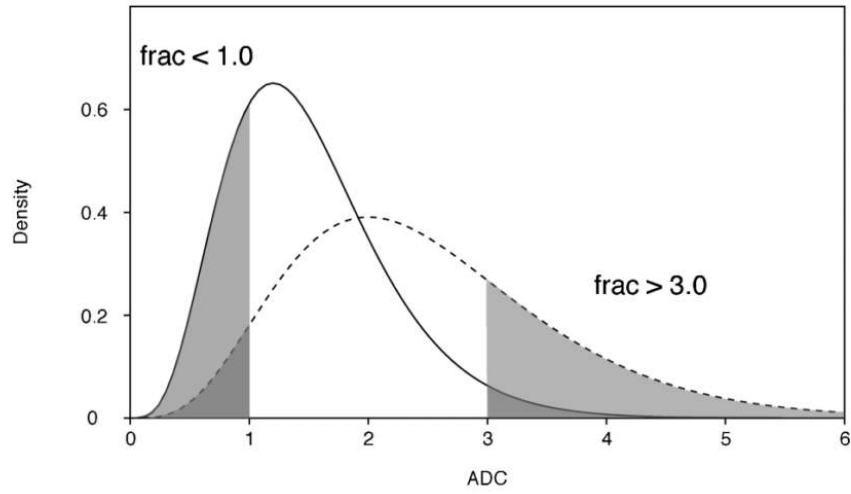


Figure 2.14: Evaluation of two fractional areas corresponding to  $\text{frac} < 1$  ( $D < 1.0 \text{ mm}^2/\text{s}$ ) and  $\text{frac} > 3$  ( $D > 3.0 \text{ mm}^2/\text{s}$ ) that are considered to reflect the small cell component and perfusion, respectively [39].

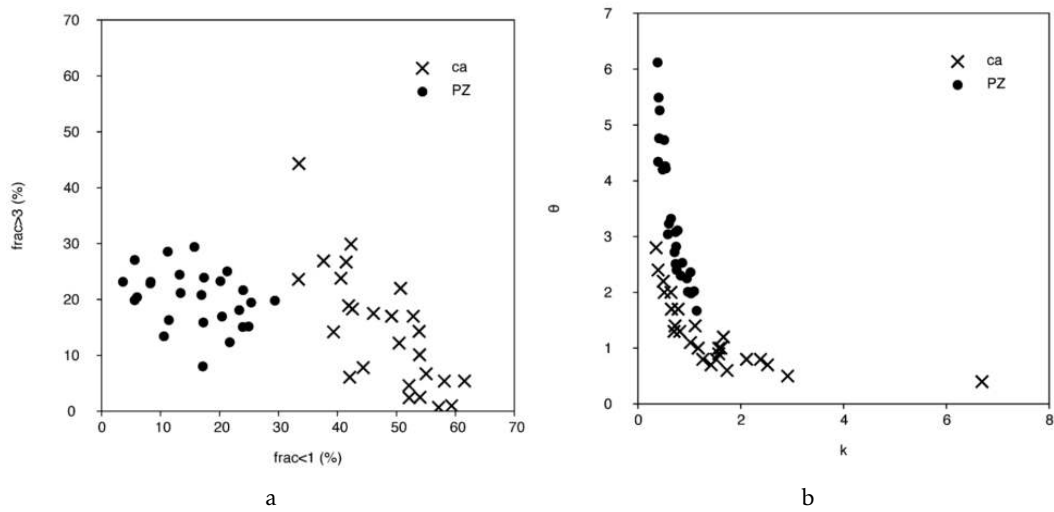


Figure 2.15: a) Scatter plot of  $\text{frac}>3$  vs  $\text{frac}<1$ ; b) Scatter plot of  $\theta$  vs  $\kappa$ ; for the cancer and not cancer group [39].

### 2.5.4 State-of-the-art of Truncated Gaussian Distribution

In a study done by Shinmoto et al. [16], the Truncated Gaussian distribution model was tested in prostate DW images. Shinmoto concluded that there are significant differences between a benign and malignant tumor on the parameters  $\sigma$  and ADC values. For a malignant tumor,  $\sigma$  and ADC have lower values than for a benign tumor.

Lee et al. [18] suggested that other models like Gamma and DKI may be used together with the truncated one, since they have different sensitivities, in order to study and further identify the underlying pathological mechanisms.

### 2.5.5 State-of-the-art of Stretched-Exponential

A study done by Liu et al. [17], where the stretched model was used to analyze DWI signals from prostate tissue, reveals that  $DDC$  and  $\alpha$  have characteristic values that help distinguish between normal and cancer tissues, with both parameters being significantly lower in prostate cancer in comparison with normal prostate tissue. As the truncated gaussian model, it has not yet been applied to breast MRI.



## MATERIALS AND METHODS

The main focus of this dissertation is to program an OsiriX plug-in that creates parametric maps based on non-Gaussian models of water diffusion. There are other plug-ins that produce parametric maps. However, they are not non-Gaussian and are only based on one model. This plug-in produces parametric maps of five different non-Gaussian models. In spite of the objective of the plug-in being to produce parametric maps, it was also added the ability to draw a Region Of Interest (ROI) around a tumor to obtain the parametric values of each model. Further it was also made available how many  $b$ -values and amount of noise alters the images, in order to inform the user on how to obtain better maps.

In this chapter the materials and methods to accomplish the dissertation's objective are presented .

### 3.1 Dataset and Acquisitions

The diffusion dataset used in this study for demonstrating the plug-in functionalities is made up of acquisitions of four different women with ages from 40 to 68 years old. The women of which the images were obtained had fibroadenomas, invasive ductal carcinomas or invasive ductal carcinomas in situ.

The images used in this study were obtained using an unilateral sagittal with single-shot spin-echo echo planar imaging (SS-SE-EPI) sequence and eight  $b$  values (50, 200, 400, 600, 800, 1000, 2000 and 3000  $\text{s}/\text{mm}^2$ ), with a 3-T system (Tim Trio; Siemens, Erlangen, Germany) and a four-channel bilateral breast coil. Patients positioned in the prone position. In order to generate three-scan-trace images, diffusion sensitizing gradients were applied in the  $x$ ,  $y$  and  $z$  directions. Because the sequence had higher  $b$ -values (2,000 and 3,000  $\text{s}/\text{mm}^2$ ) than normally used in the clinical practice, resulted in a longer TE of 106 ms.

Table 3.1: Sequence details for acquisition of the DWI images that were tested.

Parameters	DWI-SPAIR
Sequence	Single-shot EPI
Orientation	Sagittal
TR/TE (ms)	4900/106
Fat suppression	SPAIR
FOV (mm <sup>2</sup> )	250×250
Matrix	84×128
Slice thickness (mm)	5
Number of slices	16
NEX	3
Bandwidth (Hz/pixel)	1628
Scan time (min)	5:58
b-values (s/mm <sup>2</sup> )	50, 200, 400, 600, 800, 1000, 2000 and 3000

In Table 3.1 are all of the protocol details for acquisition. These images were on Digital Imaging and Communications in Medicine (DICOM) format, which comprises an image header with several attributes, such as name, series description,  $b$ -values, etc.

## 3.2 Image Processing Tools

The main tools used to build the plug-in were the Matlab software (Mathworks, Cambridge, UK.), OsiriX (Pixmeo SARL, Geneva, Switzerland) and Xcode. OsiriX is the most widely used DICOM viewer in the world and has the big advantage to have an intuitive interactive user interface. Matlab is a software with very complete function libraries, which in was used to receive data and to produce the parametric maps. Xcode was used to program the interface of the OsiriX plug-in and to be the bridge between Matlab and OsiriX. Another tool that was crucial for the development of the plug-in was OsiriX Plugin Generator that creates a new OsiriX plug-in template.

### 3.2.1 Producing parametric maps

The DWI was processed in Matlab as follows:

- Matlab has functions that are able to read DICOM images and obtain information about them. They are called *dicomread* and *dicominfo* and were used to load the images and organize them according to their slice location.
- In order for the plug-in to work with images acquired with Phillips or Siemens systems, it was what implemented a confirmatory check in the attribute manufacturer of the DICOM image. If it was written "SIEMENS", then the  $b$ -values would be in *info.Private\_0019\_100c*. However if it was a Phillips system, the  $b$ -values would be in *info.Private\_2001\_1003*.

- Because DWI images of the breast generally have low signal-to-noise ratio. In order to improve the quality of the obtained maps a smoothing filter (Wiener) with a neighborhood of 5x5 was used.
- The Levenberg-Marquardt algorithm was used with the Matlab function *lsqcurvefit* to fit the various non-Gaussian diffusion models. It starts at  $x_0$ , which are the initial guesses, and finds coefficients  $x$  to best fit the nonlinear function  $f(x, xdata)$  to the data  $ydata$  (in the least-squares sense). In this case,  $xdata$  are the  $b$  values and  $ydata$  are the images with the Wiener filter already applied.
- In order to evaluate if the curve fitting is being made successfully, the calculation of the goodness of fit was added. Goodness of fit describes how well a statistical model fits data. It was used the model R-square that is the square of the correlation between the response values and the predicted response values. R-square can only have values ranging from 0 to 1, being 1 the indication that the model explains all the variability of the response data. This way, the goodness of fit is evaluated through a parametric map which if it is mainly white, the R-squared values are proximate to 1 and if not, are close to 0.

In Matlab there is a option to obtain the residual  $ydata$  at the solution  $x$  in *lsqcurvefit*. The residual values are then used to obtain the goodness of fit with the R-squared model (Equation 3.1 used in Matlab)

$$GF = 1 - \text{resnorm} / \text{norm}(ydata - \text{mean}(ydata))^2 \quad (3.1)$$

- It was also given the user the opportunity to obtain these maps. This way a variable *GFvalue* will be given by the interface to matlab that will check if it is zero or one. If it is one it will produce the goodness of fit maps. Otherwise it will do nothing.
- After diffusion curve fitting, the parametric maps are saved in the OsiriX incoming folder through the Matlab function *dicomwrite*. Since OsiriX only reads integers values, information could be lost as the software will round up or down to unity whereas values are normally in the order of  $10^{-3} \text{mm}^2/\text{s}$ . Because of this, the maps were converted to 16 bit integers plus a suitable amount, for example, for MK it was plus 1000. All of the maps were tested in order to check the suitable amount of scaling factors in order to best see the image and its lesions. For the goodness of fit maps it was multiplied by 1000 to all of them. All the amounts that were multiplied are in Table 3.2.
- This process was then repeated for all of the five non-Gaussian models.
- In the Gamma model there was a step added in order to evaluate fractional areas for clinical evaluations like it was mentioned. It was used the *makedist* method which creates a probability distribution object with parameters  $k$  and  $\theta$ . Afterwords it was

Table 3.2: Scaling factors for each map on matlab in order for the maps to be correctly read by OsiriX. The units are also presented.

Parametric maps	Scaling factors	Units
<i>MD</i>	$1 \times 10^6$	$(\times 10^{-3} \text{mm}^2/\text{s})$
<i>MK</i>	$1 \times 10^3$	dimensionless
<i>D*</i>	$1 \times 10^6$	$(\times 10^{-3} \text{mm}^2/\text{s})$
<i>Dint</i>	$1 \times 10^6$	$(\times 10^{-3} \text{mm}^2/\text{s})$
<i>PF</i>	$1 \times 10^4$	%
$\theta$	$1 \times 10^4$	$(\times 10^{-3} \text{mm}^2/\text{s})$
$\kappa$	$1 \times 10^1$	dimensionless
<i>S1</i>	$1 \times 10^3$	%
<i>S2</i>	$1 \times 10^3$	%
<i>S3</i>	$1 \times 10^3$	%
$\sigma$	$1 \times 10^5$	$(\times 10^{-3} \text{mm}^2/\text{s})$
<i>ADC</i>	$1 \times 10^4$	$(\times 10^{-3} \text{mm}^2/\text{s})$
$\alpha$	$1 \times 10^4$	$(\times 10^{-3} \text{mm}^2/\text{s})$
<i>DDC</i>	$1 \times 10^7$	$(\times 10^{-3} \text{mm}^2/\text{s})$

used the *pdf* method that returns the probability density function for the gamma distribution evaluated at the values in *x*, which according to what was mentioned goes from 0 to 6 in intervals of 0.1.

- Because all of this processes are very time consuming, specially the *lsqcurvefit*, there was a need to shorten the running time of them. The solution that came across was parallel computing. Matlab has a toolbox that allows the user to create parallel for-loops in order to use the full processing power of multicore desktops by executing applications on workers that run locally [46]. The use of the *parfor* reduced the time for processing in half. The computer where the applications were tested was a Mac with a processor of 2.7 Ghz and an Intel Core i5.

Since Matlab isn't a free software, in order for the plug-in to work on every computer the Matlab compiler was used to create a standalone application. This means that the user only needs to install Matlab Runtime, which is free, to make the standalone application run on the users computer.

The rest of the plug-in was programmed in Objective-C, which is the language used on Xcode. It was written as follows:

- In the first place, the standalone application needs the path to the images. To do this it was created a class called *pathForRunning*. It uses the *ViewerController* class to detect which image of the series is being displayed in order to apply the *sourceFile* method that returns the path of every single image series. This information is then saved in a *NSMutableArray*. It is important to reference that when images are uploaded to OsiriX, the program automatically copies the images to its own folders, so the original images are never altered.



- In order for the user to have the chance of deciding if he wants a goodness of fit parametric map or not, a variable *GFvalue* was added that will connect with the respective checkbox.
- To call the standalone applications, the *runSystemCommand* class was used which was created with the purpose to execute a terminal command. This class receives a string *cmd* that contains the mutable array previously mentioned, the *GFvalue* variable and the command to execute the application.
- When the applications are done running, the images are uploaded to OsiriX through the INCOMING folder like it was mentioned before, and full dynamic palette is automatically applied. This is accomplished through an alert that warns the user that the process has finished. The alert has an OK button with an action that applies full dynamic to all of the images in every single series. The function that runs after the OK button is pressed is called *applyDynamic* and uses an OsiriX command called *setWLWW*.

### 3.2.2 Obtaining parametric values with a ROI

Processing the ROI values on Matlab:

- In this case, Matlab has the same methods as in 3.2.1. However there is a small change, instead of using the images, it uses the median values of the drawn ROI. This means that in the *lsqcurvefit* function, instead of *ydata* being the images with the Wiener filter, it is the ROI mean values of each slice. Since it cuts steps out, like applying the Wiener filter and saving maps, the time for processing each model was reduced drastically.
- After all of the parameters are obtained, they are going to be saved in a .txt file with the help of the function *fprintf*. This file will be saved in the TEMP folder of OsiriX, that as the name suggests, is for temporary files that are deleted after closing the program.
- In this case there is also the chance to obtain the goodness of fit of the data. Since the user chooses the area on which the models will run, there won't be a parametric map with the goodness of fit. Instead, the user will obtain a value from 0 to 1 and also a plot on which he will evaluate how well the data is fitted.

Like it was mentioned in 3.2.1, these functions were all made into standalone applications with the help of Matlab Compiler.

In this case, the part that was programmed in Objective-C had more steps because it was dealing with ROIs. These steps are:

- Firstly, the user only has to draw one ROI around the tumor area. However, in order to do the curve fitting on Matlab, it needs the values of the ROI from the same slice

in every  $b$  value. This means that the plug-in has to know in which slice the ROI was drawn. In order to do this, it was created a class called *sliceLoc* which detects the slice location of where the ROI was drawn with the help of the *ViewerController* class and *DCMObject* that offers a way to access the data for a given DICOM tag.

- Afterwords, the ROIs were copied to the images with the same slice. For this functionality it was created a class called *ROIS* which copied the ROIs but also prevented them from being pasted in an image that already had the same ROI, which would happen if the user would like to run the models more than once with the exact same ROI. In all of the classes and methods that were used, *NSRegularExpression* and *computeROI* stand out. *NSRegularExpression* has a method called *numberOfMatchesInString* that counts the number of matches in a given range of a string. It was used to check if the image already had the ROI and it works with every single ROI that can be drawn in OsiriX (oval, rectangle, etc). It also doesn't mix up with other ROIs that the image can have. The method *computeROI* obtains all of the information about the ROI, but the only information needed was the *rmean* which is the mean value of a ROI.
- The next step was very similar to 3.2.1 to call the applications. The only difference is that in this case it also had to pass a string with the mean values.
- After the application is done running, the information on the .txt file on the TEMP folder is inserted into the text fields that are on the plug-in interface. The class that does this is called *showTEXT* and it reads the .txt files with the method *stringWithContentsOfFile*. It then saves the information to a string that is then placed on the respective text fields.
- In the end, the user gets to save the data acquired or delete everything including the ROI. This was made with two classes, the *writeUsingSavePanel* and *resetpi*. *writeUsingSavePanel* uses the *writeToFile* method to save the data into a txt file in the location that user chooses through an open dialog box. *resetpi* uses the *NSFileManager* class to remove the files from the TEMP file with the method *removeItemAtPath* and also erases the text fields by changing the labels to an empty string.

### 3.3 Testing the plug-in in images with different $b$ -values and noise

#### 3.3.1 Different $b$ values

This was an important task since the amount of  $b$ -values can change a map drastically and depends on the acquisition protocol used. It is evident that various different  $b$ -values gives a more precise map [12]. However, which  $b$ -values are used alter the image even

### 3.3. TESTING THE PLUG-IN IN IMAGES WITH DIFFERENT $b$ -VALUES AND NOISE

---

more than having low numbers of  $b$ -values. This happens because certain models work best with higher  $b$ -values and others the other way around. For example, IVIM requires lower  $b$ -values than while DKI requires larger  $b$  values. Because the IVIM model is tested with a smaller amount of  $b$  values, the combinations of tested  $b$  values is different from the other models.

Therefore, in order to test how the  $b$ -values and their amount affects the efficiency of the models, the following combination of  $b$  values was tested:

1. It was removed one  $b$ -value, which was 600 s/mm<sup>2</sup>. Making a total of 7  $b$ -values, 50, 200, 400, 800, 1000, 2000 and 3000 s/mm<sup>2</sup>.
2. The 2000 s/mm<sup>2</sup> was removed. Making a total of 6  $b$ -values, 50, 200, 400, 800, 1000 and 3000 s/mm<sup>2</sup>.
3. The 200 s/mm<sup>2</sup> was removed. Making a total of 5  $b$ -values, 50, 400, 800, 1000 and 3000 s/mm<sup>2</sup>.
4. The 800 s/mm<sup>2</sup> was removed. Making a total of 4  $b$ -values, 50, 400, 1000 and 3000 s/mm<sup>2</sup>.
5. The 1000 s/mm<sup>2</sup> was removed. Making a total of 3  $b$ -values, 50, 400 and 3000 s/mm<sup>2</sup>.

In case of the IVIM model, the following  $b$  values were tested. Because the IVIM model has four free parameters, it was only one  $b$  values removed for each test.

1. It was removed one  $b$ -value, which was 600 s/mm<sup>2</sup>. Making a total of 4  $b$ -values, 50, 200, 400, 800 s/mm<sup>2</sup>.
2. The 400 s/mm<sup>2</sup> was removed. Making a total of 4  $b$ -values, 50, 200, 600, 800 s/mm<sup>2</sup>.
3. The 200 s/mm<sup>2</sup> was removed. Making a total of 4  $b$ -values, 50, 400, 600, 800, 1000 and 3000 s/mm<sup>2</sup>.
4. The 800 s/mm<sup>2</sup> was removed. Making a total of 4  $b$ -values, 50, 200, 400, 800 s/mm<sup>2</sup>.
5. The 50 s/mm<sup>2</sup> was removed. Making a total of 4  $b$ -values, 200, 400, 600, 800s/mm<sup>2</sup>.

In order to test with the different amount of  $b$ -values, the images were selected before being uploaded to OsiriX. Afterwards, the plug-in was applied and the images were exported in order to be compared.

### 3.3.2 Different amount of noise

Noise is one of the biggest concerns in image processing. If there is a big amount of noise, the image can lose valuable information. In 3.2.1 it was referred that a filter is applied to the images before being processed. However, this filter can't be of value if the images are noisy. In order to inform the user about the amount of noise that still produces a good map, several amounts were added to the images.

In order to better evaluate how the noise affects the images, the parameters of the DKI model were used in the equation 2.4 to obtain images that had no noise and with known fitting values. The method to add the noise was called *randn* and is a matlab function that produces random normally distributed matrices. After these matrices were created, they were added to the image, creating the noise. The amount that was added was in increments of 5%. Which means that firstly 5% of noise was added, then 10% of noise and so on. In the end, after reaching 35% of noise, it was stopped since the image had lost so much information that the tumor was no longer visible.

## RESULTS AND DISCUSSION

The results will be presented in this chapter as for the discussion as well. At first will be presented and discussed the interface and results of the plugin for the parametric maps and then, also, of the parametric values obtained with ROIs. In order to better inform the user about what kind of images he is advised to use in order to obtain the best results as possible, it was also tested for how many  $b$  values and from how much noise the resulting maps will start to loose quality.

In the parametric maps, are always two images shown, greyscale and color ("jet" CLUT). "Jet" Color Look Up Table ( Color Look Up Table (CLUT)) assigns colors and opacity values based upon the images greyscale values.

The analysis made to the parametric maps was qualitative and to the parametric values was quantitative. One advantage of producing a great amount of maps is that a ROI can be drawn in a map where the lesion is clearly seen and be placed in a map where it isn't as clear. This can help in the study of these images since the user will know the location of the tumor.

### 4.1 Parametric maps

#### 4.1.1 Interface

The final look of the plug-in is shown in Figure 4.1. On the left side of the plugin are the check boxes to obtain the parametric maps for non-Gaussian models (DKI, IVIM, Gamma, Truncated and Stretched). The user gets a chance to obtain all of the maps or only a few of them. He also gets the choice to decide if he wants maps of goodness-of-fit for the models or not. If he selects the "OK" button without selecting any model a warning will appear for him to choose one, like it is shown on Figure 4.2. In case the user is trying to run the models on parametric maps and not on DWI images, the Figure 4.3 of the warning

appears. While, the applications are running and the images aren't uploaded to OsiriX, a "Please wait..." window appears (Figure 4.4).

In Figure 4.5 there is a help button with a question mark. When the user presses this window it will appear the scaling factor that was used for which parametric map like it was mentioned in section 3.2.1 and also the references of the models that were used.

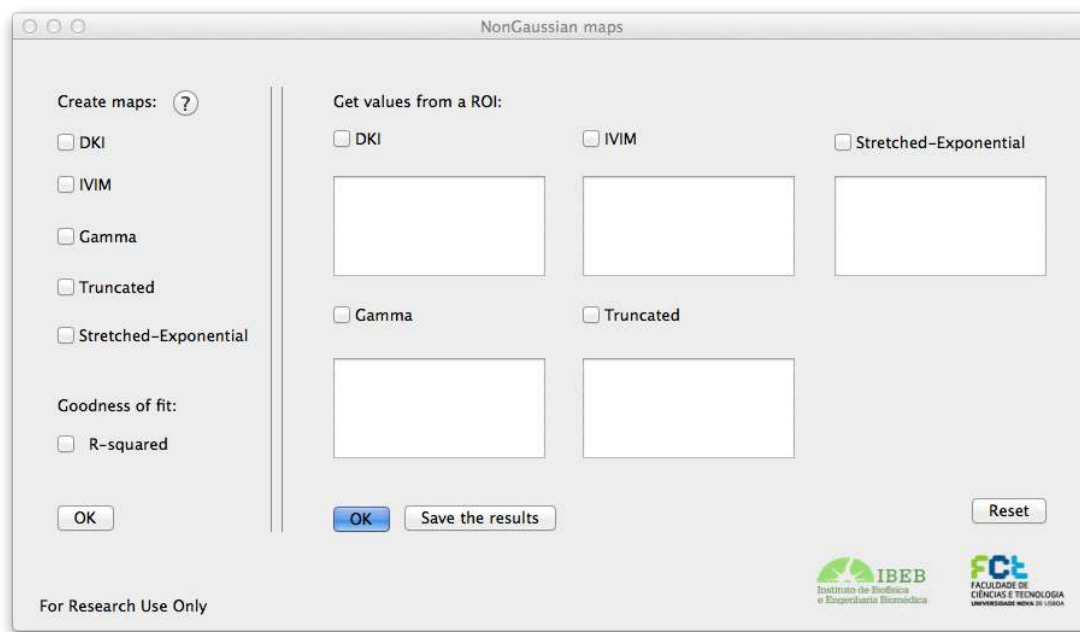


Figure 4.1: Interface of the plug-in.



Figure 4.2: Warning that appears when the user presses the "OK" button, next to the parametric maps check boxes, and doesn't select which model to run.

After the applications are done running, an alert window appears warning the user that the process is completed (Figure 4.6). The OK button of the warning has an action which applies the full dynamic to all of the series of maps that are now being uploaded to OsiriX. This action was created because the upload of the maps to OsiriX occurs by saving the images on the programs INCOMING folder. And because full dynamic is a crucial step (it adapts the grayscale of the image with the help of the image upper and



Figure 4.3: Warning that appears when the user trys to run the models on a parametric map and not a DWI image.

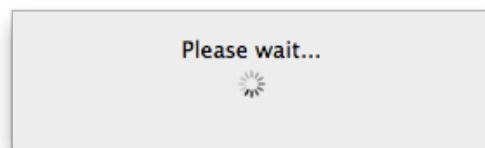


Figure 4.4: Window that alerts the user to wait while the program is running.

lower range), it's easier if it is applied to all of the images at once. In case the user presses the "Cancel" button, the images will not be uploaded.

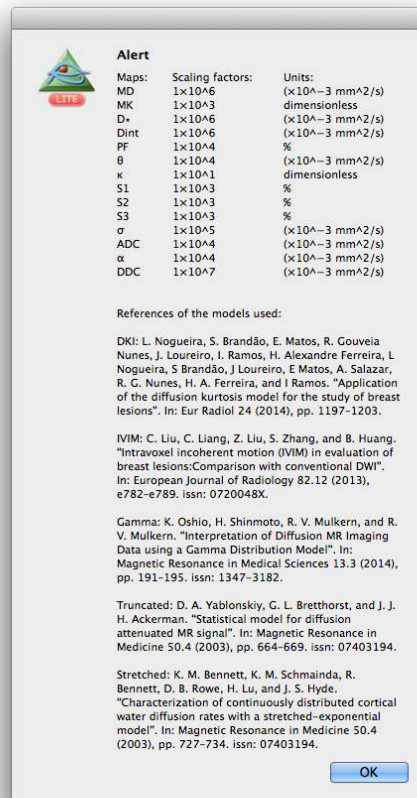


Figure 4.5: Window that informs the user on the amount that was multiplied to which image and also the references of the models that were used.

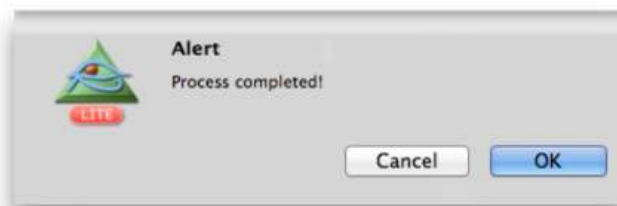


Figure 4.6: Window that alerts the user that the process to produce parametric maps is complete. If the "OK" button is pressed, the images are uploaded to OisriX and full dynamic is automatically applied.

#### 4.1.2 DKI parametric maps

As it was mentioned in 4.1.1, the plugin gives the user the opportunity to obtain different maps from five different models. The first model returns two different parametric maps, the "MD" and the "MK".

In the *MD* map, the tumor appears darker and in the *MK* map lighter, as it was predicted to happen since *MD* values are lower and *MK* values are higher in malignant



lesions than in benign lesions and healthy parenchyma, as it was mentioned in 2.5.1. Therefore, a high MK value demonstrates a deviation from the Gaussian curve, meaning that the tumoral tissue has a complex architecture and is rich in barriers such as cellular membranes. In the MK map is also easily seen tumor heterogeneity.

The average amount of time that it took to process the DKI parametric maps was 115 seconds without parallel computing and 50 seconds with parallel computing.

#### 4.1.2.1 Malignant lesions

The diffusion-weighted image and the diffusion-weighted image with the "Wiener" filter applied, with the  $b$  value of  $50 \text{ s/mm}^2$ , of a breast with malignant tumor (invasive ductal carcinoma) are represented in Figure 4.7 (these images are not obtained through the plug-in). In all three images, the detection of the tumor is relatively difficult. However, when the DKI model is applied, the tumor is clearly seen (Figures 4.8 and 4.9).

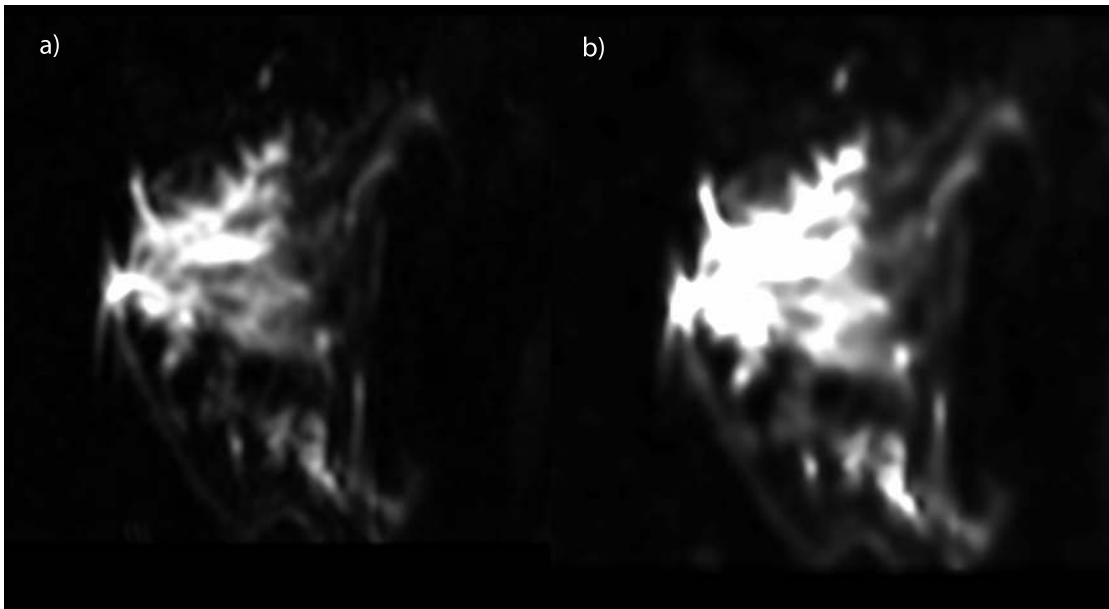


Figure 4.7: Images of a breast with malignant tumor (invasive ductal carcinoma): a) DWI image with the  $b$  value  $50 \text{ s/mm}^2$ ; b) DWI image with the Wiener filter applied.

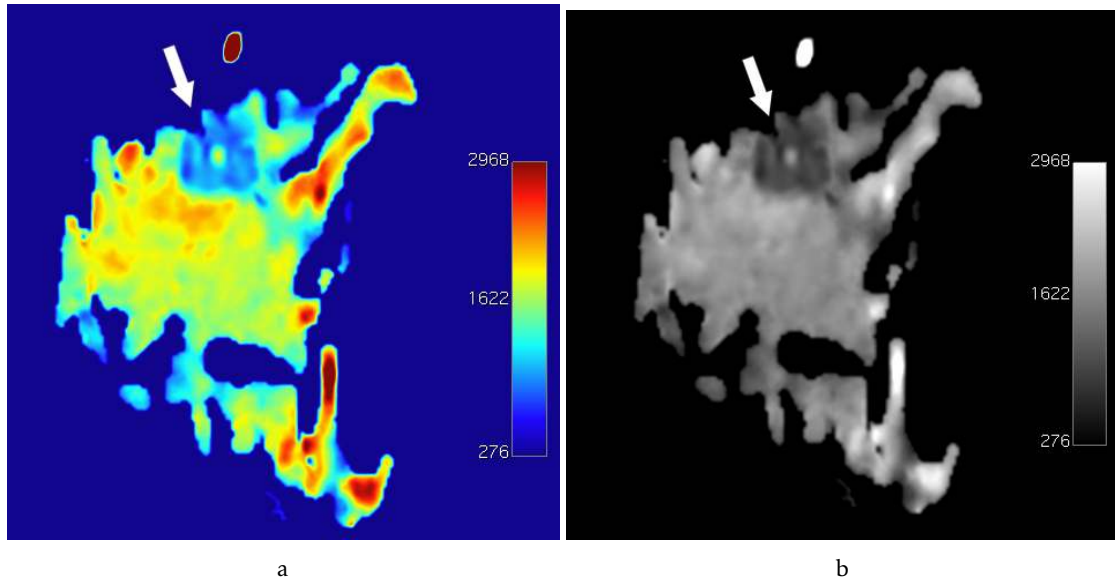


Figure 4.8: *MD* parametric maps (scaling factor of  $1 \times 10^6$  and in  $\text{mm}^2/\text{s}$ ) with an arrow indicating a malignant lesion (invasive ductal carcinoma) in dark blue with "jet" CLUT applied (a) and in grayscale (b).

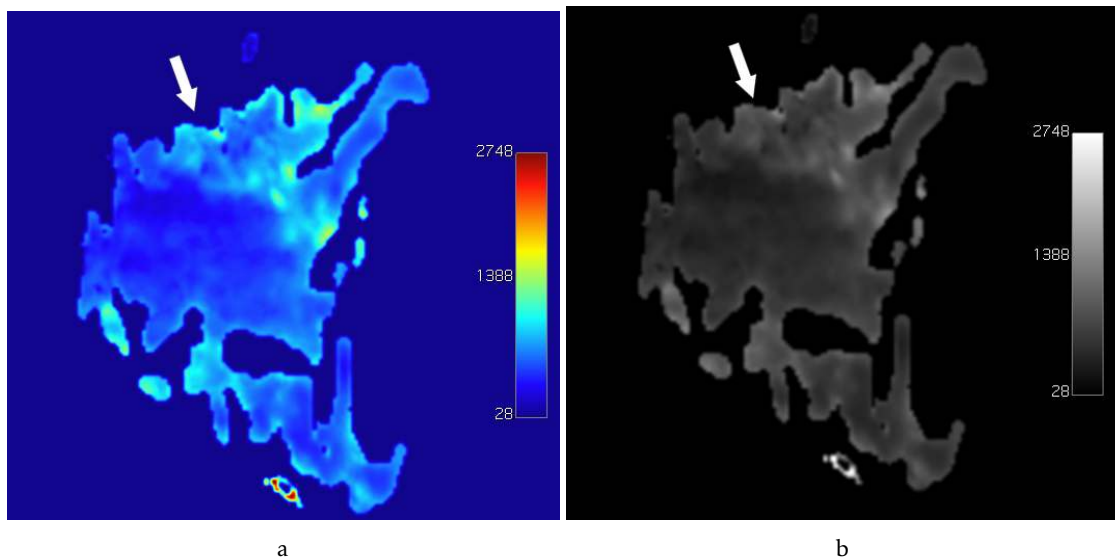


Figure 4.9: *MK* parametric maps (scaling factor of  $1 \times 10^3$  with no units since it is dimensionless) with an arrow indicating a malignant lesion (invasive ductal carcinoma) in light blue with "jet" CLUT applied (a) and in grayscale (b).

#### 4.1.2.2 Benign lesions

In Figure 4.10 and 4.11 the *MD* and *MK* maps of a breast with a benign tumor (fibroadenoma) are shown. The dark red that appears on Figure a) of the *MD* map (4.10) are actually the lighter areas on the image as you can see when you compare both of them. And the dark blue that appears on Figure b) of the *MK* map (4.11) is the darkest area of

the image. These two images are in agreement with the literature since in a benign lesion, the  $MD$  values are higher and  $MK$  values are lower than in malignant tissues. Because  $MK$  is a low value, it becomes very similar to the Gaussian shape, meaning more diffusion which concludes that it is a benign lesion.

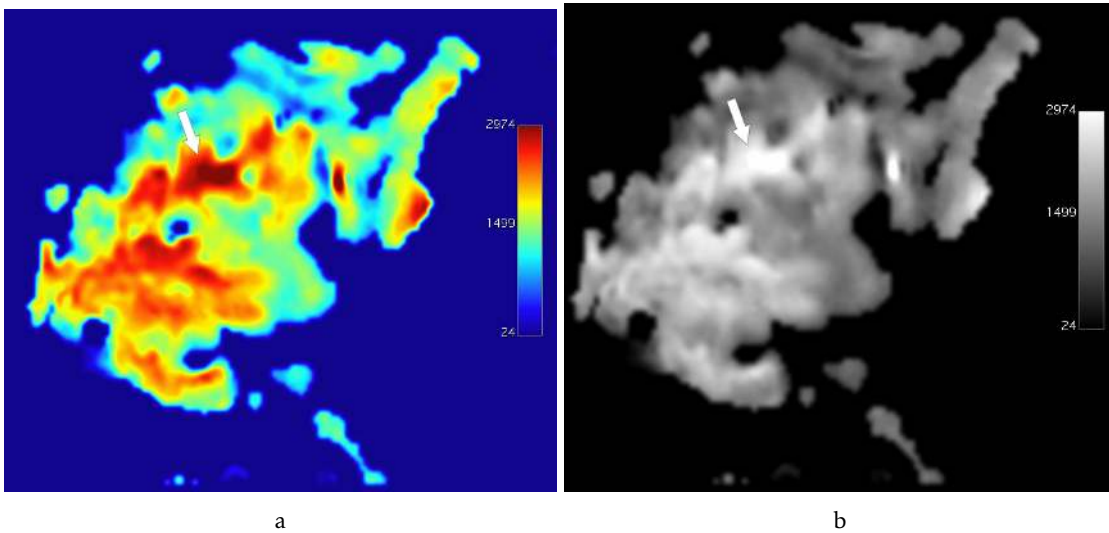


Figure 4.10:  $MD$  parametric maps (scaling factor of  $1 \times 10^6$  and in  $\text{mm}^2/\text{s}$ ) with an arrow indicating a benign lesion (fibroadenoma) in dark red with "jet" CLUT applied (a) and in grayscale (b).

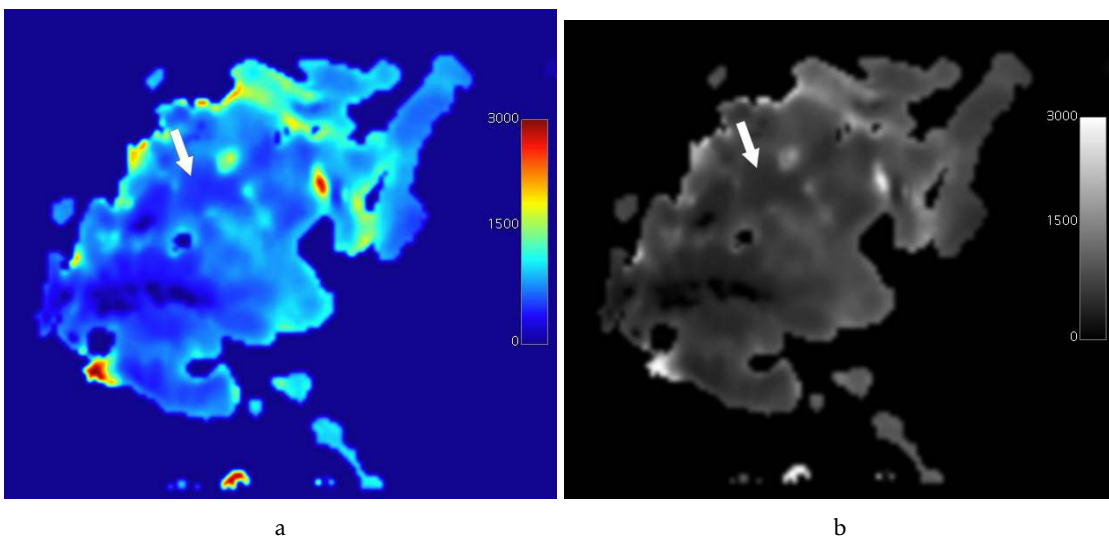


Figure 4.11:  $MK$  parametric maps (scaling factor of  $1 \times 10^3$  and with no units since it is dimensionless) with an arrow indicating a benign lesion (fibroadenoma) in dark blue with "jet" CLUT applied (a) and in grayscale (b).

### 4.1.3 IVIM parametric maps

The second model on the interface is the IVIM model. With this model the user gets three different parametric maps, the  $D^*$  map,  $D_{int}$  map and  $PF$  map. Because, as it was mentioned in 2.3.2, this technique uses low  $b$ -values and the images that were tested started at the  $b$ -value  $50 \text{ s/mm}^2$ , which can explain the low quality of some maps, like the  $D^*$  map. Since the  $b$  values aren't the most appropriate for testing the IVIM model, the IVIM/DKI model didn't show a good enough curve fitting of the data, so it was not added to the plug-in.

The maps that were obtained are in agreement with literature since, the parametric values for the benign lesions are higher than for the malignant lesions, which explains why the benign lesion appears lighter and the malignant lesion darker.

The average amount of time that it took to process the IVIM parametric maps was 240 seconds without parallel computing and 140 seconds with parallel computing.

#### 4.1.3.1 Malignant lesions

In Figures 4.12, 4.13 and 4.14 the  $D^*$ ,  $D$  and  $f$  maps are shown. In the  $D$  map the lesion is very clear. However, the  $PF$  and  $D^*$  maps weren't able to show the lesion as perfectly as  $D$ , which could be expected since its specificity and sensibility are significantly lower. In the  $D$  map is also easily seen tumor heterogeneity. In the  $f$  maps the higher values are around the tumor area which can mean that is high vascularized which is typical in neogenesis process [47].

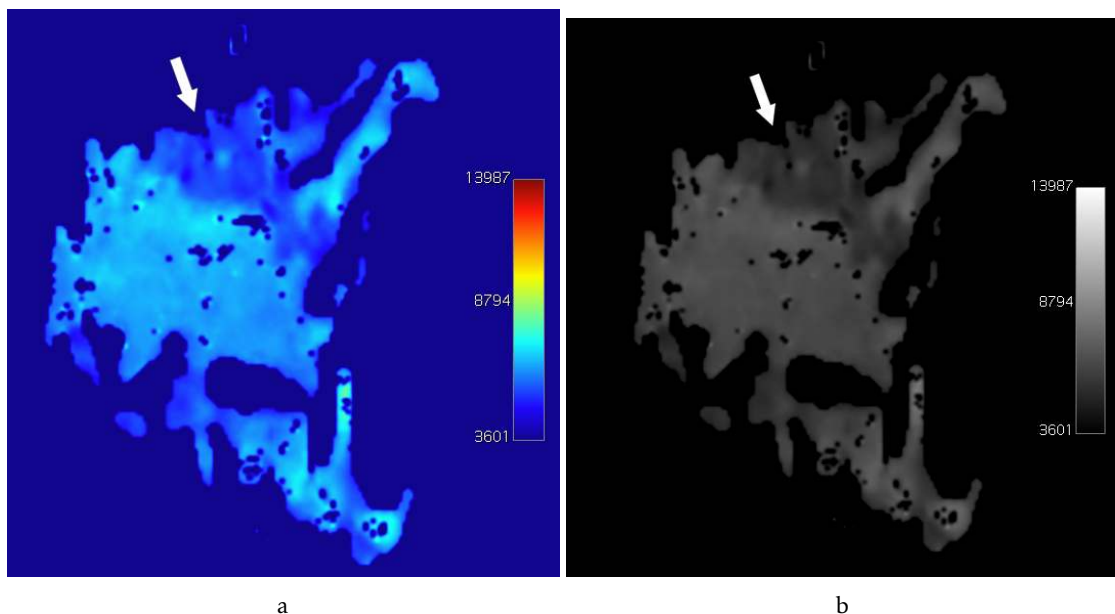


Figure 4.12:  $D^*$  parametric maps (scaling factor of  $1 \times 10^6$  and in  $\text{mm}^2/\text{s}$ ) with an arrow indicating a malignant lesion (invasive ductal carcinoma) in dark blue with "jet" CLUT applied (a) and in grayscale (b).

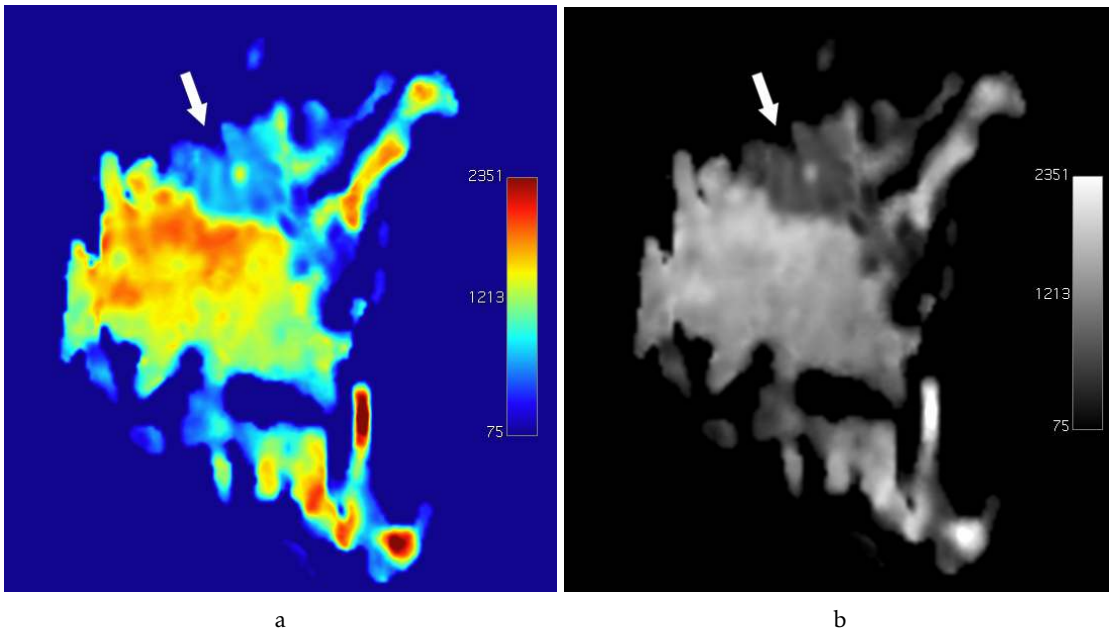


Figure 4.13:  $D$  parametric maps (scaling factor of  $1 \times 10^6$  and in  $\text{mm}^2/\text{s}$ ) with an arrow indicating a malignant lesion (invasive ductal carcinoma) in blue with "jet" CLUT applied (a) and in grayscale (b).

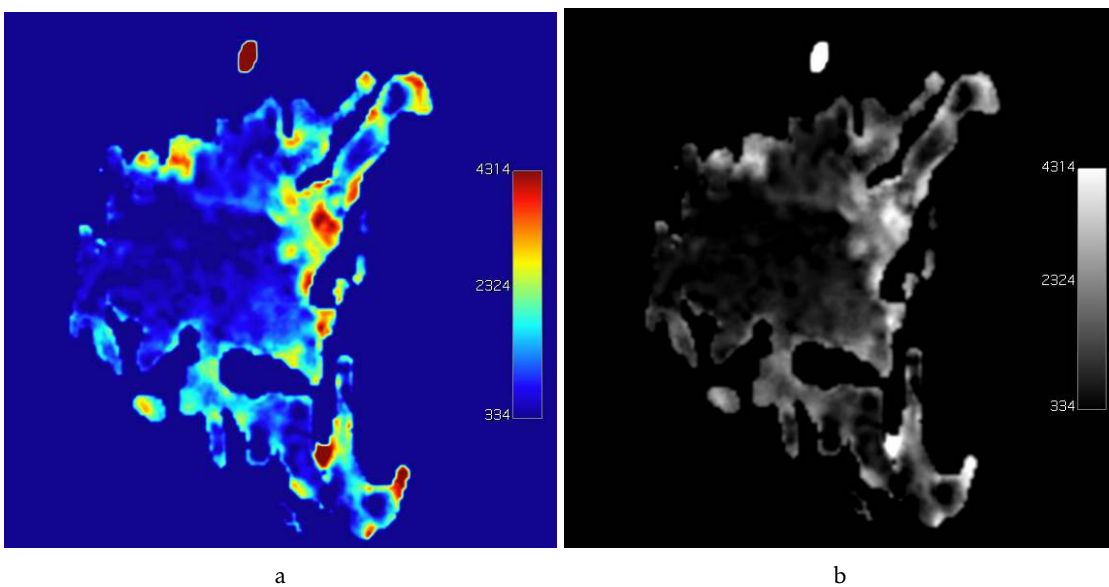


Figure 4.14:  $f$  parametric maps (scaling factor of  $1 \times 10^4$  and in %) that show higher values of perfusion around the tumor area with "jet" CLUT applied (a) and in grayscale (b).

### 4.1.3.2 Benign lesions

In Figures 4.15, 4.16 and 4.17 the  $D^*$ ,  $D$  and  $f$  maps are shown. On the  $D$  map the lesion is very clear. However, the  $f$  and  $D^*$  maps weren't able to show the lesion as perfectly as  $D$ , as it was also seen in the malignant images. Also, the  $f$  map shows a lighter area that does not correspond to the tumor which could be justified by high perfusion.

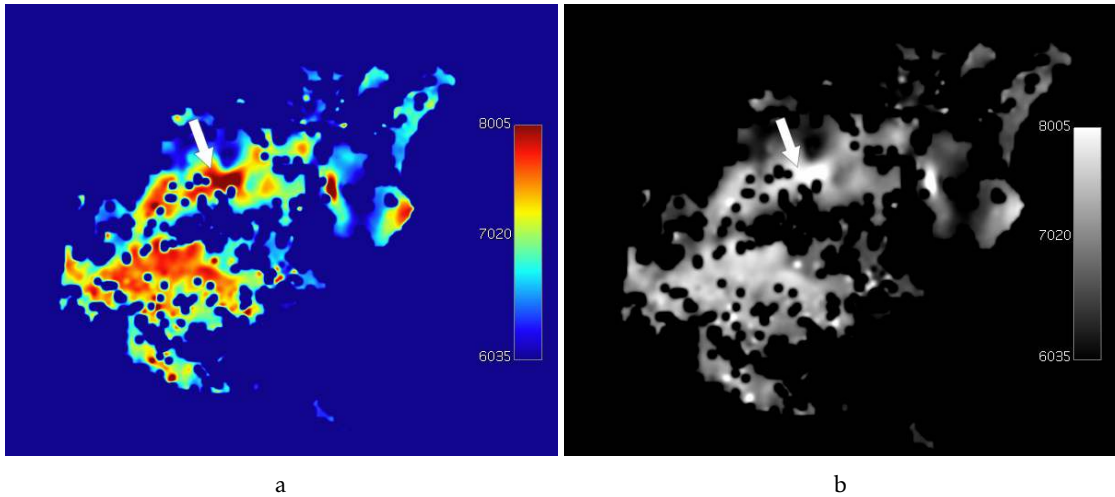


Figure 4.15:  $D^*$  parametric maps (scaling factor of  $1 \times 10^6$  and in  $\text{mm}^2/\text{s}$ ) with an arrow indicating a benign lesion (fibroadenoma) in dark red with "jet" CLUT applied (a) and in grayscale (b).

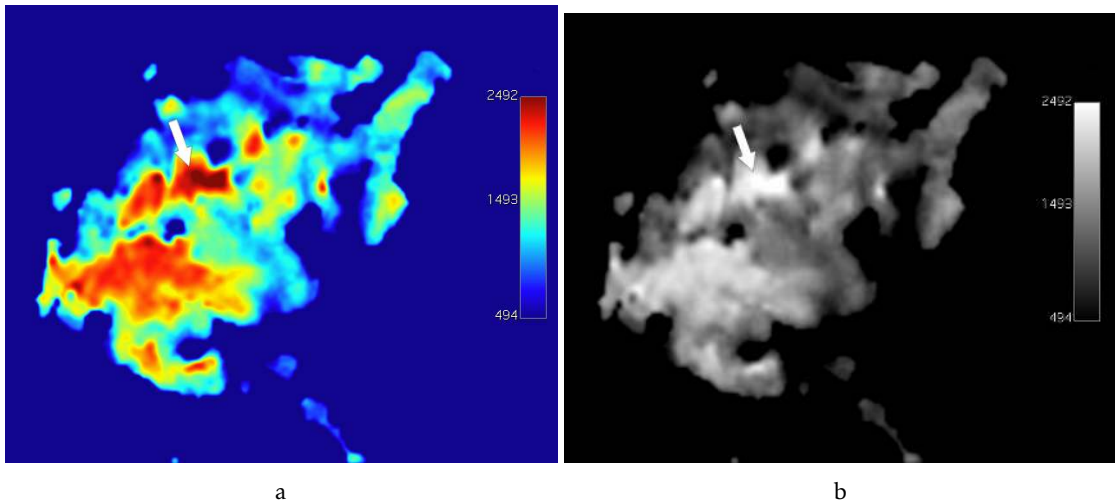


Figure 4.16:  $D$  parametric maps (scaling factor of  $1 \times 10^6$  and in  $\text{mm}^2/\text{s}$ ) with an arrow indicating a benign lesion (fibroadenoma) in dark red with "jet" CLUT applied (a) and in grayscale (b).

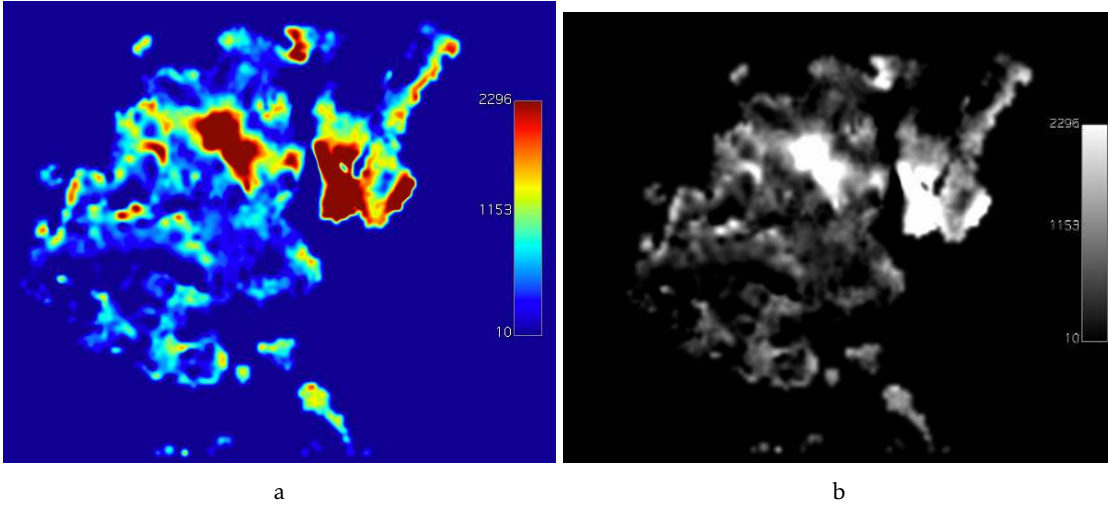


Figure 4.17:  $f$  parametric maps (scaling factor of  $1 \times 10^4$  and in %) that show high diffusion near the tumor area with "jet" CLUT applied (a) and in grayscale (b).

#### 4.1.4 Gamma parametric maps

The third model is the Gamma model. With it, the user obtains five different parametric maps the  $\theta$  map,  $\kappa$  map, S1 map, S2 map e S3 map. According to literature, the malignant lesions have higher  $\theta$  values and lower  $\kappa$  values, which is verified in the following images.

The average amount of time that it took to process the Gamma parametric maps was 240 seconds without parallel computing and 210 seconds with parallel computing.

##### 4.1.4.1 Malignant lesions

On the  $\theta$  maps (Figure 4.18) and  $\kappa$  maps (Figure 4.19), the typical values for a tumor match the ones on the parametric map (the tumor area has lower values in  $\theta$  than in  $\kappa$ ). In case of the S1, S2 and S3 maps, the values for the first map are supposed to be significantly higher than the ones for the S3 map, which is confirmed in the Figures 4.20, 4.21 and 4.22. According to literature mentioned in 2.5.3, the S1 map is the one that better shows the tumor area which can be seen in the Figures. Also, the S1 map shows tumoral heterogeneity.

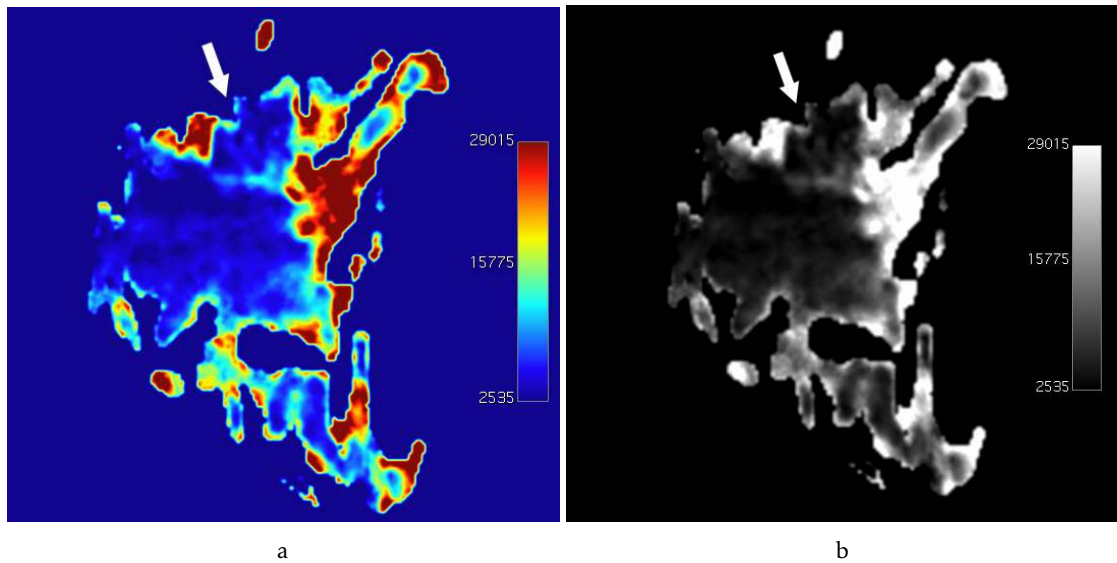


Figure 4.18:  $\theta$  parametric maps (scaling factor of  $1 \times 10^4$  and in  $\text{mm}^2/\text{s}$ ) with an arrow indicating a malignant lesion (invasive ductal carcinoma) with "jet" CLUT applied (a) and in grayscale (b).

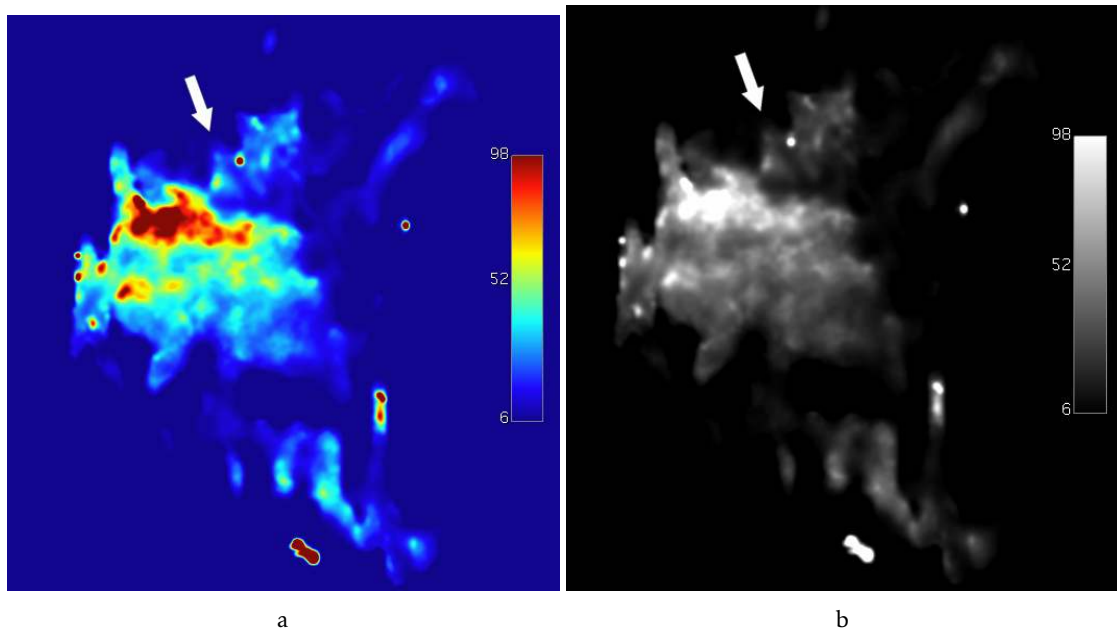


Figure 4.19:  $\kappa$  parametric maps (scaling factor of 10 and with no units since it is dimensionless) with an arrow indicating a malignant lesion (invasive ductal carcinoma) with "jet" CLUT applied (a) and in grayscale (b).



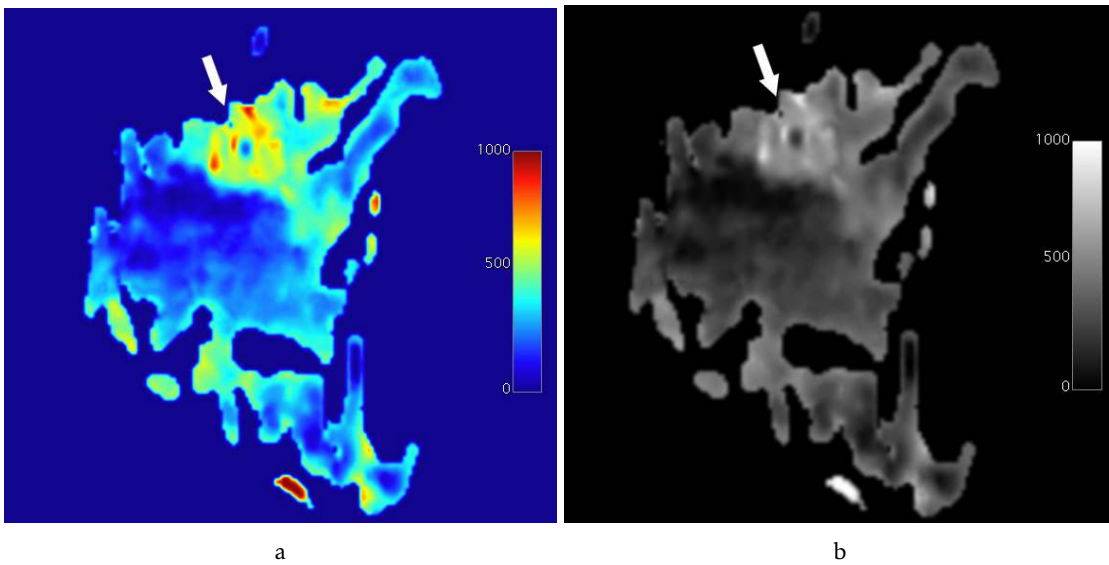


Figure 4.20: S1 parametric maps (scaling factor of  $1 \times 10^3$  and in %) with an arrow indicating a malignant lesion (invasive ductal carcinoma) with "jet" CLUT applied (a) and in grayscale (b).

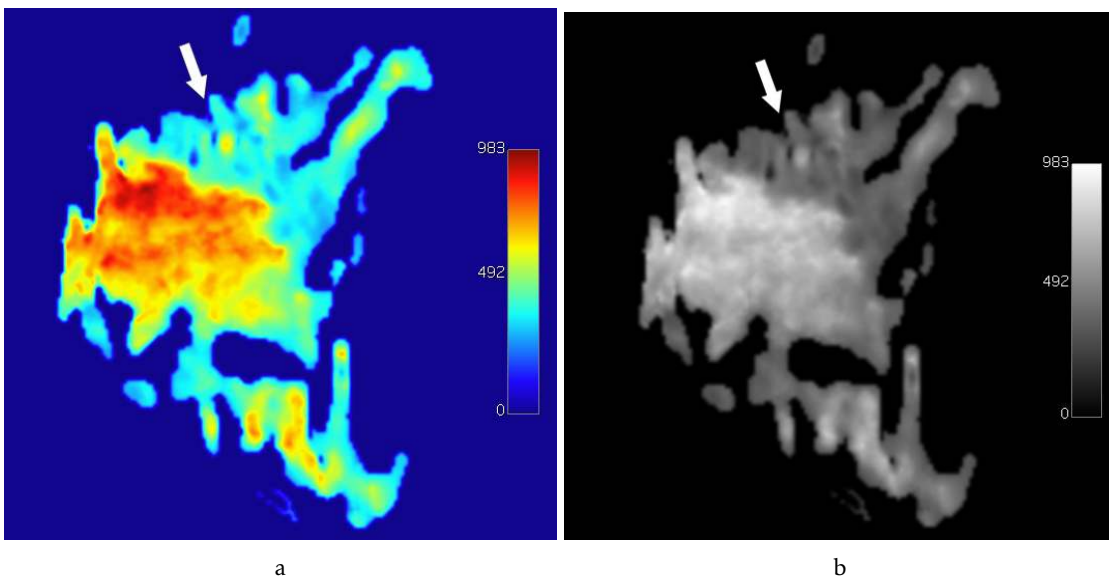


Figure 4.21: S2 parametric maps (scaling factor of  $1 \times 10^3$  and in %) with an arrow indicating a malignant lesion (invasive ductal carcinoma) with "jet" CLUT applied (a) and in grayscale (b).

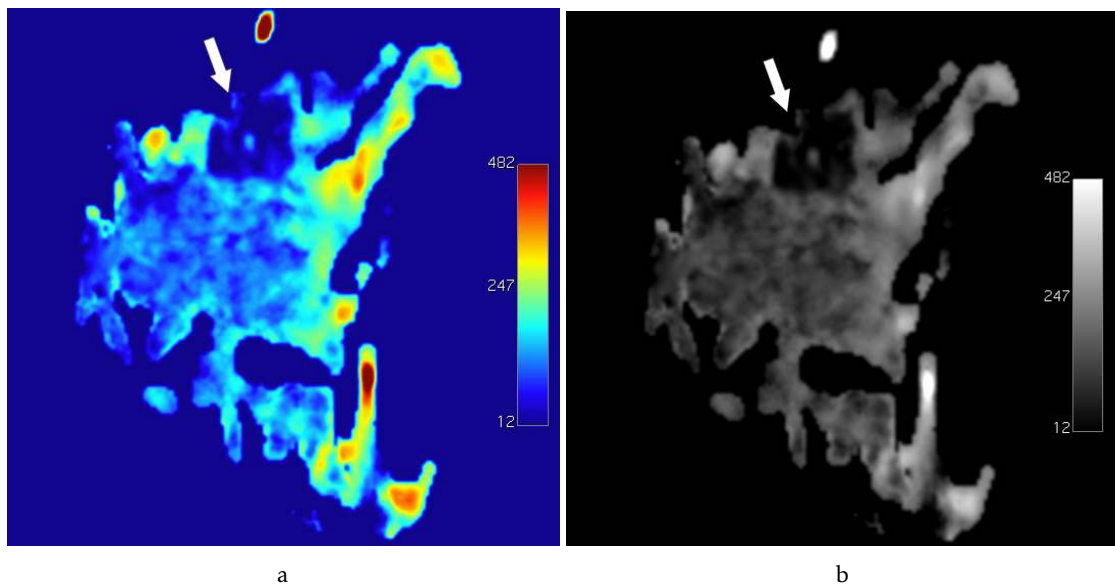


Figure 4.22: S3 parametric maps (scaling factor of  $1 \times 10^3$  and in %) with an arrow indicating a malignant lesion (invasive ductal carcinoma) with "jet" CLUT applied (a) and in grayscale (b).

#### 4.1.4.2 Benign lesions

On the  $\theta$  maps (Figure 4.23) and  $\kappa$  maps (Figure 4.24), the typical values for a tumor match the ones on the parametric map (the tumor area has lower values in  $\theta$  than in  $\kappa$ ). In case of the S1, S2 and S3 maps, the first two maps show lower values than the S3 map, which means that there is a low restriction to diffusion confirming that it is a benign tumor. The high values on the S3 map indicate that the lesion has high perfusion.

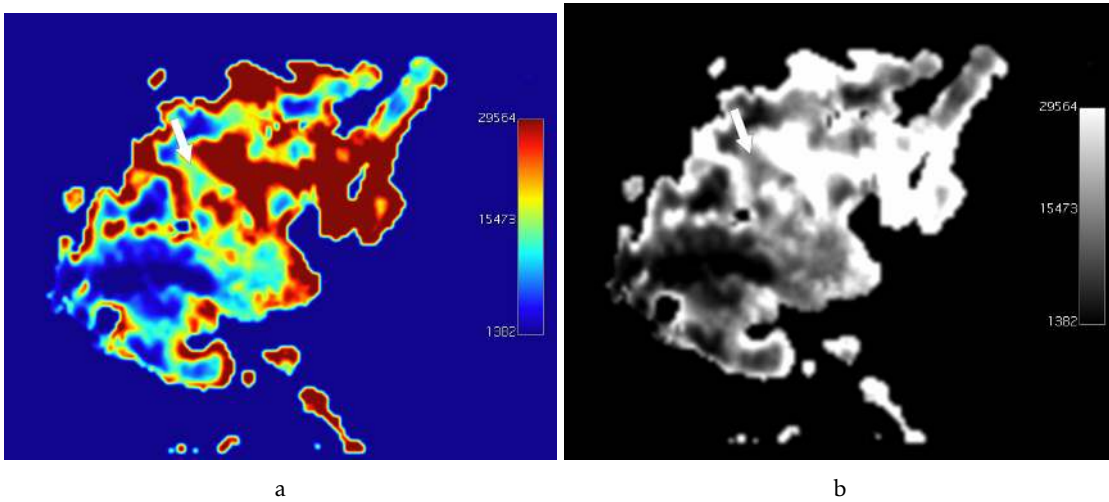


Figure 4.23:  $\theta$  parametric maps (scaling factor of  $1 \times 10^4$  and in  $\text{mm}^2/\text{s}$ ) with an arrow indicating a benign lesion (fibroadenoma) with "jet" CLUT applied (a) and in grayscale (b).

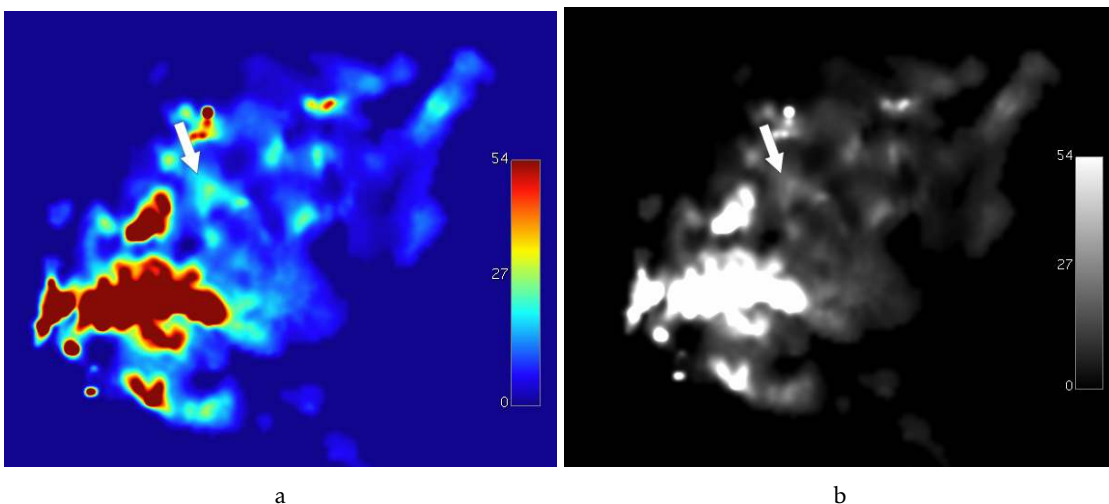


Figure 4.24:  $\kappa$  parametric maps (scaling factor of 10 and with no units since it is dimensionless) with an arrow indicating a benign lesion (fibroadenoma) with "jet" CLUT applied (a) and in grayscale (b).

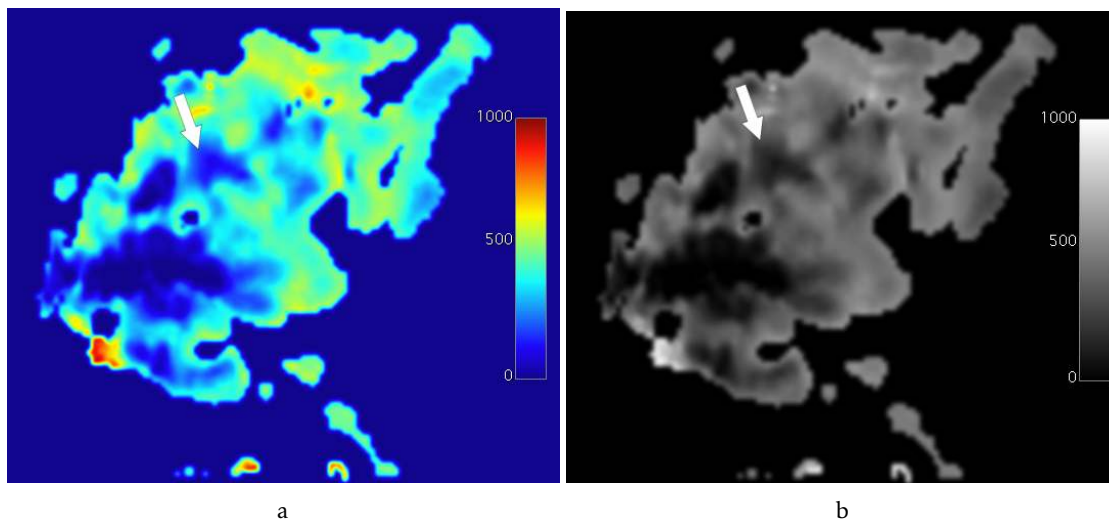


Figure 4.25: S1 parametric maps (scaling factor of  $1 \times 10^3$  and in %) with an arrow indicating a benign lesion (fibroadenoma) with "jet" CLUT applied (a) and in grayscale (b).

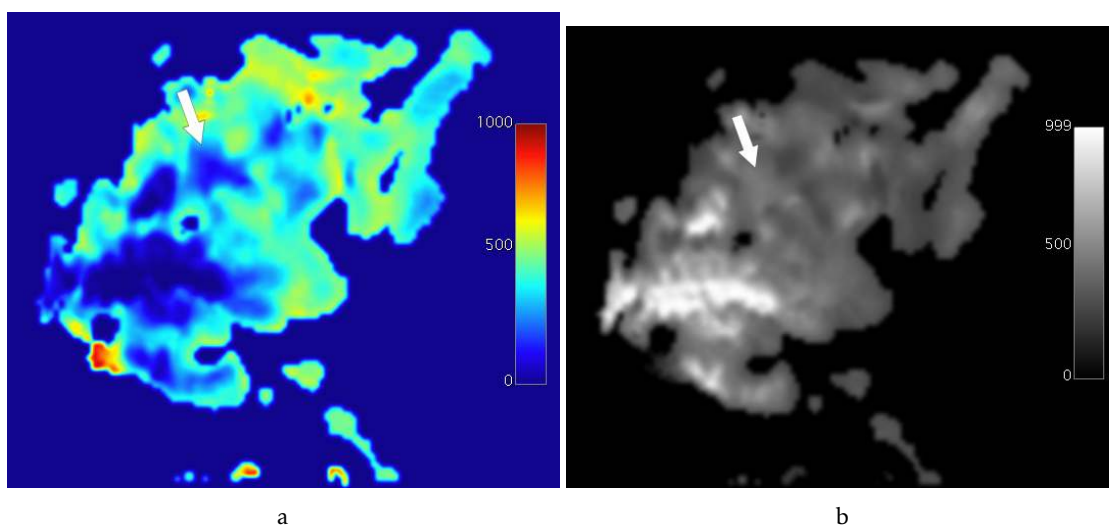


Figure 4.26: S2 parametric maps (scaling factor of  $1 \times 10^3$  and in %) with an arrow indicating a benign lesion (fibroadenoma) with "jet" CLUT applied (a) and in grayscale (b).

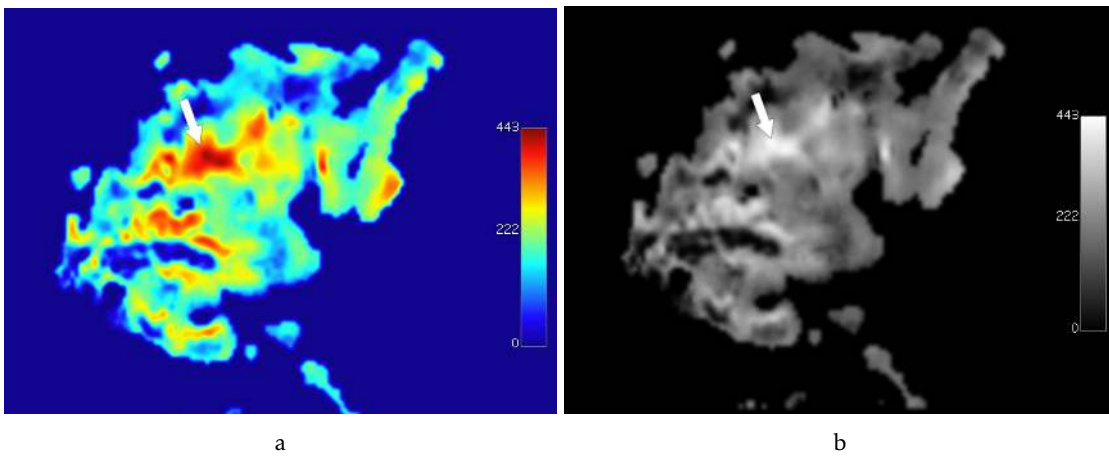


Figure 4.27: S3 parametric maps (scaling factor of  $1 \times 10^3$  and in %) with an arrow indicating a benign lesion (fibroadenoma) with "jet" CLUT applied (a) and in grayscale (b).

### 4.1.5 Truncated parametric maps

The fourth model is the Truncated model. With it, the user obtains two different maps, the  $\sigma$  map and the  $ADC$  map. Since there still aren't any studies of this model applied to the breast, the standard values of a malignant tumor are still unknown. However, it has been applied to prostate and in that study, both the  $ADC$  and  $\sigma$  values were higher in benign lesions than in malignant lesions, which is also seen in the following images, meaning that the model was able to distinguish between malignant and benign lesions.

The average amount of time that it took to process the Truncated parametric maps was 105 seconds without parallel computing and 74 seconds with parallel computing.

#### 4.1.5.1 Malignant lesions

In both of the maps,  $\sigma$  (Figure 4.28) and  $ADC$  (Figure 4.29), the malignant lesion (invasive ductal carcinoma) is clearly seen.

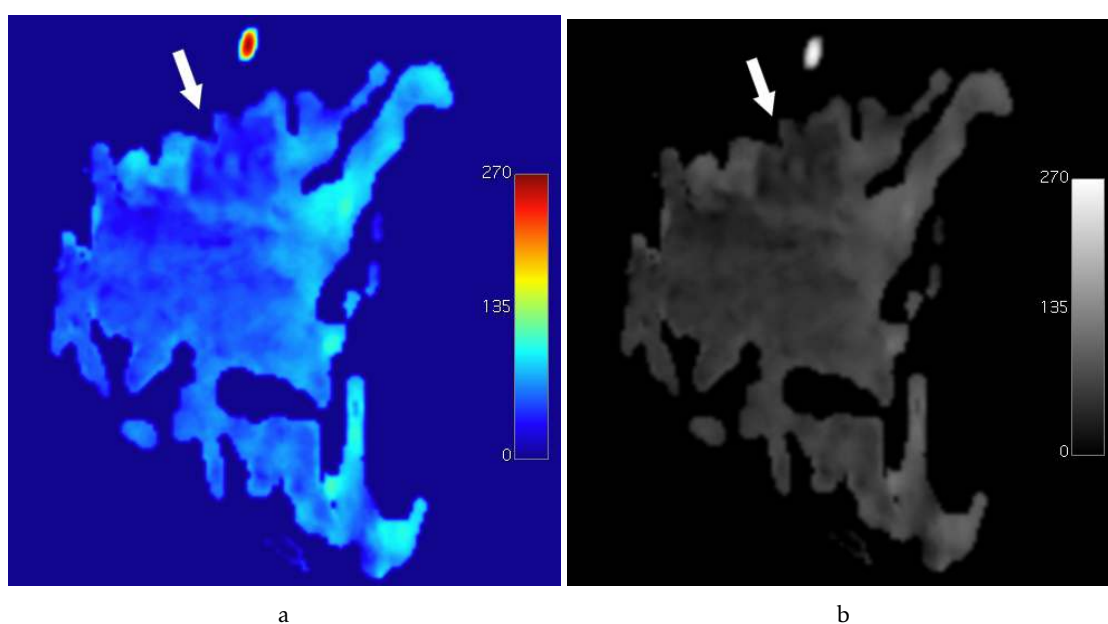


Figure 4.28:  $\sigma$  parametric maps (scaling factor of  $1 \times 10^5$  and in  $\text{mm}^2/\text{s}$ ) with an arrow indicating a malignant lesion (invasive ductal carcinoma) with "jet" CLUT applied (a) and in grayscale (b).

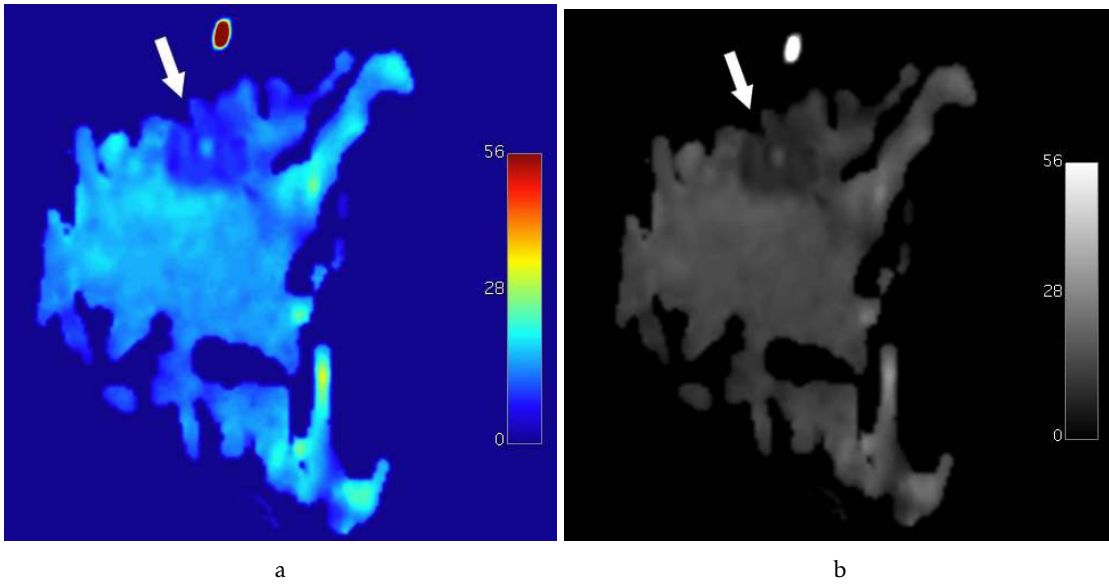


Figure 4.29:  $ADC$  parametric maps (scaling factor of  $1 \times 10^4$  and in  $\text{mm}^2/\text{s}$ ) with an arrow indicating a malignant lesion (invasive ductal carcinoma) with "jet" CLUT applied (a) and in grayscale (b).

#### 4.1.5.2 Benign lesions

In both of the maps,  $\sigma$  (Figure 4.30) and  $ADC$  (Figure 4.31), the benign lesion is clearly seen.

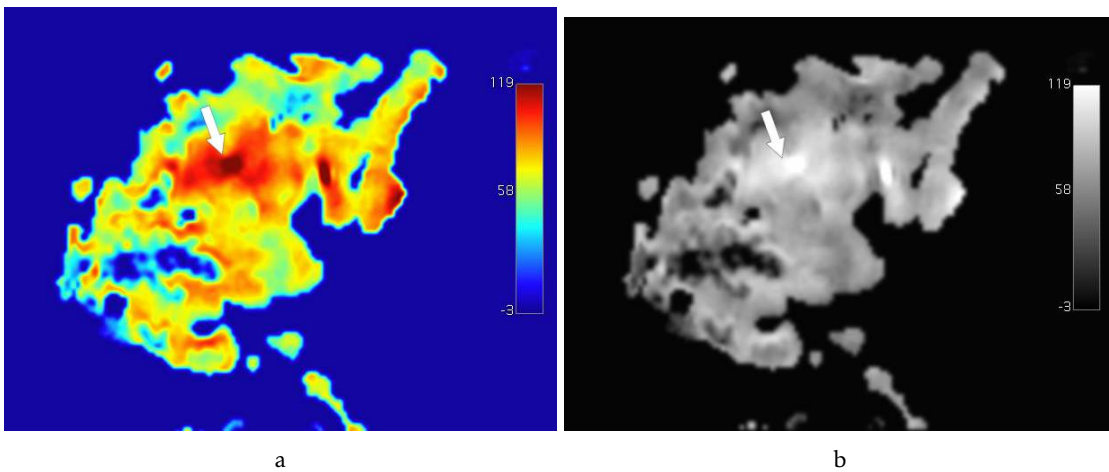


Figure 4.30:  $\sigma$  parametric maps (scaling factor of  $1 \times 10^5$  and in  $\text{mm}^2/\text{s}$ ) with an arrow indicating a benign lesion (fibroadenoma) with "jet" CLUT applied (a) and in grayscale (b).

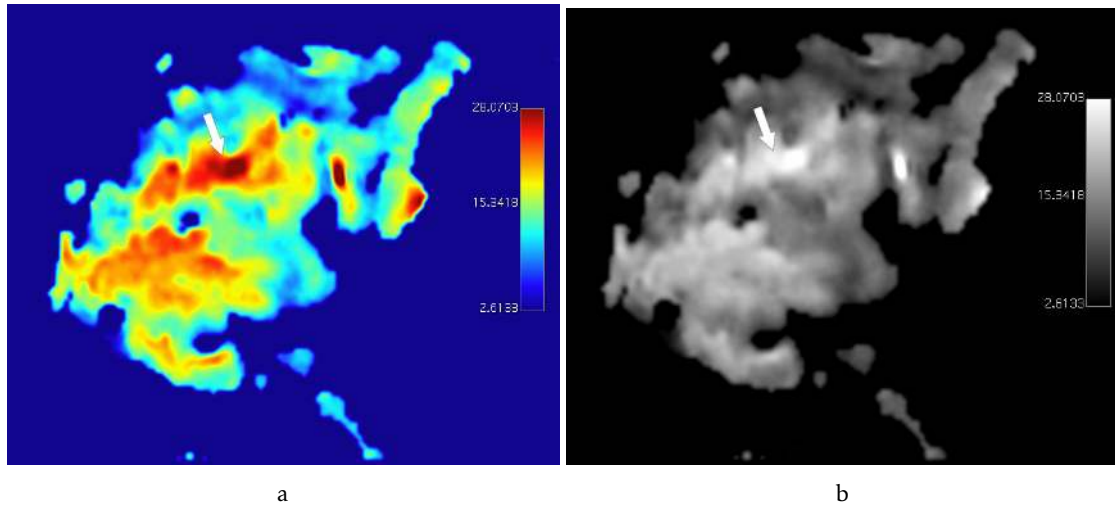


Figure 4.31: ADC parametric maps (scaling factor of  $1 \times 10^4$  and in  $\text{mm}^2/\text{s}$ ) with an arrow indicating a benign lesion (fibroadenoma) with "jet" CLUT applied (a) and in grayscale (b).

#### 4.1.6 Stretched parametric maps

The fifth model is the Stretched model. With it, the user obtains two different maps, the *DDC* map and the  $\alpha$  map. As it was mentioned in subsection 2.5.5, there aren't any studies of this model applied to the breast. However, when both maps of the malignant lesion and benign lesion are compared, the values of the maps for the benign lesions are higher than the ones for the malignant lesion.

The average amount of time that it took to process the Truncated parametric maps was 139 seconds without parallel computing and 110 seconds with parallel computing.

##### 4.1.6.1 Malignant lesions

In the *DDC* map (Figure 4.32) the malignant is clearly seen, unlike the  $\alpha$  map (Figure 4.33). According to the literature, the *DDC* and  $\sigma$  values are lower in malignant lesions in comparison with normal tissue. In spite of it only being tested in prostate, the same is observed in the obtained images, since the tumor is the darkest area of the image. Also, in the *DDC* map it is possible to see tumoral heterogeneity.



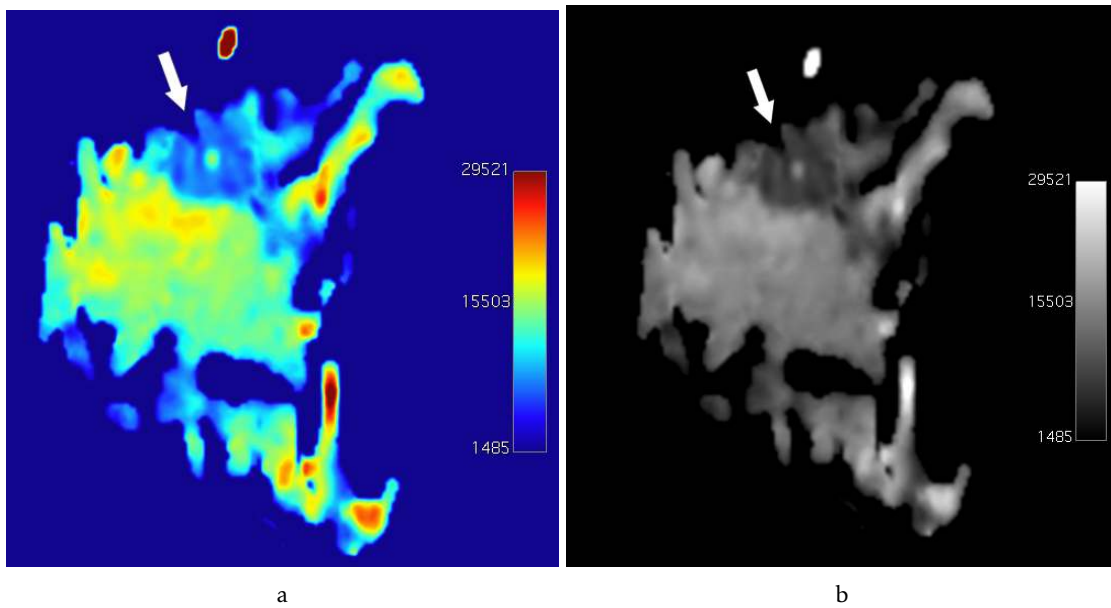


Figure 4.32: *DDC* parametric maps (scaling factor of  $1 \times 10^7$  and in  $\text{mm}^2/\text{s}$ ) with an arrow indicating a malignant lesion (invasive ductal carcinoma) with "jet" CLUT applied (a) and in grayscale (b).

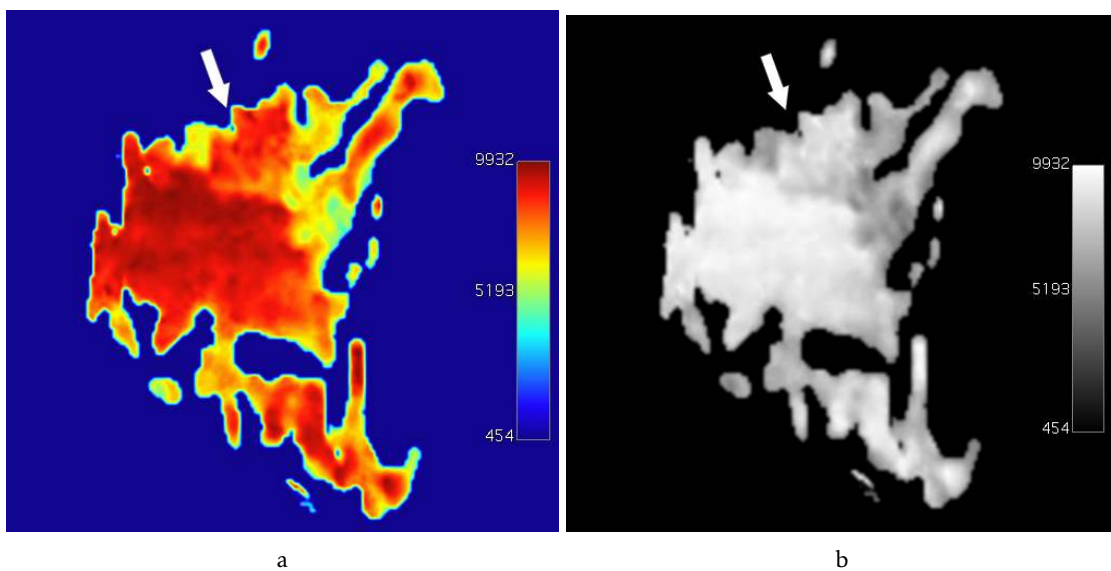


Figure 4.33:  $\alpha$  parametric maps (scaling factor of  $1 \times 10^4$  and with no units since it is dimensionless) with an arrow indicating a malignant lesion (invasive ductal carcinoma) with "jet" CLUT applied (a) and in grayscale (b).

4.1.6.2 Benign lesions

In the *DDC* map (Figure 4.34) the benign lesion is clearly seen, unlike the  $\alpha$  map (Figure 4.35). Since there wasn't found any study that compares benign lesions with normal tissue for this model, it is not possible to compare the obtained results with literature. However, looking at the *DDC* map, it is possible to conclude that the model has the ability to distinguish between benign lesions and normal tissue.

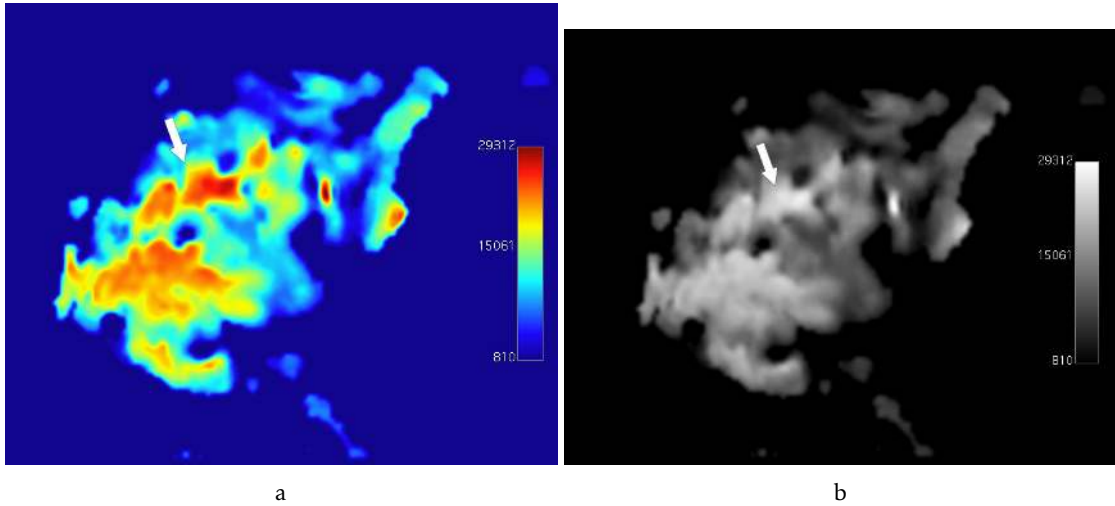


Figure 4.34: *DDC* parametric maps (scaling factor of  $1 \times 10^7$  and in  $\text{mm}^2/\text{s}$ ) with an arrow indicating a benign lesion (fibroadenoma) with "jet" CLUT applied (a) and in grayscale (b).

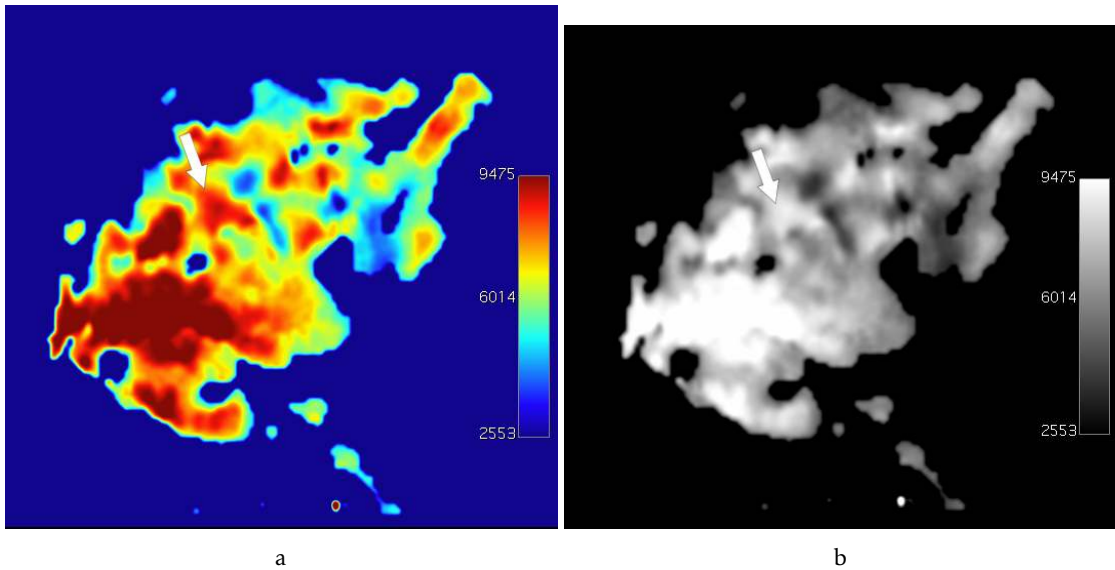


Figure 4.35:  $\alpha$  parametric maps (scaling factor of  $1 \times 10^4$  and with no units since it is dimensionless) with an arrow indicating a benign lesion (fibroadenoma) with "jet" CLUT applied (a) and in grayscale (b).

### 4.1.7 Goodness-of-fit maps

In order to better evaluate the goodness-of-fit between all of the five models, the obtained parametric maps were compared. Since we are only working with eight images for the fitting process, the goodness-of-fit doesn't vary much for each model (between 0.8 and 1.0).

Another conclusion that is reached is that the fitting worked better for the malignant lesions than for the benign lesions as is shown in the following Figures 4.36 and 4.37 since the values of the goodness-of-fit vary from 0.7 to 1. The maps also appear to have lost information since they show black spots in the middle of breast image.

The maps of the IVIM models aren't compared with the other models because they have a smaller amount of images tested since it only works for  $b$  values lower than  $1000 \text{ s/mm}^2$ . The IVIM model also has three free parameters to be determined which can provide a less reliable parameter estimation in spite of having good goodness-of-fit values [16]. The Figure 4.38 shows goodness of fit values lower for the benign lesion in comparison with the malignant lesion.

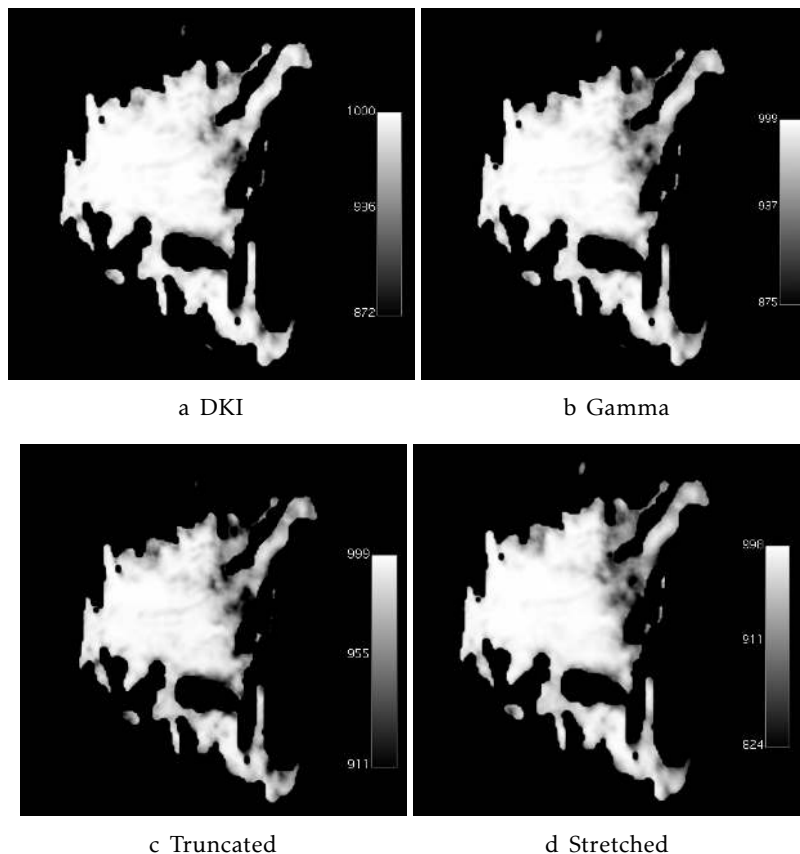


Figure 4.36: Goodness-of-fit maps (scaling factor of  $1 \times 10^3$ ) for DKI, Gamma, Truncated and Stretched models applied to a breast with a malignant lesion (invasive ductal carcinoma).

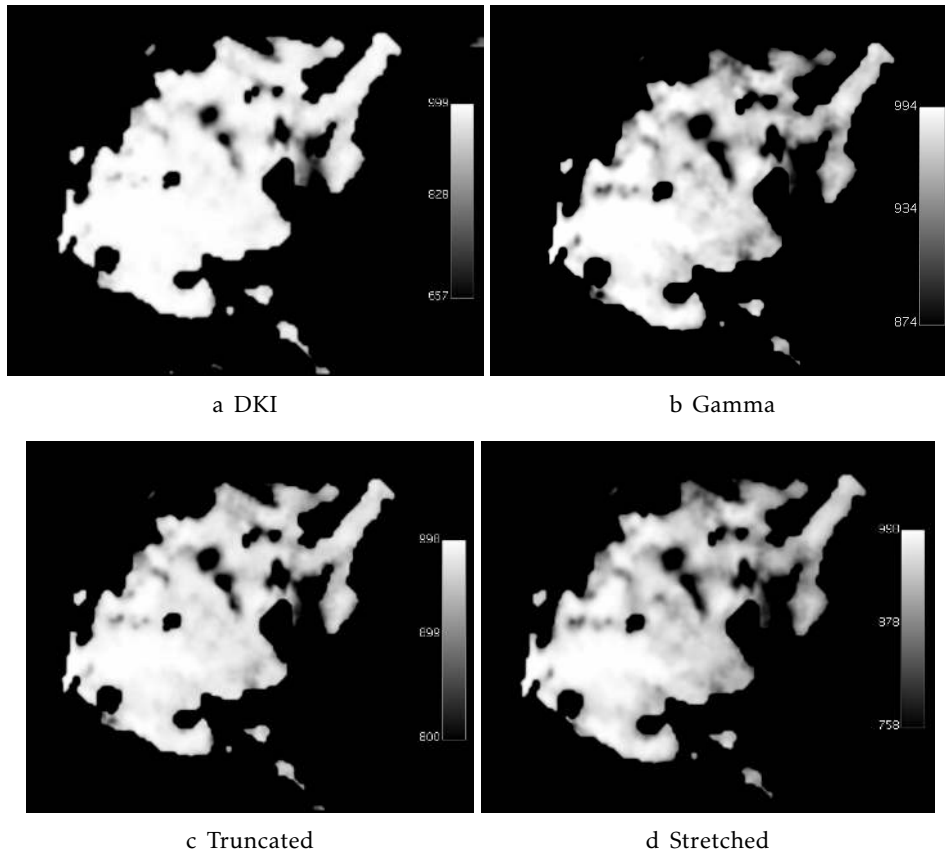


Figure 4.37: Goodness-of-fit map (scaling factor of  $1 \times 10^3$ ) for DKI, Gamma, Truncated and Stretched models applied to a breast with a benign lesion (fibroadenoma).

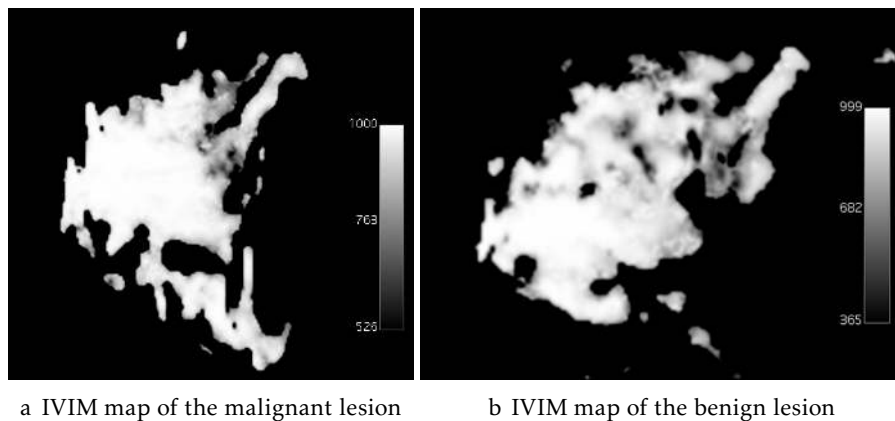


Figure 4.38: Goodness-of-fit maps (scaling factor of  $1 \times 10^3$ ) for the IVIM models applied to a breast with a malignant lesion (invasive ductal carcinoma) and benign lesion (fibroadenoma). The range of greyscale shows that fitting wasn't as good for the malignant lesions as it was for benign lesions.

## 4.2 Parametric values obtained through ROIs

### 4.2.1 Interface to obtain the parametric values

The interface to obtain the parametric maps consists of check boxes to select which models to run, and text fields where the results are shown. Firstly the user will need to draw a ROI in the tumor area like shown in Figure 4.39, which is normally drawn in a high  $b$  value image since it is when the malignant tumors are most visible (in this case it was only to show where it was drawn since the higher  $b$  value image is too dark). When the "OK" button is pressed and the models are chosen, the same warning mentioned in subsection 4.1.1 (Figure 4.2) appears. Also, if the window on OsiriX isn't the one where the user draws the ROI, then the program won't be able to run and it will appear the warning shown on Figure 4.40. While the program is executing, the same window mentioned in subsection 4.1.1 (Figure 4.4) will appear. Also, if the user tries to run the model on the parametric maps, the same warning as mentioned in 4.1.1(Figure 4.3) will appear.

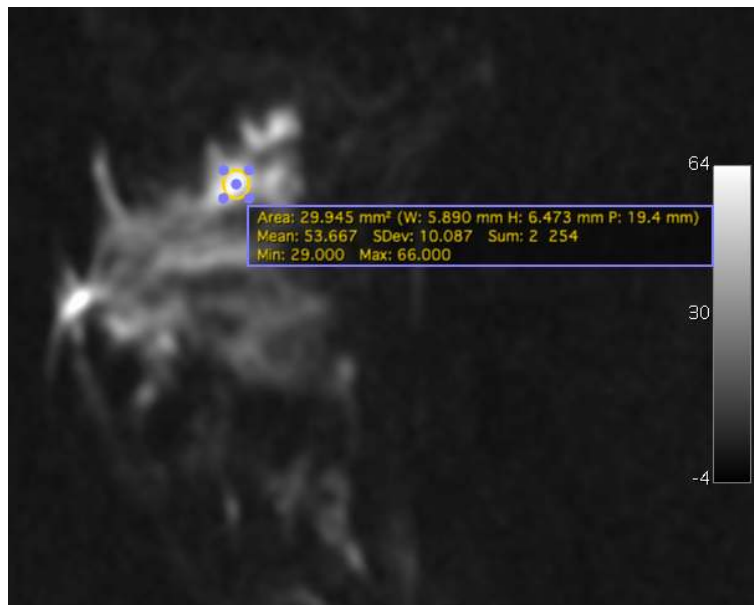


Figure 4.39: DWI image of a breast with a malignant lesion (invasive ductal carcinoma) with  $b$  value of  $1000 \text{ s/mm}^2$  exemplifying a drawn ROI in order to then run the program.

After the program is done running, the window shown on Figure 4.41 appears. The user then gets the opportunity to save the results by pressing the button "Save the results" which will open a window that lets the user choose where to save them (defaulted to be saved in the .txt format). In case the user hasn't run a model yet, the warning in Figure 4.42 will appear. The user gets to delete the drawn ROI and the results that are on the text field boxes with the "Reset" button, however, the window displayed must also be the one where he draws the ROI, or else appears the warning on Figure 4.40. In case the user doesn't press the "Reset" button or draws another ROI, then all of the results will be from the initially drawn ROI.



Figure 4.40: Alert that warns the user that the program can only run if on the displayed window is the image where the user draws the ROI.

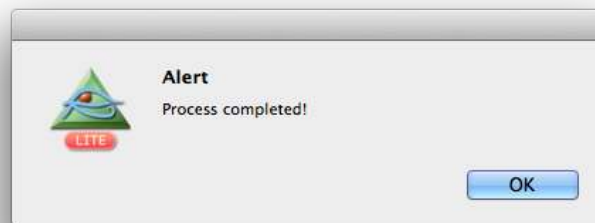


Figure 4.41: Warning that alerts the user that the process to obtain the parametric values is done running.

#### 4.2.2 Obtained parametric values

The outcomes from running a model are the parametric values that are displayed in the text fields (Figure 4.43) and also a plot with the goodness-of-fit. In the case of the malignant tumor tested, all of the parametric values obtained were in agreement with the literature. For the truncated and stretched models it wasn't possible to compare the results with the ones from literature since they don't exist yet. The same happened when the models were applied to a benign tumor, where the results of the parametric values (Figure 4.44) are in agreement with the literature.

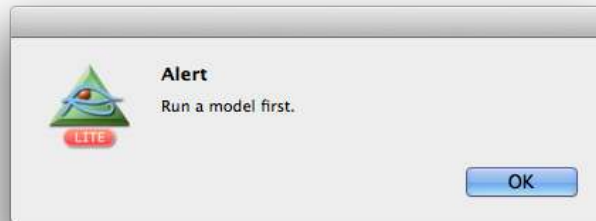


Figure 4.42: Warning that appears when the user is trying to save the results obtained but without running a model first.

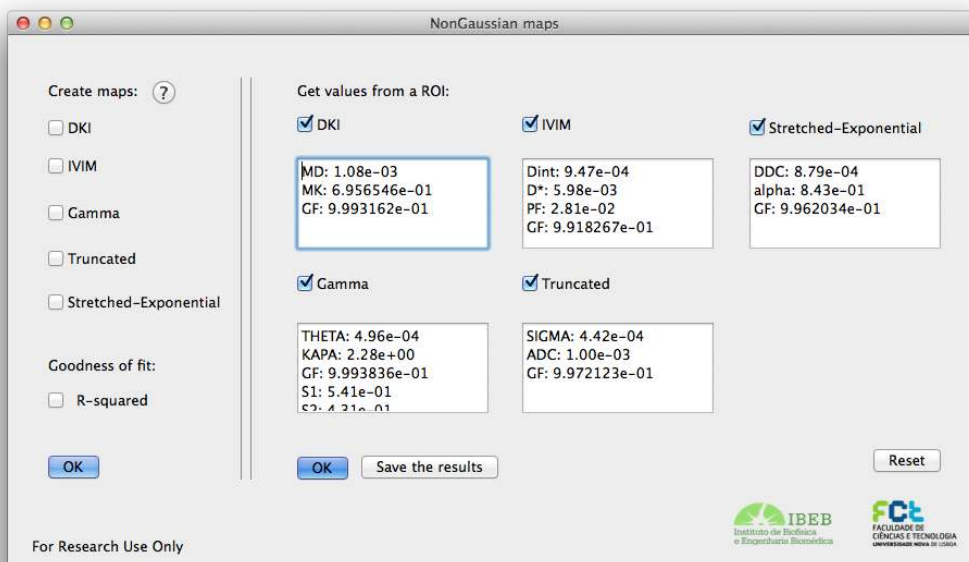


Figure 4.43: Results for the parametric values obtained through ROIS around the malignant tumor (invasive ductal carcinoma) area.

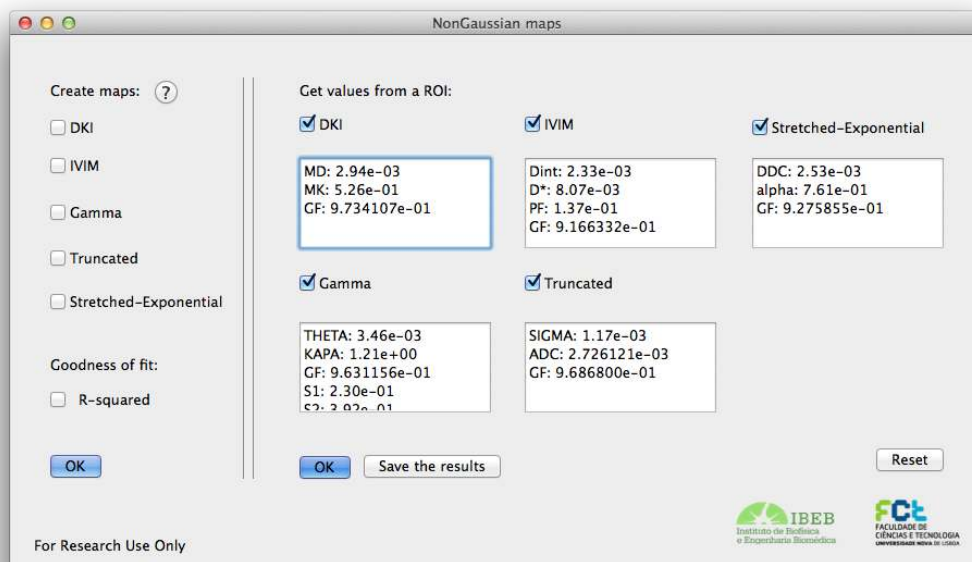


Figure 4.44: Results for the parametric values obtained through ROIS around the benign tumor (fibroadenoma) area.



#### 4.2.2.1 Results from the DKI model of the malignant lesion

The parametric values obtained for DKI in an image with a malignant tumor (invasive ductal carcinoma) were the ones seen on Figure 4.43.  $MD$  has the value  $1.08 \times 10^{-3} \text{mm}^2/\text{s}$  and  $MK$  0.70 (dimensionless metric). Since a malignant tumor typically has  $MD$  values between  $1.02$  and  $2.02 \times 10^{-3} \text{mm}^2/\text{s}$  and  $MK$  values between 0.34 and 0.88, and the results obtained were between those intervals, it is possible to affirm that the model is working correctly.

The user also obtains a plot of the fitting of the  $b$  values versus the median values of the ROI where it is possible to observe the good fitting of the model (Figure 4.45).

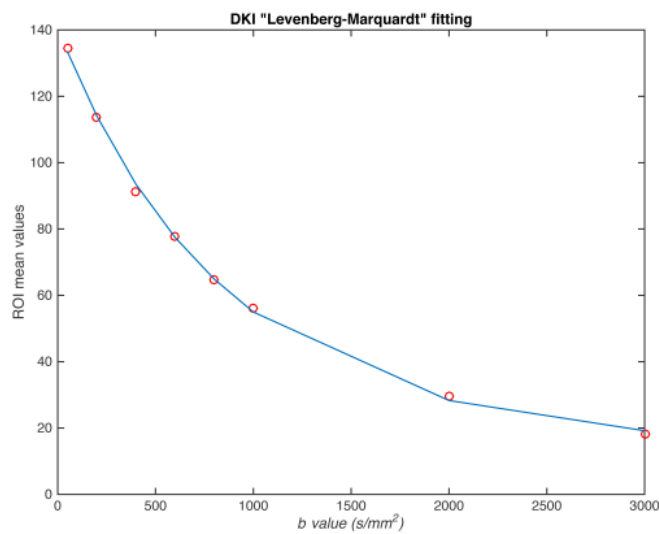


Figure 4.45: Fitting plot for the DKI model of a DWI image of the breast with a malignant lesion (invasive ductal carcinoma) where it is possible to see how well the fitting process was done.

#### 4.2.2.2 Results from the DKI model of the benign lesion

The parametric values obtained for the DKI applied in an image with a benign tumor (fibroadenoma) were the ones seen on Image 4.44.  $MD$  has the value  $2.94 \times 10^{-3} \text{mm}^2/\text{s}$  and  $MK$  0.53 (dimensionless metric). Since a benign tumor is supposed to have  $MD$  values between  $1.75$  and  $2.59 \times 10^{-3} \text{mm}^2/\text{s}$  and  $MK$  values between 0.19 and 0.55. The results for the  $MD$  parameters that were obtained are higher than the ones referenced in literature, which can be expected since the fitting wasn't as good as it was for the malignant lesions.

The user also obtains a plot of the fitting of the  $b$  values versus the median values of the ROI where it is possible to observe the fitting of the model (Figure 4.46). In this case the fitting wasn't as successful as the malignant lesion.

Since the fitting wasn't good in a few points, for example at the  $b$  values  $1000 \text{ s/mm}^2$  and  $2000 \text{ s/mm}^2$  it can justify when the obtained parametric values were slightly higher than expected.

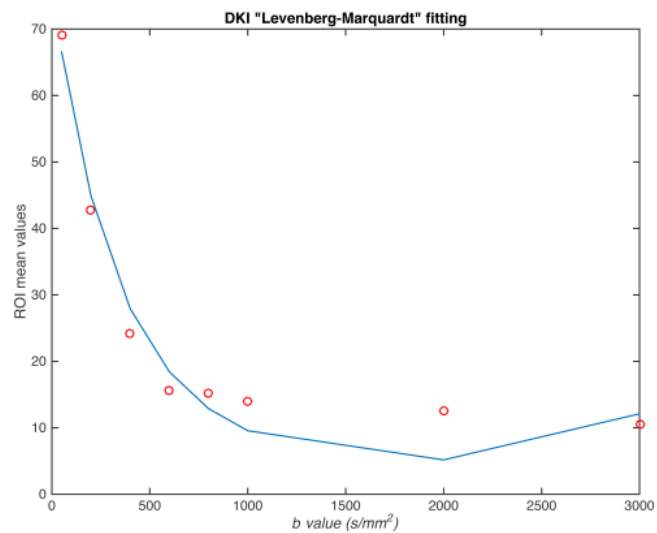


Figure 4.46: Fitting plot for the DKI model of a DWI image of the breast with a benign lesion (fibroadenoma) where is possible to see that the fitting wasn't well performed in the last  $b$  values.

4.2.2.3 Results from the IVIM model of the malignant lesion

The parametric values obtained for the IVIM model applied in an image with a malignant tumor (invasive ductal carcinoma) were the ones seen on Figure 4.43.  $D$  shows the value  $0.95 \times 10^{-3} \text{mm}^2/\text{s}$ ,  $f$  2.81 % and  $D^*$   $5.98 \times 10^{-3} \text{mm}^2/\text{s}$ . According to the literature, a malignant tumor has  $D$  values between  $0.77$  and  $0.98 \times 10^{-3} \text{mm}^2/\text{s}$ ,  $f$  values between 7.68 % and 11.88 % and  $D^*$  values between  $70.33$  and  $113.23 \times 10^{-3} \text{mm}^2/\text{s}$ . In spite of the SI units being on the same order of magnitude, the values obtained were different from the ones expected for malignant lesions with the exception of the  $D$  parameter. A possible reason for this to happen is the  $b$  values of the used images, which started at  $50 \text{ s/mm}^2$ . According to literature, a good amount of  $b$  values would be the same as of free parameters and they would start at  $0 \text{ s/mm}^2$  until  $750 \text{ s/mm}^2$ .

In Figures 4.43 and 4.44  $D_{int}$  corresponds to  $D$ ,  $D_{ast}$  to  $D^*$  and  $PF$  to  $f$ .

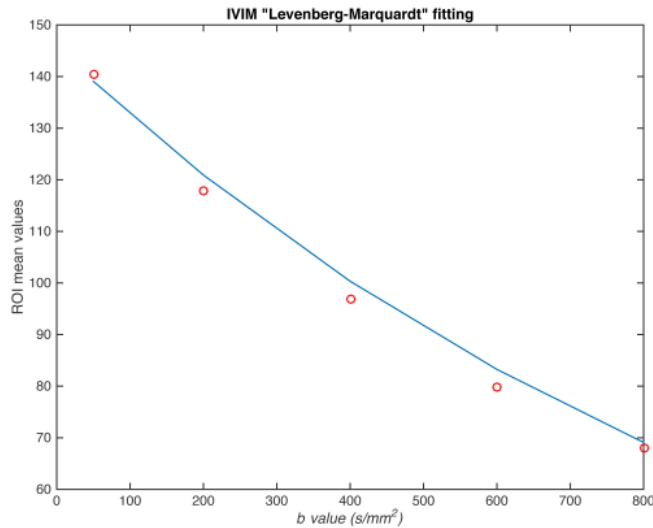


Figure 4.47: Fitting plot for the IVIM model of a DWI image of the breast with a malignant lesion (invasive ductal carcinoma), where is possible to see how the IVIM model doesn't do the fitting as good for higher  $b$  values than it does for lower ones.

4.2.2.4 Results from the IVIM model of the benign lesion

The parametric values obtained for the IVIM model applied in an image with a benign tumor (fibroadenoma) were the ones seen on Figure 4.44.  $D$  has the value  $2.33 \times 10^{-3} \text{mm}^2/\text{s}$ ,  $PF$  13.7 % and  $D^*$   $8.07 \times 10^{-3} \text{mm}^2/\text{s}$ . According to the literature, a benign tumor has  $D$  values between  $1.26$  and  $1.44 \times 10^{-3} \text{mm}^2/\text{s}$ ,  $f$  values between 4.72 % and 10.33 % and  $D^*$  values between  $83.20$  and  $113.19 \times 10^{-3} \text{mm}^2/\text{s}$ . The reason for this discrepancy is also explained in the malignant lesions section 4.2.2.3.

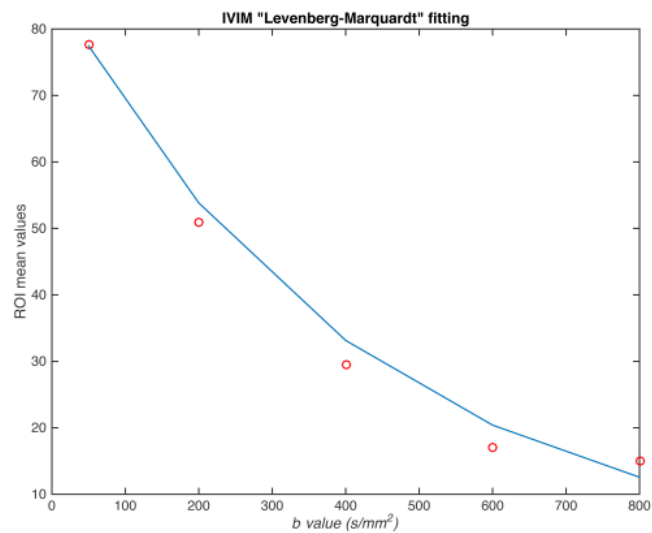


Figure 4.48: Fitting plot for the IVIM model of a DWI image of the breast with a benign lesion (fibroadenoma), where is possible to see that the fitting isn't as good for higher  $b$  values than it does for lower ones.

#### 4.2.2.5 Results from the Gamma model of the malignant lesion

The parametric values obtained for the Gamma model applied in an image with a malignant tumor (invasive ductal carcinoma) were the ones seen on Figure 4.43.  $\theta$  has the value  $0.50 \times 10^{-3} \text{mm}^2/\text{s}$  and  $\kappa$  2.28 (dimensionless metric). Since a malignant tumor is suppose to have  $\theta$  values between  $0.71$  and  $1.75 \times 10^{-3} \text{mm}^2/\text{s}$  and  $\kappa$  values between  $0.47$  and  $1.47$ , it is possible to say that the model is working correctly for the  $\theta$  values, but has a slight deviation for the  $\kappa$  values. However, it was mentioned in 2.5.3 that those two parameters aren't the best to locate the tumor, unlike the S1 parameter.

S1 has the value 0.54, S2 0.43 and S3 0.03. According to what was mentioned in 2.5.3 a malignant tumor would have S1 values higher than 0.30 and S3 values lower than 0.50, which is the case. However, it is important to notice that those values are from tests performed to prostate and not breast.

The plot with the fitting of the  $b$  values versus the median values of the ROI shows a good fitting of the values (Figure 4.49).

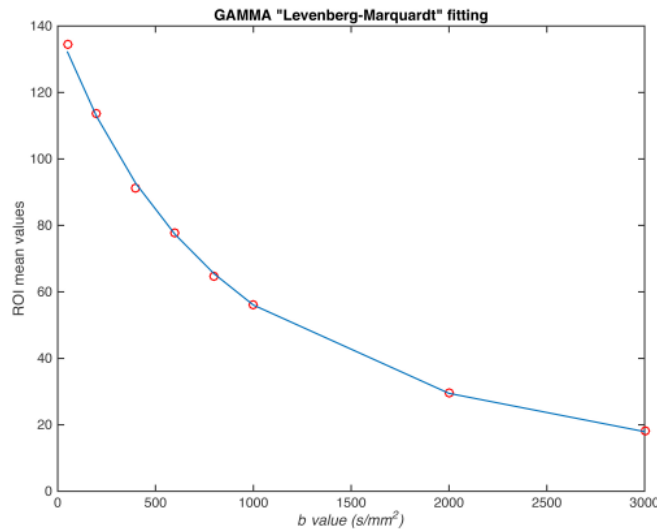


Figure 4.49: Fitting plot for the Gamma model of a DWI image of the breast with a malignant lesion (invasive ductal carcinoma), where is possible to see how well the fitting process was done.

#### 4.2.2.6 Results from the Gamma model of the benign lesion

The parametric values obtained for the Gamma model applied in an image with a benign tumor (fibroadenoma) were the ones seen on Figure 4.44.  $\theta$  has the value  $3.46 \times 10^{-3} \text{mm}^2/\text{s}$  and  $\kappa$  1.21 (dimensionless metric). Since a benign tumor is suppose to have  $\theta$  values between  $2.39$  and  $6.19 \times 10^{-3} \text{mm}^2/\text{s}$  and  $\kappa$  values between  $0.22$  and  $1.08$ , it is possible to say that the model is working correctly for the  $\theta$  values, but has a slight deviation for the  $\kappa$  values. According to literature, the benign lesions have higher  $\theta$  values and lower  $\kappa$  values in comparison with malignant lesions which is also seen in the obtained results.

However, it was mentioned in 2.5.3 that those two parameters aren't the best to locate the tumor, unlike the  $S1$  parameter.

$S1$  has the value 0.23,  $S2$  0.39 and  $S3$  0.38. There is a difference between the  $S1$  values and the  $S2$  and  $S3$  values, which can mean that the tumor is benign. The tests that were performed with these parameters were only applied in prostate and comparing between malignant and peripheric tissue, which means that it doesn't provide information to compare with the obtained results.

The plot with the fitting of the  $b$  values versus the median values of the ROI shows a fitting of the values (Figure 4.50). The incorrect fitting in some  $b$  values can explain why the results of  $\theta$  and  $\kappa$  differ from the ones expected.

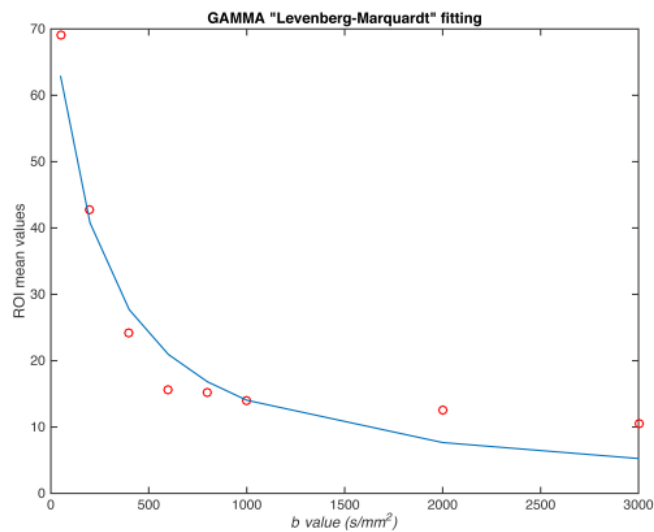


Figure 4.50: Fitting plot for the Gamma model of a DWI image of the breast with a benign lesion (fibroadenoma), where is possible to see that some points don't have a good fitting.

#### 4.2.2.7 Results from the Truncated model of the malignant lesion

The parametric values obtained for the Truncated model applied in an image with a malignant tumor (invasive ductal carcinoma) were the ones seen on Figure 4.43.  $\sigma$  has the value  $0.44 \times 10^{-3} \text{mm}^2/\text{s}$  and  $ADC$   $1.00 \times 10^{-3} \text{mm}^2/\text{s}$ . The fitting plot of the  $b$  values versus the median values of the ROI shows how well the fitting process was performed (Figure 4.51).

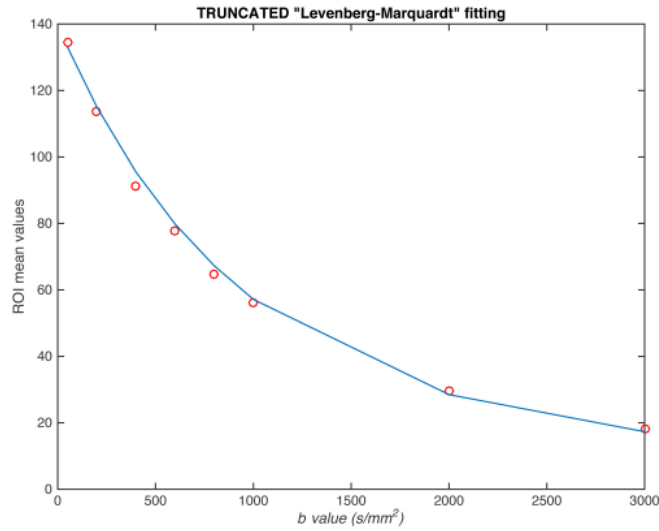


Figure 4.51: Fitting plot for the Truncated model of a DWI image of the breast with a malignant lesion (invasive ductal carcinoma), where it is possible to see how well the fitting process was performed.

#### 4.2.2.8 Results from the Truncated model of the benign lesion

The parametric values obtained for the Truncated model applied in an image with a benign tumor (fibroadenoma) were the ones seen on Figure 4.44.  $\sigma$  has the value  $1.17 \times 10^{-3} \text{mm}^2/\text{s}$  and  $ADC$   $2.73 \times 10^{-3} \text{mm}^2/\text{s}$ . The fitting plot of the  $b$  values versus the median values of the ROI shows how for higher  $b$  values the fitting isn't as good as for lower  $b$  values (Figure 4.52).

When the benign and malignant values for this model are compared it is possible to observe a difference between the values of  $\sigma$  and  $ADC$ , the  $\sigma$  and  $ADC$  values are higher in the benign lesion than in the malignant lesion, which means that it was able to distinguish between the two lesions.

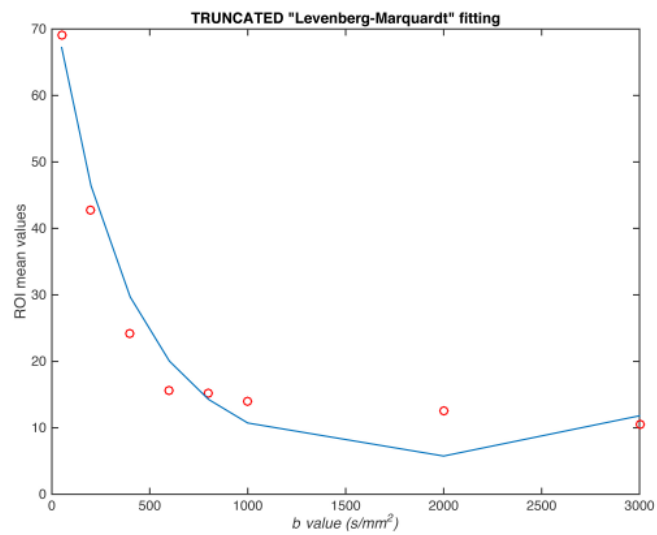


Figure 4.52: Fitting plot for the Truncated model of a DWI image of the breast with a benign lesion (fibroadenoma), where is possible to see that some points don't have a good fitting.



#### 4.2.2.9 Results from the Stretched model of the malignant lesion

The parametric values obtained for the Stretched model applied in an image with a malignant tumor (invasive ductal carcinoma) were the ones seen on Figure 4.43.  $DDC$  has the value  $0.88 \times 10^{-3} \text{mm}^2/\text{s}$  and  $\alpha$  0.84 (dimensionless metric). The fitting plot of the  $b$  values versus the median values of the ROI shows how well the fitting process was performed (Figure 4.53).

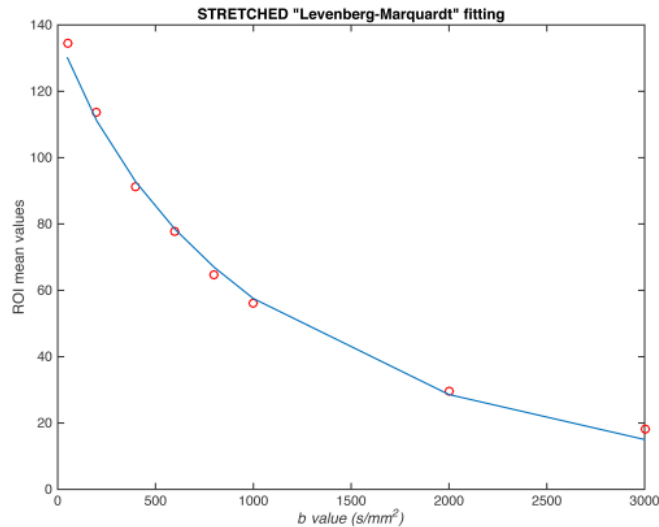


Figure 4.53: Fitting plot for the Stretched model of a DWI image of the breast with a malignant lesion (invasive ductal carcinoma), where is possible to see that some points don't have a good fitting.

#### 4.2.2.10 Results from the Stretched model of the benign lesion

The parametric values obtained for the Stretched model applied in an image with a benign tumor (fibroadenoma) were the ones seen on Figure 4.43.  $DDC$  has the value  $2.53 \times 10^{-3} \text{mm}^2/\text{s}$  and  $\alpha$  0.76 (dimensionless metric). The values for the The fitting plot of the  $b$  values versus the median values of the ROI shows how for higher  $b$  values the fitting isn't as good as for lower  $b$  values (Figure 4.54).

When the benign and malignant values for this model are compared it is possible to observe a difference between the values of  $DDC$ , which can mean that it can detect between malignant and benign lesions. However, the same doesn't happen with the  $\alpha$  values that are very similar in both lesions.

#### 4.2.2.11 Results of the goodness-of-fit for all of the models

Since the values of goodness-of-fit obtained are always between 0.9 and 1.0, the better way to evaluate them is to compare them with each model. The models that are compared

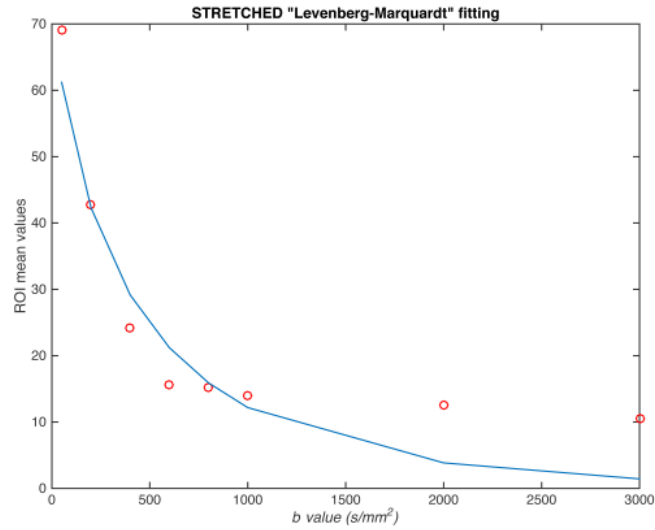


Figure 4.54: Fitting plot for the Stretched model of a DWI image of the breast with a benign lesion (fibroadenoma), where is possible to see that some points don't have a good fitting.

are the ones that were tested with the same amount of  $b$  values like it was explained in 4.1.7.

For the malignant lesions, the goodness-of-fit was 0.9993 for the DKI model, 0.9938 for the Gamma model, 0.9972 for the Truncated model and 0.9962 for the Stretched model.

For the benign lesions, the goodness-of-fit was 0.9734 for the DKI model, 0.9631 for the Gamma model, 0.9686 for the Truncated model and 0.9276 for the Stretched model.

In case of the IVIM model, the goodness-of-fit value for the malignant lesions was 0.9918 and for the benign lesions, 0.9166.

When both lesions are compared, it is concluded that the goodness of fit for the malignant lesion had higher values which goes in agreement with the previous results, the curve fitting performed better in the malignant lesions.

### 4.3 Number of $b$ values and noise tests

#### 4.3.1 $b$ values test

As it was explained in 3.3.1, in order to better inform the user on which images he should use the plug-in, several different combinations of images with different  $b$  values were tested. The combination that is going to be mentioned in this section is the one which the  $b$  values were removed in the order:  $600 \text{ s/mm}^2$ ,  $2000 \text{ s/mm}^2$ ,  $200 \text{ s/mm}^2$ ,  $800 \text{ s/mm}^2$  and  $1000 \text{ s/mm}^2$ .

The conclusions that can be taken after evaluating how all of the models reacted to a small number of  $b$  values is that the models work best with a bigger amount, except for the IVIM, and the minimum of recommended  $b$  values for a map should be of 3  $b$  values.

##### 4.3.1.1 DKI

The images that were obtained with the mentioned combination of  $b$  values for the DKI model are shown in Figures 4.55 ( $MD$  map) and 4.56 ( $MK$  map). In both maps, the tumor was visible until the image with the  $b$  value  $800 \text{ s/mm}^2$  is removed, then the outlines of the lesion become less detectable.

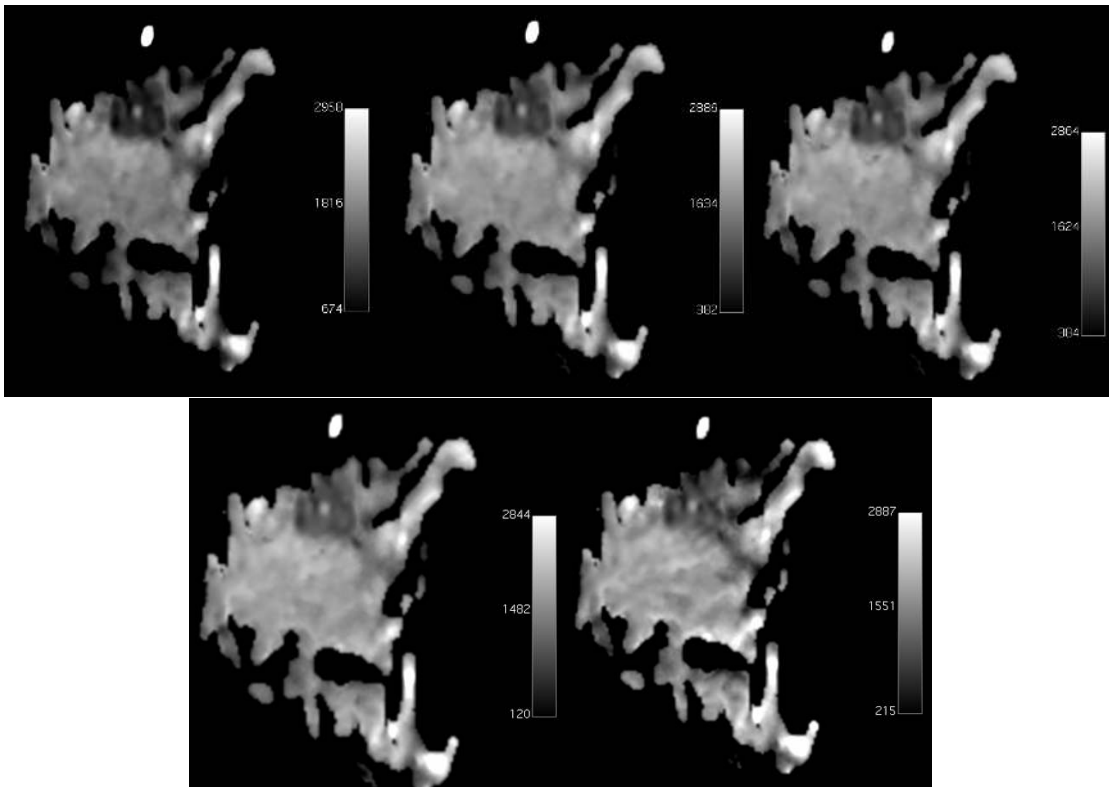


Figure 4.55:  $MD$  maps (scaling factor of  $1 \times 10^6$  and in  $\text{mm}^2/\text{s}$ ) of a breast with a malignant lesion (invasive ductal carcinoma) which show the quality decrease when are applied with images with less  $b$  values. The  $b$  values were removed in the order:  $600 \text{ s/mm}^2$ ,  $2000 \text{ s/mm}^2$ ,  $200 \text{ s/mm}^2$ ,  $800 \text{ s/mm}^2$  and  $1000 \text{ s/mm}^2$ , respectively.

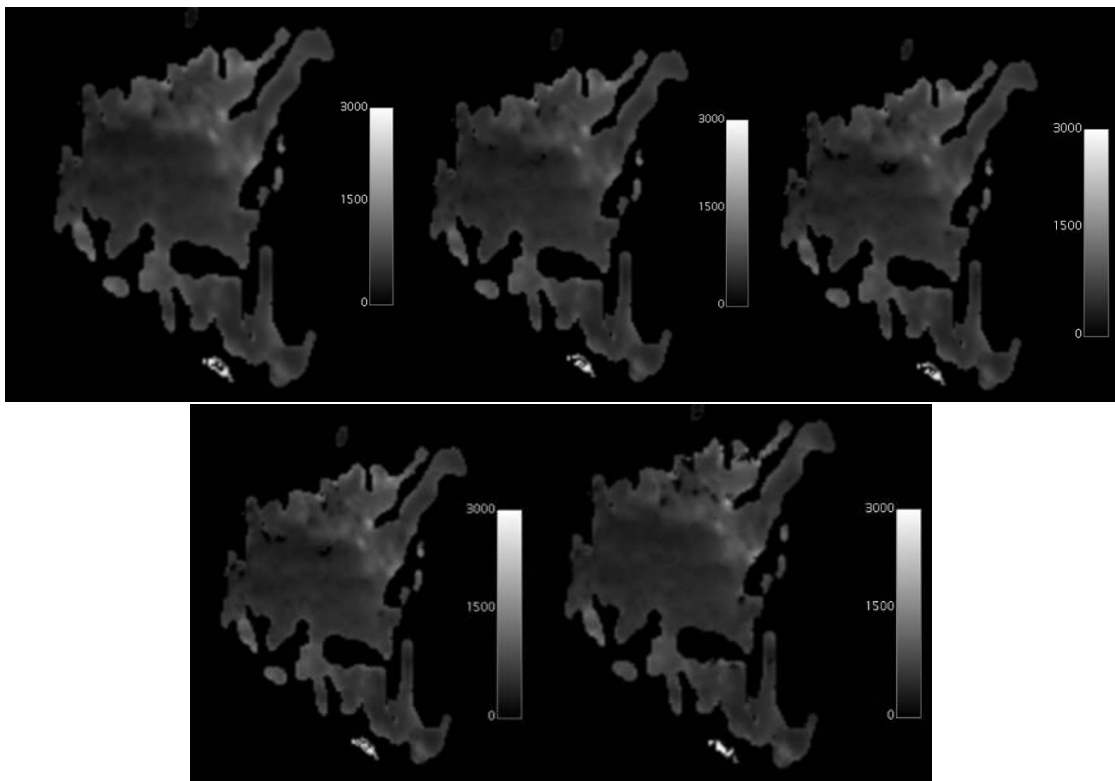


Figure 4.56: *MK* maps (scaling factor of  $1 \times 10^3$  with no units since it is dimensionless) of a breast with a malignant lesion (invasive ductal carcinoma) which show the quality decrease when are applied with images with less  $b$  values. The  $b$  values were removed in the order:  $600 \text{ s/mm}^2$ ,  $2000 \text{ s/mm}^2$ ,  $200 \text{ s/mm}^2$ ,  $800 \text{ s/mm}^2$  and  $1000 \text{ s/mm}^2$ , respectively.

## 4.3.1.2 IVIM

The images that were obtained with the mentioned combination of  $b$  values for the IVIM model are shown in Figures 4.57 ( $D^*$  map), 4.58 ( $D$  map) and 4.59 ( $f$  map). In the  $D$  map, the tumor is always visible. However, both the  $D^*$  and  $f$  maps had bad quality and the tumor is hardly seen.

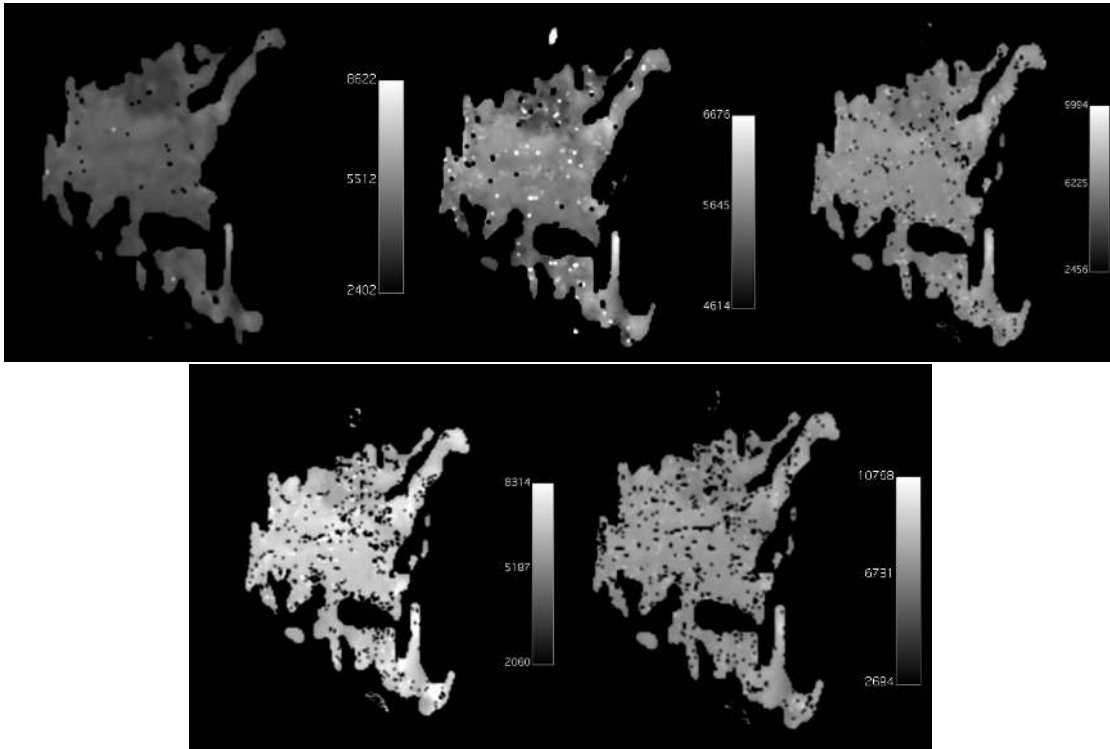


Figure 4.57:  $D^*$  maps (scaling factor of  $1 \times 10^6$  and in  $\text{mm}^2/\text{s}$ ) of a breast with a malignant lesion (invasive ductal carcinoma) which show the quality increase when are applied with images with less  $b$  values. The  $b$  values that was removed was  $50 \text{ s}/\text{mm}^2$ . Then it was  $200$ ,  $400$ ,  $600$  and  $800 \text{ s}/\text{mm}^2$ , respectively. In all of the tests, the amount of  $b$  values for each image was 4.

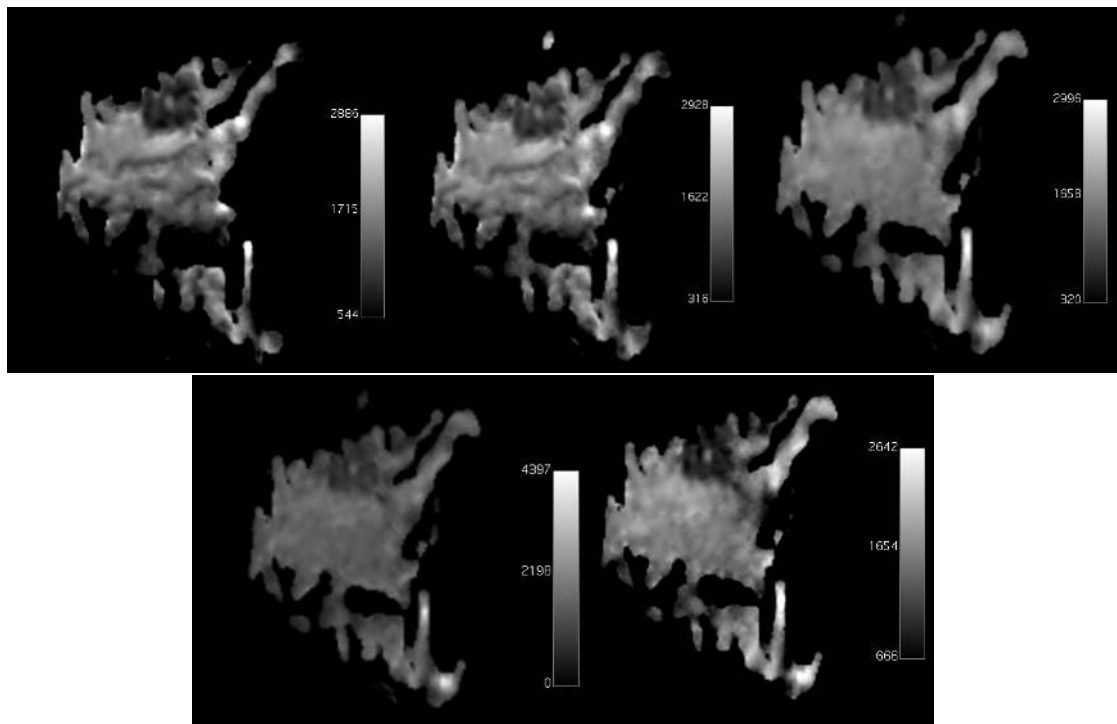


Figure 4.58:  $D$  maps (scaling factor of  $1 \times 10^6$  and in  $\text{mm}^2/\text{s}$ ) of a breast with a malignant lesion (invasive ductal carcinoma) which show the quality decrease when are applied with images with less  $b$  values. The  $b$  values that was removed was  $50 \text{ s}/\text{mm}^2$ . Then it was  $200$ ,  $400$ ,  $600$  and  $800 \text{ s}/\text{mm}^2$ , respectively. In all of the tests, the amount of  $b$  values for each image was 4.

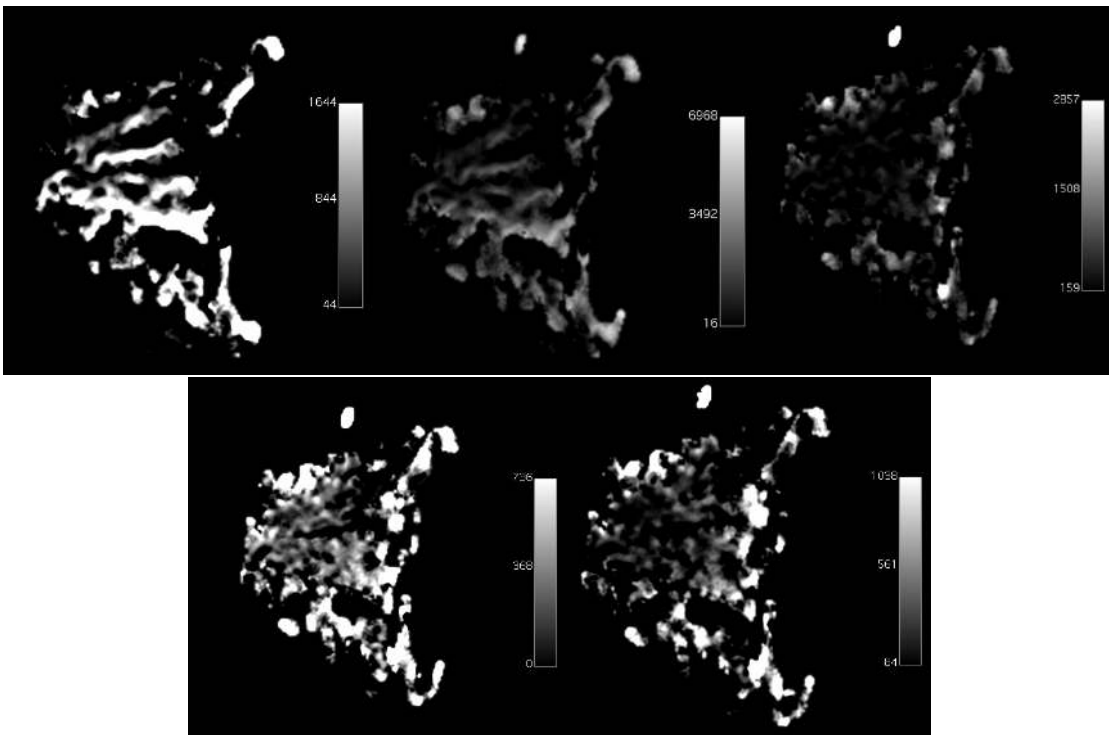


Figure 4.59:  $f$  maps (scaling factor of  $1 \times 10^4$  and in %) of a breast with a malignant lesion (invasive ductal carcinoma) which show the quality increase when are applied with images with less  $b$  values. The  $b$  values that was removed was  $50 \text{ s/mm}^2$ . Then it was  $200$ ,  $400$ ,  $600$  and  $800 \text{ s/mm}^2$ , respectively. In all of the tests, the amount of  $b$  values for each image was 4.

### 4.3.1.3 Gamma distribution

The images that were obtained with the mentioned combination of  $b$  values for the Gamma model are shown in Figures 4.60 ( $\theta$  map), 4.61 ( $\kappa$  map), 4.62 (S1 map), 4.63 (S2 map) and 4.64 (S3 map). In all of the maps, the tumor is visible until the image with the  $b$  value  $800 \text{ s/mm}^2$  is removed, then the outlines of the lesion become less detectable.

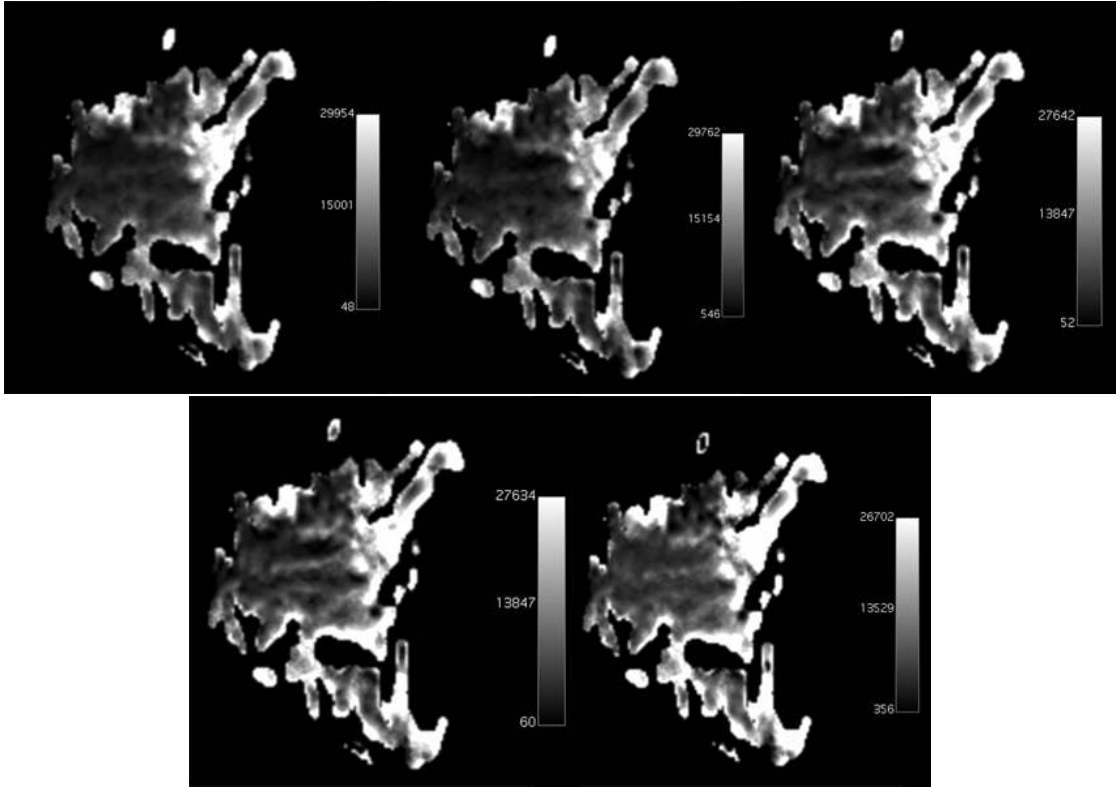


Figure 4.60:  $\theta$  maps (scaling factor of  $1 \times 10^4$  and in  $\text{mm}^2/\text{s}$ ) of a breast with a malignant lesion (invasive ductal carcinoma) which show the quality decrease when are applied with images with less  $b$  values. The  $b$  values were removed in the order:  $600 \text{ s/mm}^2$ ,  $2000 \text{ s/mm}^2$ ,  $200 \text{ s/mm}^2$ ,  $800 \text{ s/mm}^2$  and  $1000 \text{ s/mm}^2$ , respectively.



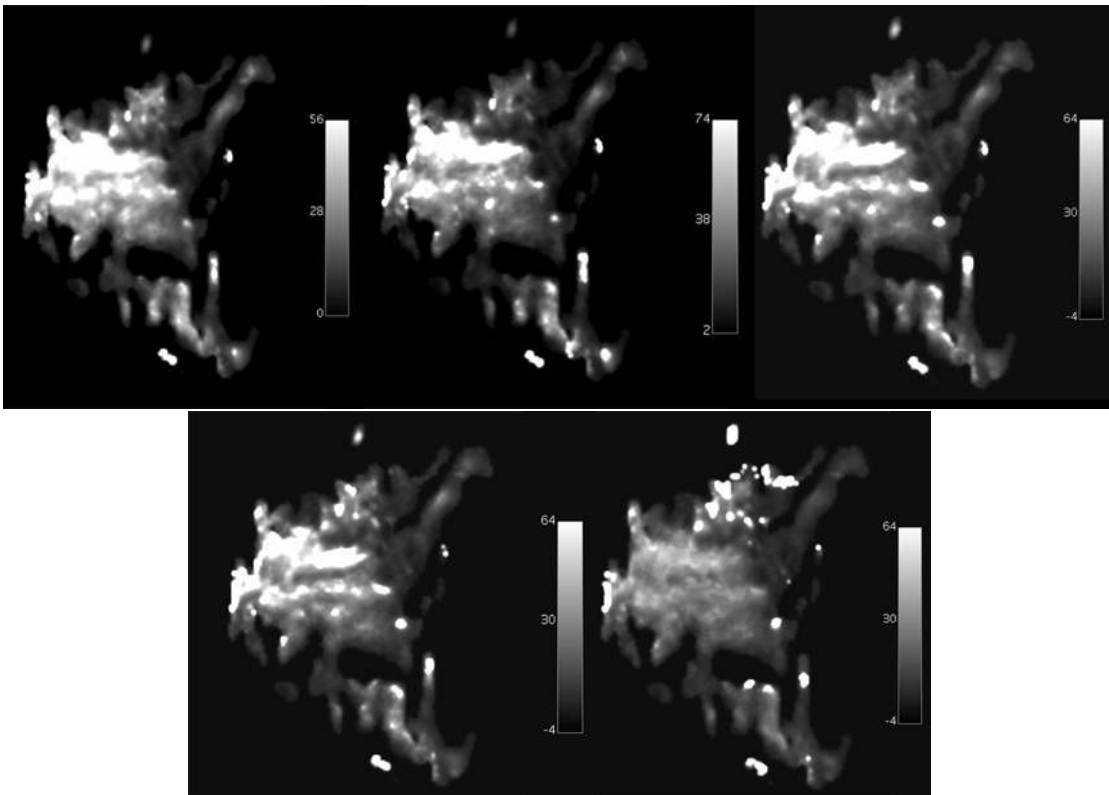


Figure 4.61:  $\kappa$  maps (scaling factor of 10 and with no units since it is dimensionless) of a breast with a malignant lesion (invasive ductal carcinoma) which show the quality decrease when are applied with images with less  $b$  values. The  $b$  values were removed in the order:  $600 \text{ s/mm}^2$ ,  $2000 \text{ s/mm}^2$ ,  $200 \text{ s/mm}^2$ ,  $800 \text{ s/mm}^2$  and  $1000 \text{ s/mm}^2$ , respectively.

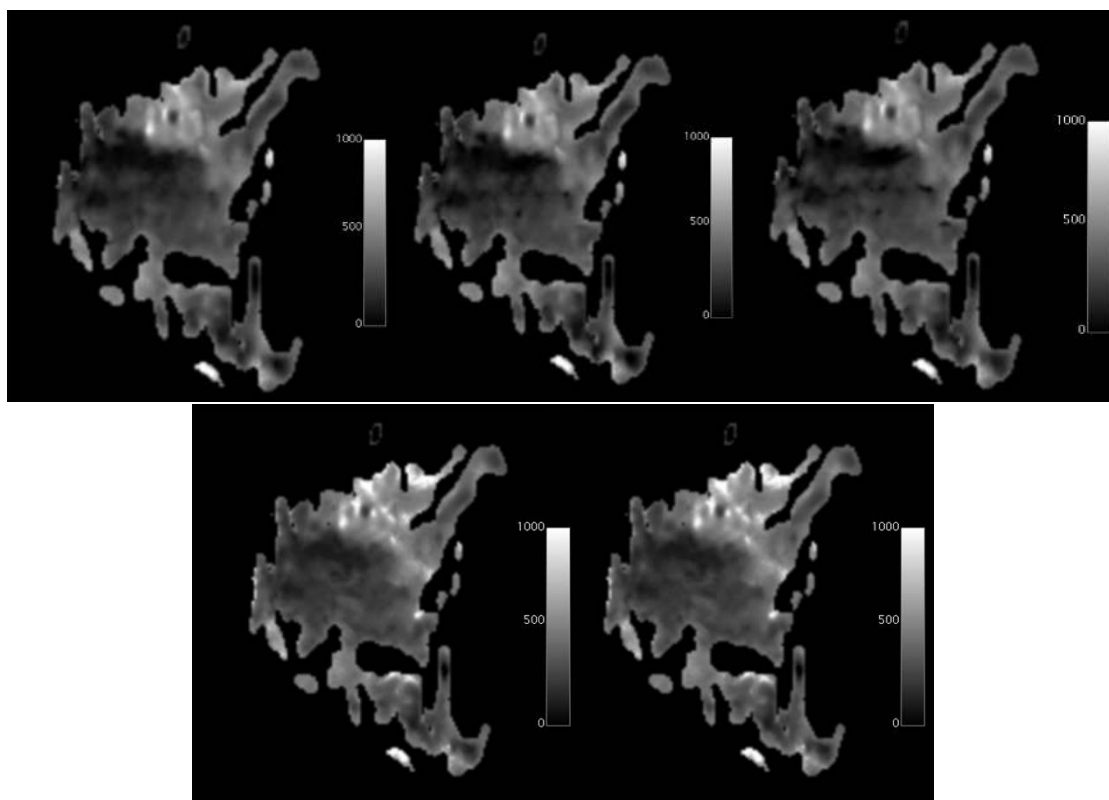


Figure 4.62:  $S_1$  maps (scaling factor of  $1 \times 10^3$  and in %) of a breast with a malignant lesion (invasive ductal carcinoma) which show the quality decrease when are applied with images with less  $b$  values. The  $b$  values were removed in the order:  $600 \text{ s/mm}^2$ ,  $2000 \text{ s/mm}^2$ ,  $200 \text{ s/mm}^2$ ,  $800 \text{ s/mm}^2$  and  $1000 \text{ s/mm}^2$ , respectively.

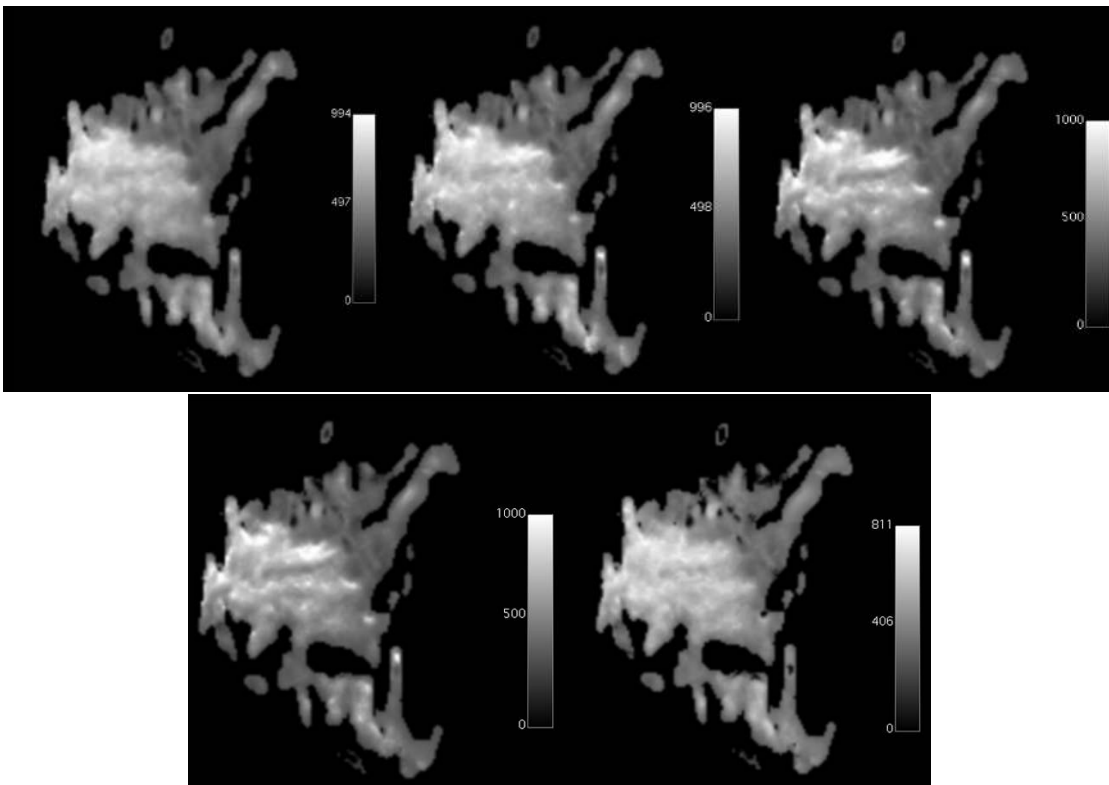


Figure 4.63:  $S_2$  maps (scaling factor of  $1 \times 10^3$  and in %) of a breast with a malignant lesion (invasive ductal carcinoma) which show the quality decrease when are applied with images with less  $b$  values. The  $b$  values were removed in the order:  $600 \text{ s/mm}^2$ ,  $2000 \text{ s/mm}^2$ ,  $200 \text{ s/mm}^2$ ,  $800 \text{ s/mm}^2$  and  $1000 \text{ s/mm}^2$ , respectively.

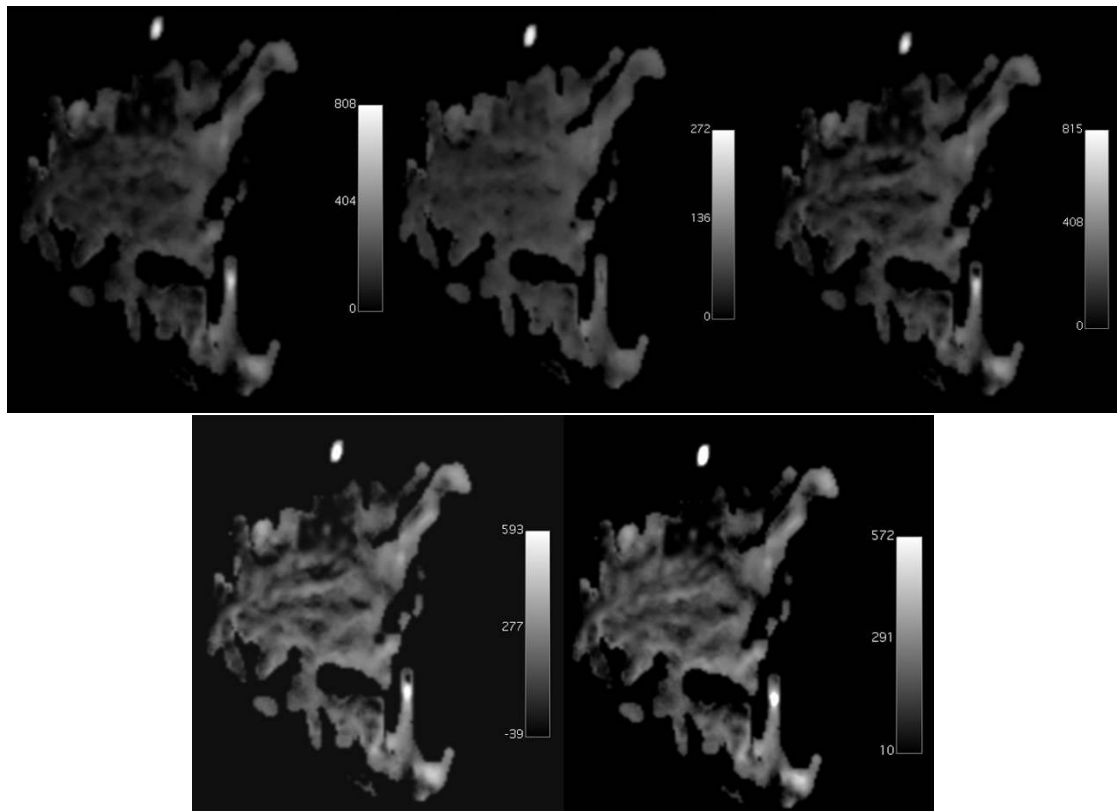


Figure 4.64:  $S_3$  maps (scaling factor of  $1 \times 10^3$  and in %) of a breast with a malignant lesion (invasive ductal carcinoma) which show the quality decrease when are applied with images with less  $b$  values. The  $b$  values were removed in the order:  $600 \text{ s/mm}^2$ ,  $2000 \text{ s/mm}^2$ ,  $200 \text{ s/mm}^2$ ,  $800 \text{ s/mm}^2$  and  $1000 \text{ s/mm}^2$ , respectively.

#### 4.3.1.4 Truncated Gaussian distribution

The images that were obtained with the mentioned combination of  $b$  values for the Truncated model are shown in Figures 4.65 ( $\sigma$  map) and 4.66 ( $ADC$  map). In the map, the tumor is visible until the image with the  $b$  value  $800 \text{ s/mm}^2$  is removed, then the outlines of the lesion become less detectable. However, the  $\sigma$  map didn't work as well after the  $800 \text{ s/mm}^2$  is removed. The tumor is still visible, but barely and the last image lost much more information than the  $ADC$  map.

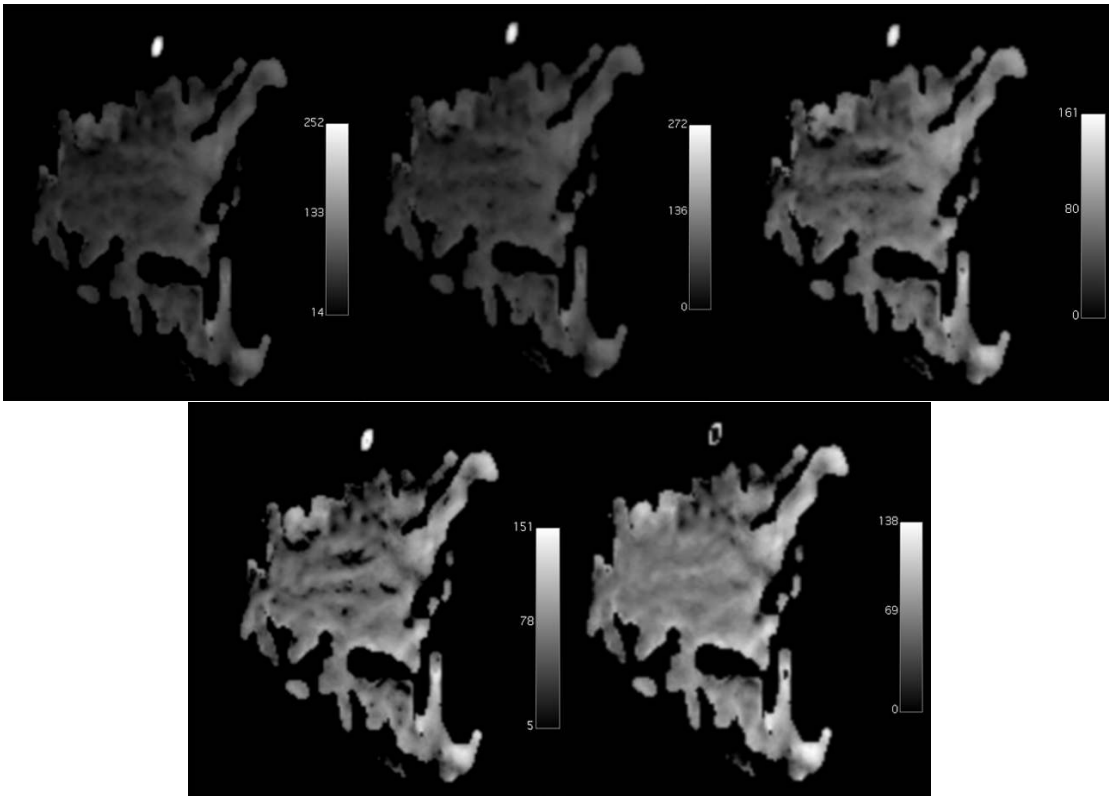


Figure 4.65:  $\sigma$  maps (scaling factor of  $1 \times 10^5$  and in  $\text{mm}^2/\text{s}$ ) of a breast with a malignant lesion (invasive ductal carcinoma) which show the quality decrease when are applied with images with less  $b$  values. The  $b$  values were removed in the order:  $600 \text{ s/mm}^2$ ,  $2000 \text{ s/mm}^2$ ,  $200 \text{ s/mm}^2$ ,  $800 \text{ s/mm}^2$  and  $1000 \text{ s/mm}^2$ , respectively.

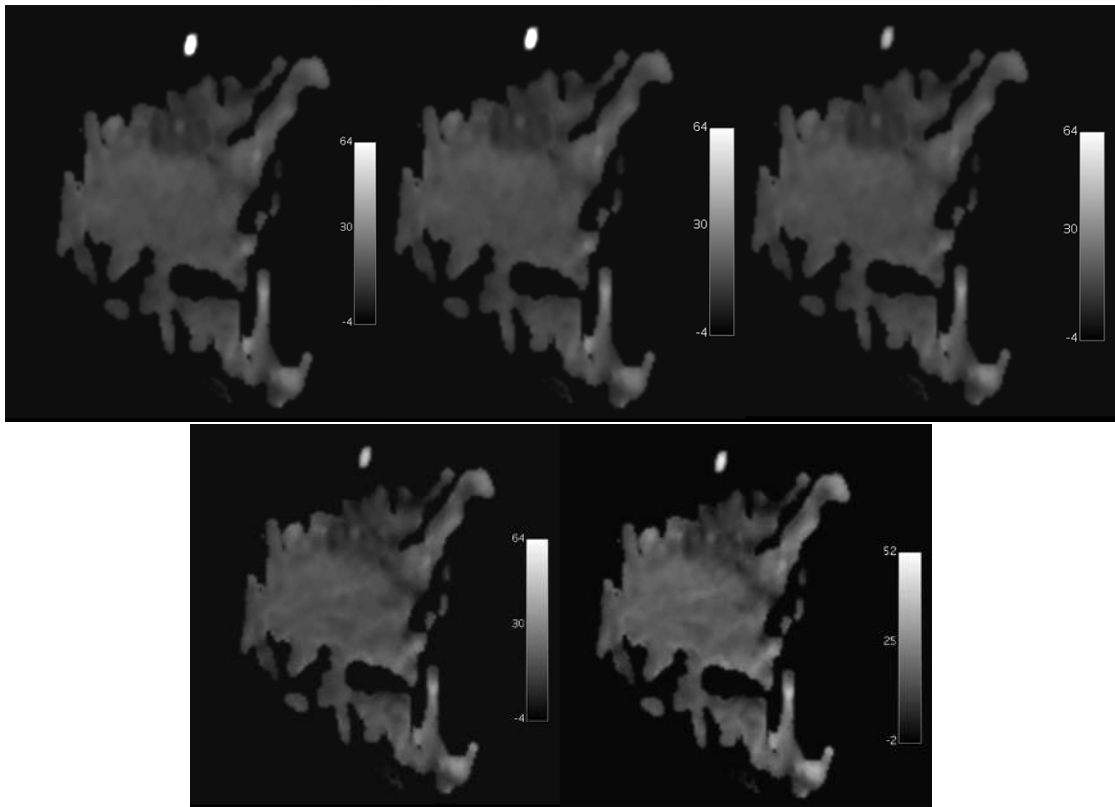


Figure 4.66: ADC maps (scaling factor of  $1 \times 10^4$  and in  $\text{mm}^2/\text{s}$ ) of a breast with a malignant lesion (invasive ductal carcinoma) which show the quality decrease when are applied with images with less  $b$  values. The  $b$  values were removed in the order:  $600 \text{ s}/\text{mm}^2$ ,  $2000 \text{ s}/\text{mm}^2$ ,  $200 \text{ s}/\text{mm}^2$ ,  $800 \text{ s}/\text{mm}^2$  and  $1000 \text{ s}/\text{mm}^2$ , respectively.

#### 4.3.1.5 Stretched-Exponential distribution

The images that were obtained with the mentioned combination of  $b$  values for the Stretched model are shown in Figures 4.67 ( $DDC$  map) and 4.68 ( $\alpha$  map). In the map, the tumor is visible until the image with the  $b$  value  $800 \text{ s/mm}^2$  is removed, then the outlines of the lesion become less detectable.

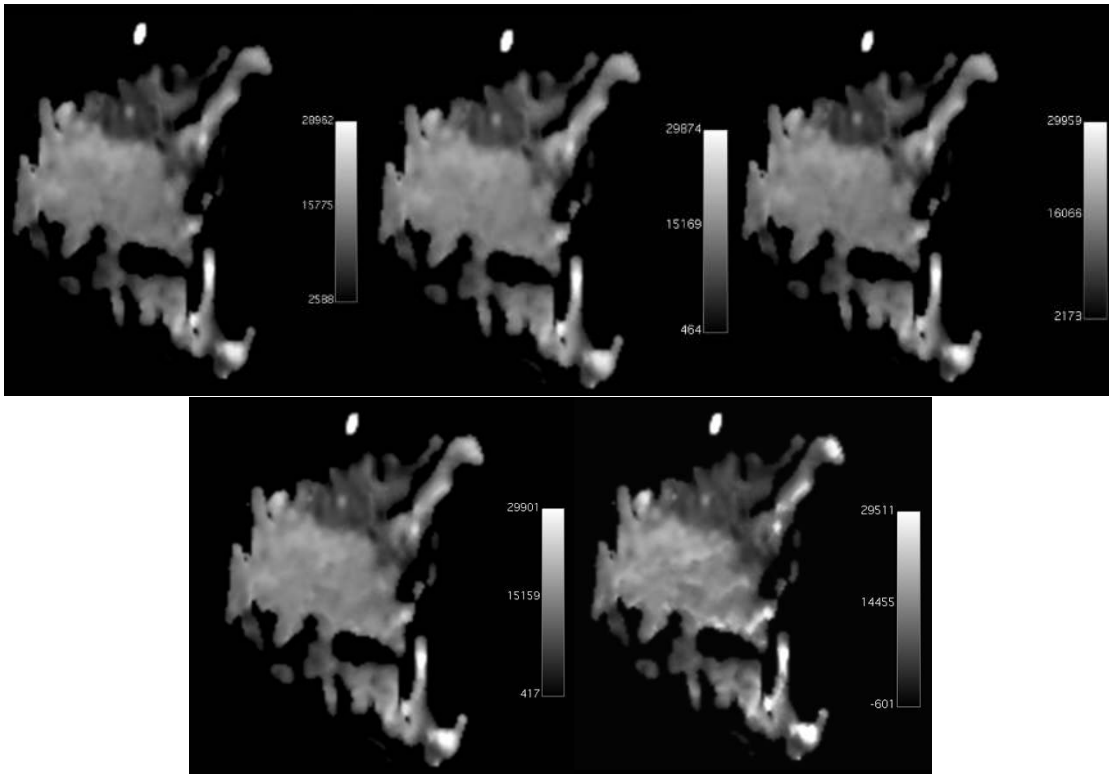


Figure 4.67:  $DDC$  maps (scaling factor of  $1 \times 10^7$  and in  $\text{mm}^2/\text{s}$ ) of a breast with a malignant lesion (invasive ductal carcinoma) which show the quality decrease when are applied with images with less  $b$  values. The  $b$  values were removed in the order:  $600 \text{ s/mm}^2$ ,  $2000 \text{ s/mm}^2$ ,  $200 \text{ s/mm}^2$ ,  $800 \text{ s/mm}^2$  and  $1000 \text{ s/mm}^2$ , respectively.

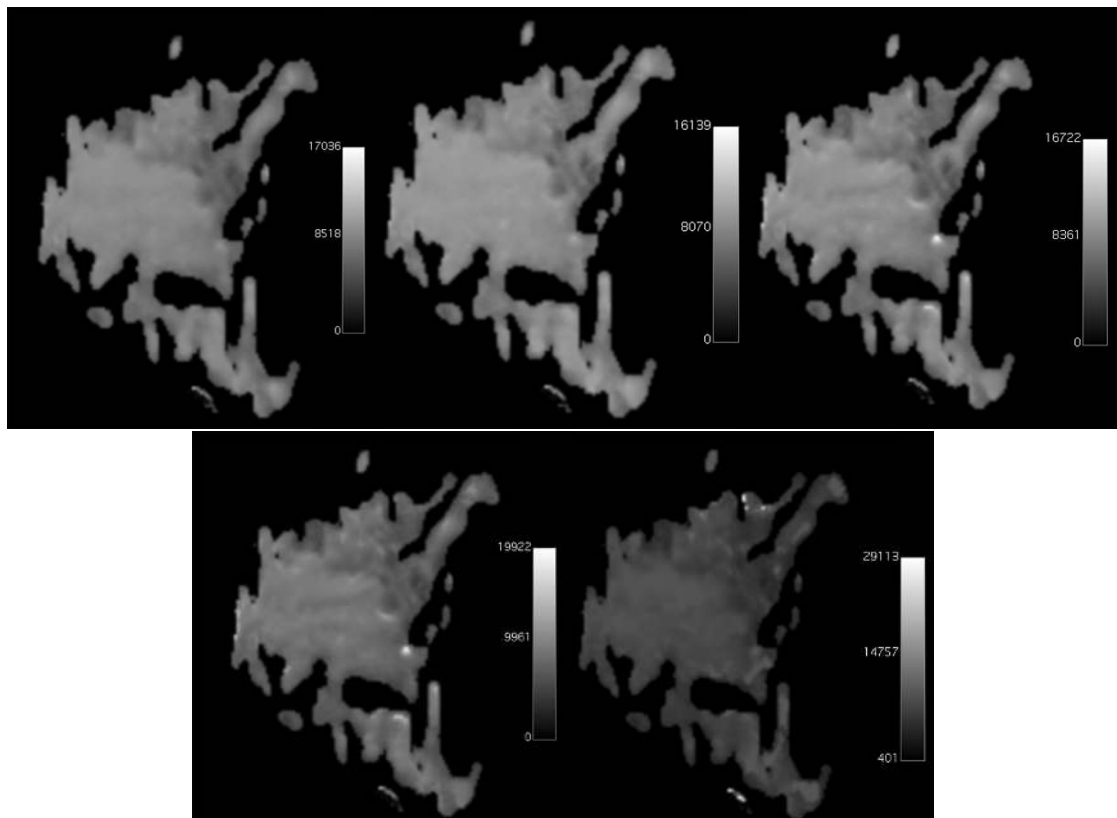


Figure 4.68:  $\alpha$  maps (scaling factor of  $1 \times 10^4$  and with no units since it is dimensionless) of a breast with a malignant lesion (invasive ductal carcinoma) which show the quality decrease when are applied with images with less  $b$  values. The  $b$  values were removed in the order:  $600 \text{ s/mm}^2$ ,  $2000 \text{ s/mm}^2$ ,  $200 \text{ s/mm}^2$ ,  $800 \text{ s/mm}^2$  and  $1000 \text{ s/mm}^2$ , respectively.



#### 4.3.1.6 Goodness-of-fit maps

In order to evaluate how well the fitting process was performed, the goodness of fit maps were compared for each model. The maps are in agreement with the previous results which conclude that when the models that are tested with only three  $b$  values the quality decreases. The following images are of 3  $b$  values. The previous studied amount are in appendix A.

The goodness-of-fit maps that were obtained with the IVIM model, don't show a big difference between each other, which goes in agreement with the results in 4.3.1.2.

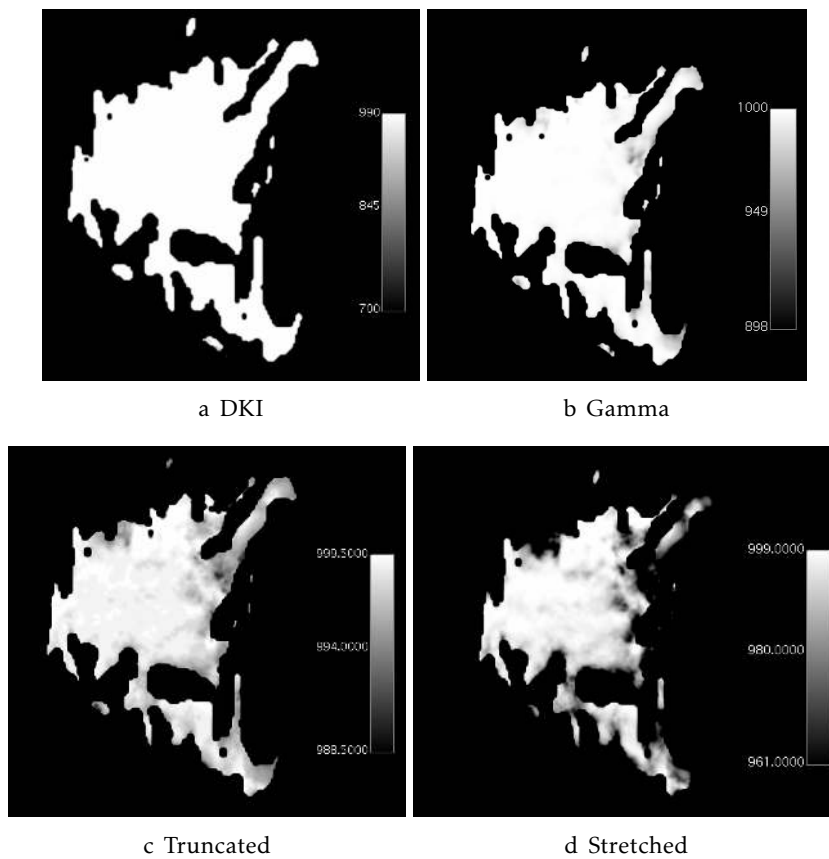


Figure 4.69: Goodness-of-fit map (scaling factor of  $1 \times 10^3$ ) for DKI, Gamma, Truncated and Stretched models applied to a breast with a malignant lesion (invasive ductal carcinoma) when the image with the  $b$  value  $1000 \text{ s/mm}^2$  was removed. The range of greyscale shows that fitting wasn't as good for IVIM as it was for DKI and Gamma.

### 4.3.2 Noise tests

In order to see how the noise affects the obtained parametric maps, several amounts of noise were added (10%, 15%, 20%, 25%, 30% and 35%) like it was mentioned in 3.3.2. Afterwards it was tested how all of the models handled the noise. Looking at the images it is possible to conclude that the quality of the images decreases and when the noise is already at 35% it is difficult to clearly identify the tumor in the image.

The conclusion that is reached after evaluating all of the following images is that when the amount of noise is over 15% too much information is lost, which mean that the suggestion to give the user would be to use images of amounts of noise lower than 15%. The goodness-of-fit maps for all the models are in the Appendix A.

#### 4.3.2.1 DKI

The images that were obtained with the different amounts of noise for the DKI model are shown in Figures 4.70 (*MD* map) and 4.71 (*MK* map). The maps that were obtained with images with 10% and 15% of noise show the lesion very clearly. However, as the noise increases beyond 15% the lesion starts getting difficult to locate in the image, specially in the *MK* maps. Because of this, the suggestion for the user would be to not use the DKI model in images with an amount of noise bigger than 15%.

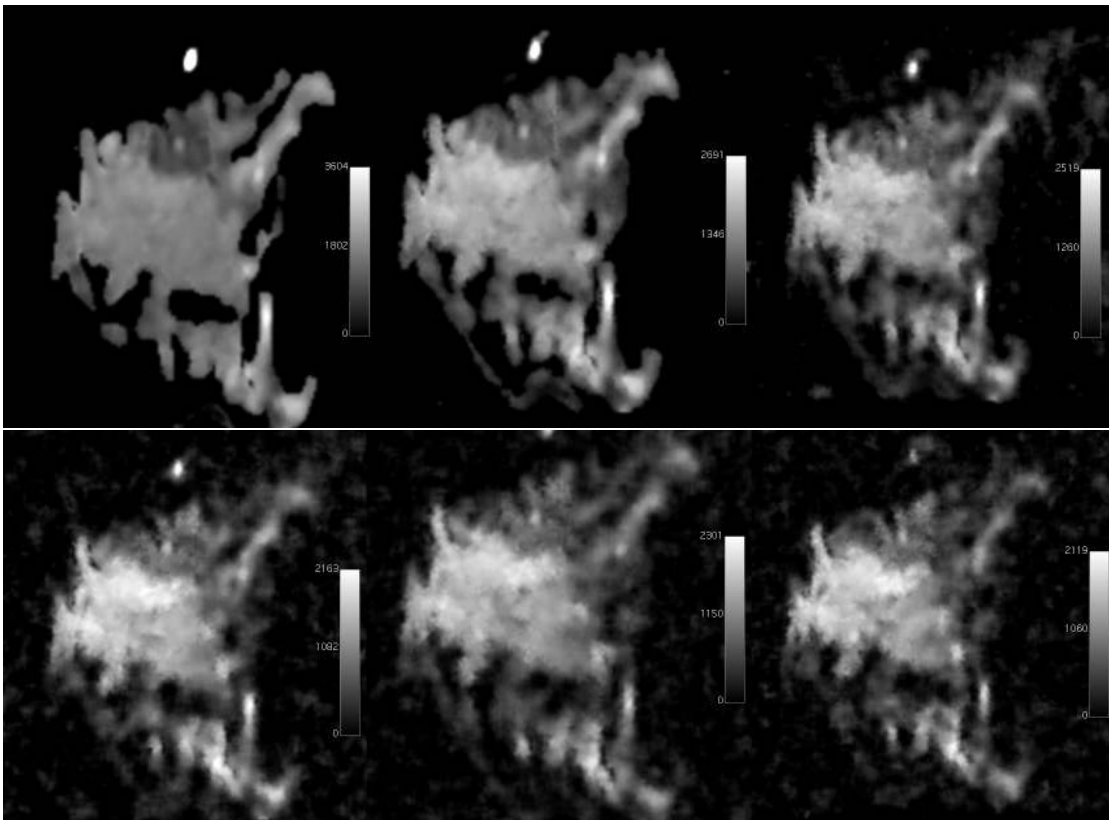


Figure 4.70: MD maps (scaling factor of  $1 \times 10^6$  and in  $\text{mm}^2/\text{s}$ ) of a breast with a malignant lesion (invasive ductal carcinoma) which show the quality decrease when are applied to images with 10%, 15%, 20%, 25%, 30% and 35% amount of noise, respectively..

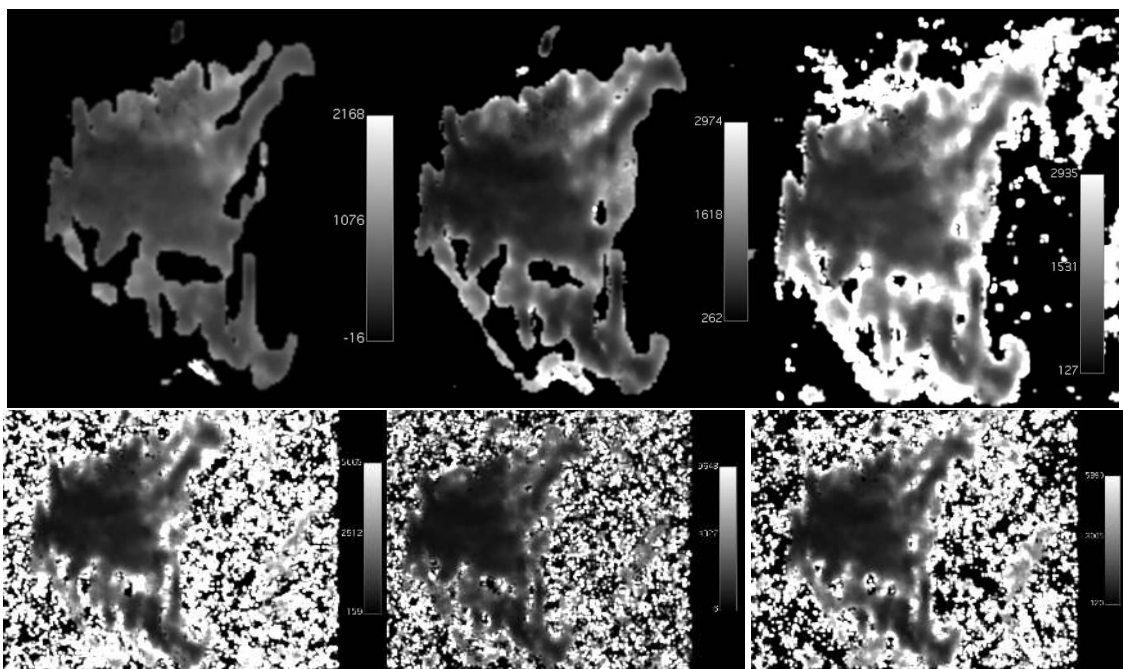


Figure 4.71: *MK* maps (scaling factor of  $1 \times 10^3$  with no units since it is dimensionless) of a breast with a malignant lesion (invasive ductal carcinoma) which show the quality decrease when are applied to images with 10%, 15%, 20%, 25%, 30% and 35% amount of noise, respectively.

## 4.3.2.2 IVIM

The images that were obtained with the different amounts of noise for the IVIM model are shown in Images 4.72 ( $D^*$  map), 4.73 ( $D$  map) and 4.74 ( $f$  map).  $D^*$  and  $f$  have already been mentioned by not having enough quality since the lesion is very difficult to detect. When these maps are applied in Figures with noise, the quality decreases even more drastically than any other maps. When the noise of the image is over 15% it is impossible to detect the lesion. However, the same does not happen with the  $D$  map. This map handles the noise better in the sense that the lesion can be detected in images with higher amount of noise. At 20% the lesion is still visible but poorly, so the user would be advised to use images with an amount of noise lower than 20%.

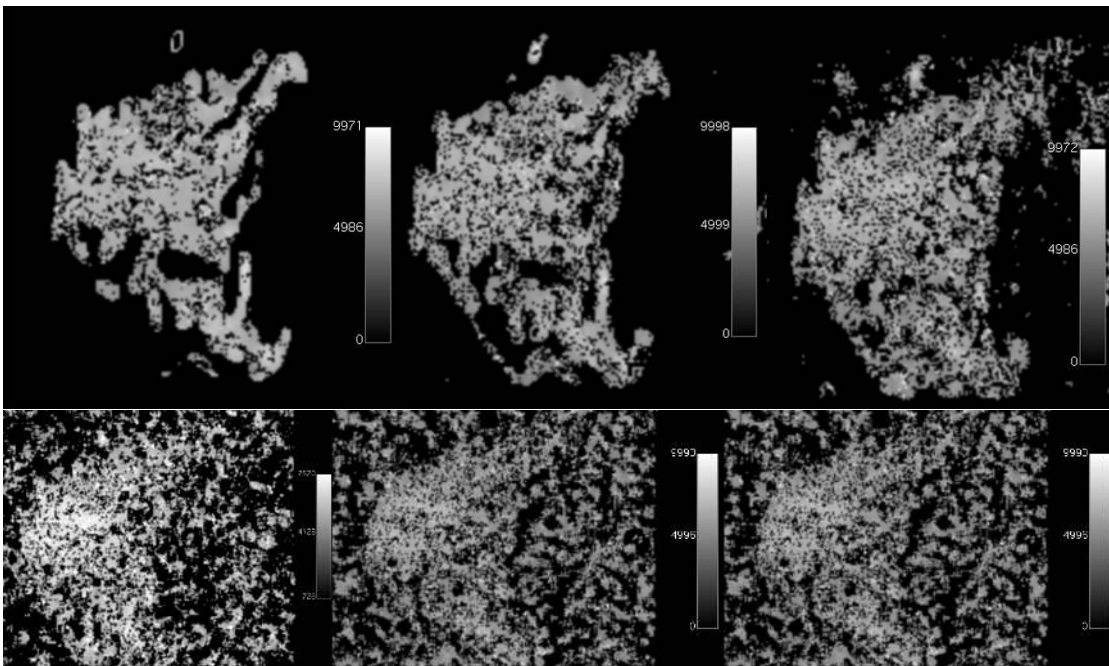


Figure 4.72:  $D^*$  maps (scaling factor of  $1 \times 10^6$  and in  $\text{mm}^2/\text{s}$ ) of a breast with a malignant lesion (invasive ductal carcinoma) which show the quality increase when are applied to images with 10%, 15%, 20%, 25%, 30% and 35% amount of noise, respectively.

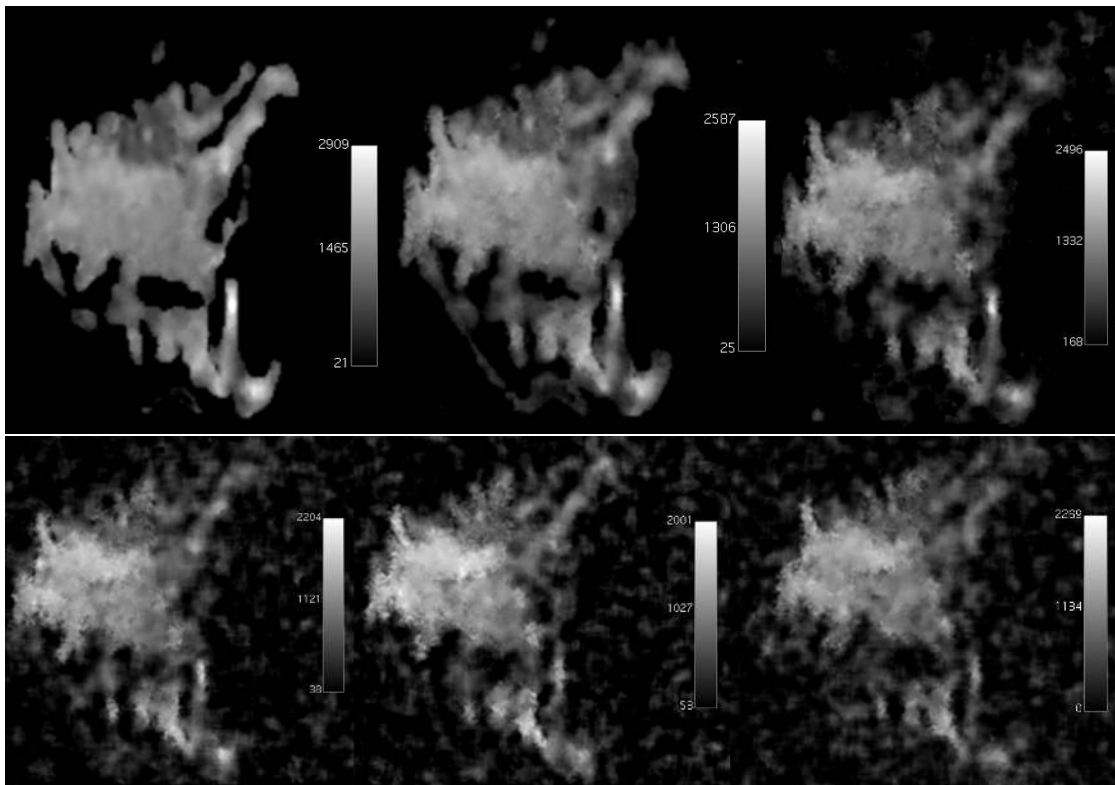


Figure 4.73:  $D$  maps (scaling factor of  $1 \times 10^6$  and in  $\text{mm}^2/\text{s}$ ) of a breast with a malignant lesion (invasive ductal carcinoma) which show the quality decrease when are applied to images with 10%, 15%, 20%, 25%, 30% and 35% amount of noise, respectively.

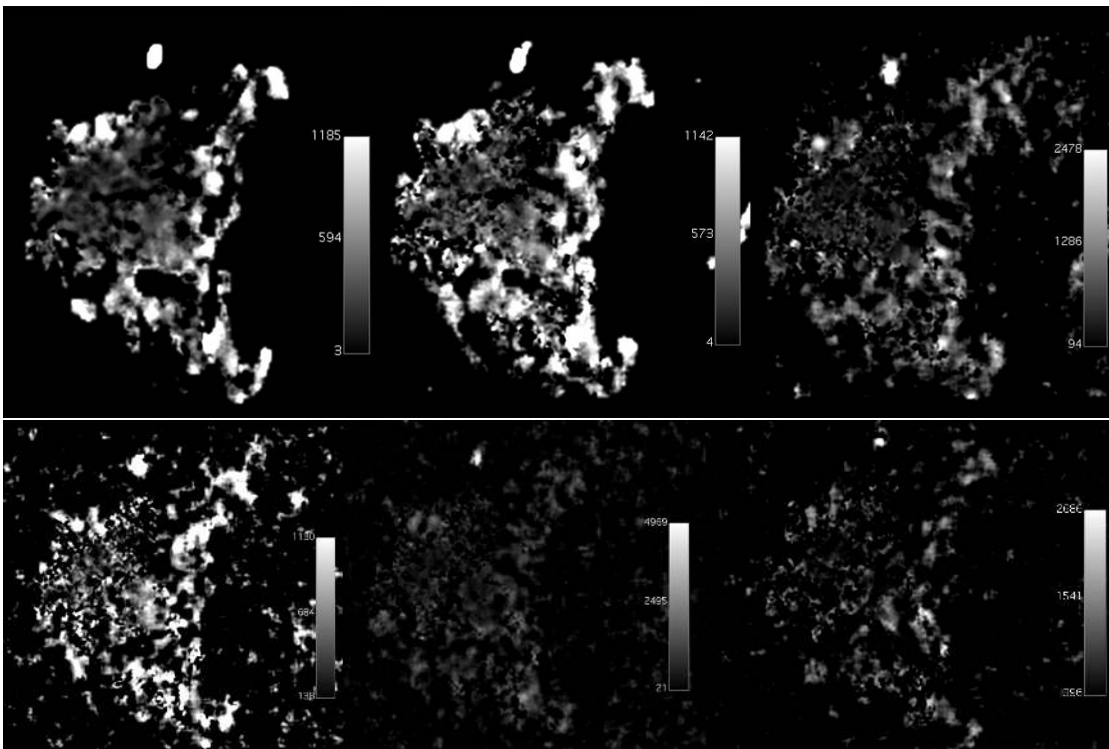


Figure 4.74:  $f$  maps (scaling factor of  $1 \times 10^4$  and in %) of a breast with a malignant lesion (invasive ductal carcinoma) which show the quality increase when are applied to images with 10%, 15%, 20%, 25%, 30% and 35% amount of noise, respectively.

### 4.3.2.3 Gamma distribution

The images that were obtained with the different amounts of noise for the Gamma model are shown in Figures 4.75 ( $\theta$  map), 4.76 ( $\kappa$  map), 4.77 (S1 map), 4.78 (S2 map) and 4.79 (S3 map). In all five maps that were obtained, the same conclusion was reached, when the image used has a higher amount of noise than 15% the quality of the map decreases to a point where the detection of the tumor location become difficult. The S3 map was the only map that even at higher values of noise, the tumor was still detectable.

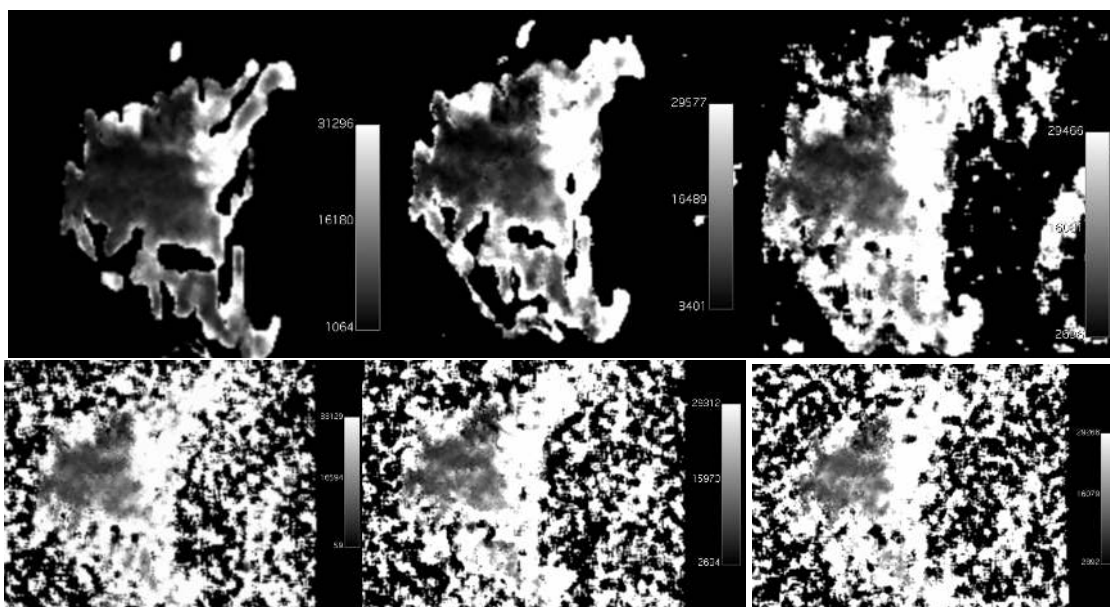


Figure 4.75:  $\theta$  maps (scaling factor of  $1 \times 10^4$  and in  $\text{mm}^2/\text{s}$ ) of a breast with a malignant lesion (invasive ductal carcinoma) which show the quality increase when applied to images with 10%, 15%, 20%, 25%, 30% and 35% amount of noise, respectively.



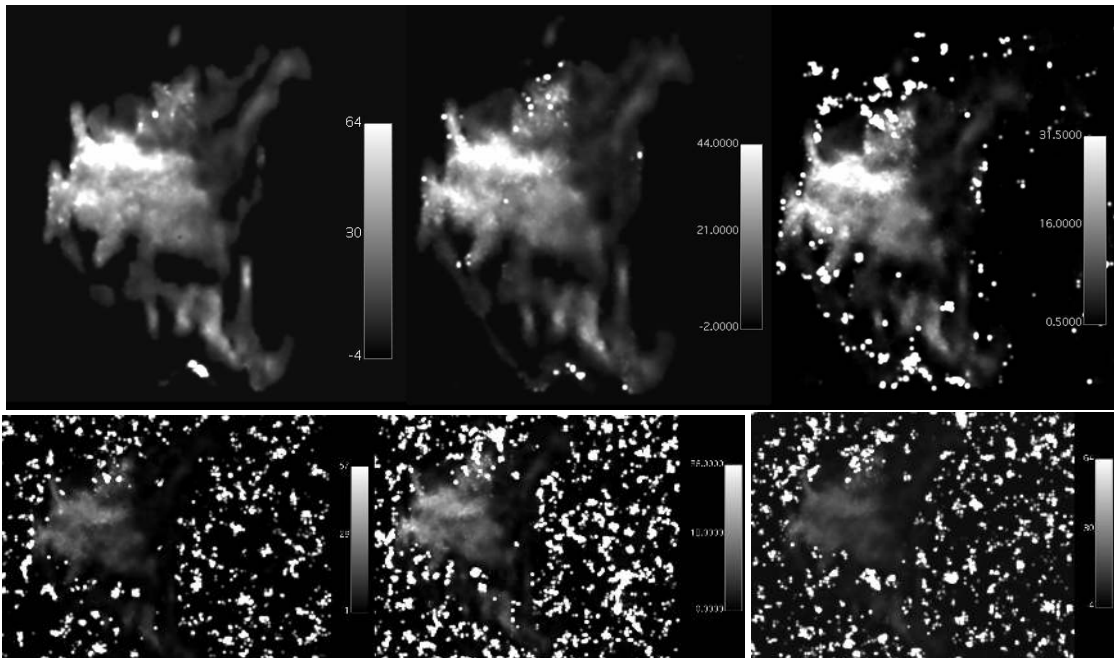


Figure 4.76:  $\kappa$  maps (scaling factor of 10 and with no units since it is dimensionless) of a breast with a malignant lesion (invasive ductal carcinoma) which show the quality increase when applied to images with 10%, 15%, 20%, 25%, 30% and 35% amount of noise, respectively.

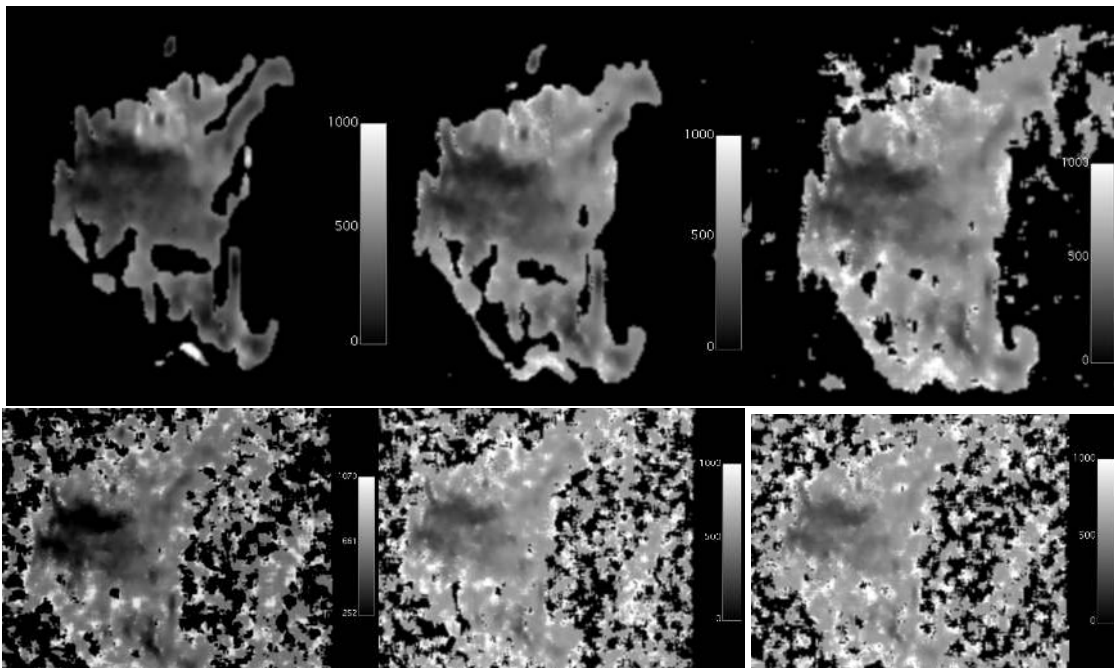


Figure 4.77:  $S_1$  maps (scaling factor of  $1 \times 10^3$  and in %) of a breast with a malignant lesion (invasive ductal carcinoma) which show the quality decrease when are applied to images with 10%, 15%, 20%, 25%, 30% and 35% amount of noise, respectively.

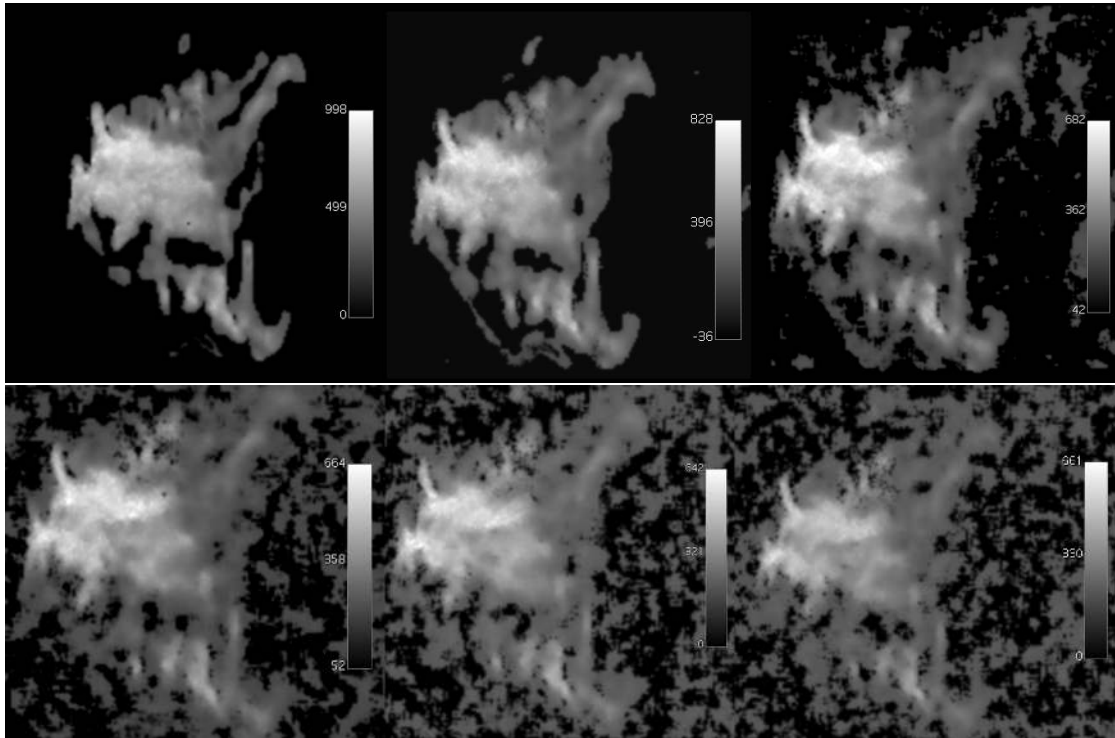


Figure 4.78: S2 maps (scaling factor of  $1 \times 10^3$  and in %) of a breast with a malignant lesion (invasive ductal carcinoma) which show the quality increase when are applied to images with 10%, 15%, 20%, 25%, 30% and 35% amount of noise, respectively.

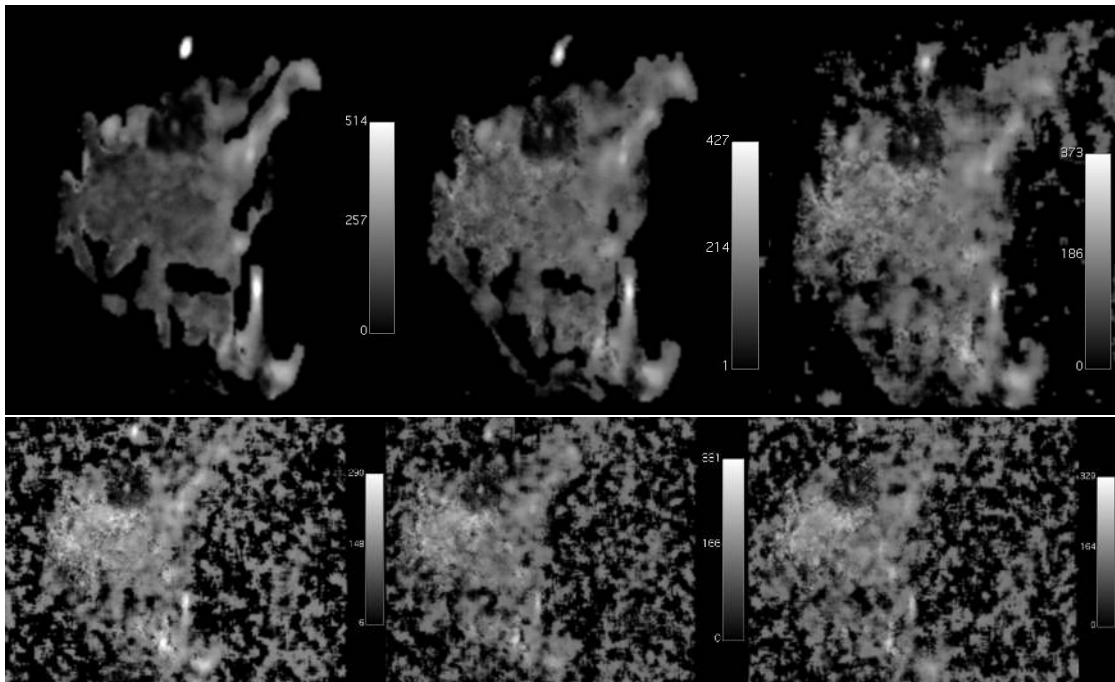


Figure 4.79: S3 maps (scaling factor of  $1 \times 10^3$  and in %) of a breast with a malignant lesion (invasive ductal carcinoma) which show the quality increase when are applied to images with 10%, 15%, 20%, 25%, 30% and 35% amount of noise, respectively.

#### 4.3.2.4 Truncated Gaussian distribution

The images that were obtained with the mentioned combination for the Truncated model are shown in Figures 4.80 ( $\sigma$  map) and 4.81 ( $ADC$  map). When the amount of noise of the images tested was higher than 15%, the quality of the maps decreases to point where is difficult to detect the tumor. However, the tumor is still detectable at images with 20% of noise, which means that the user would be advised to use images with an amount of noise lower than 20%.

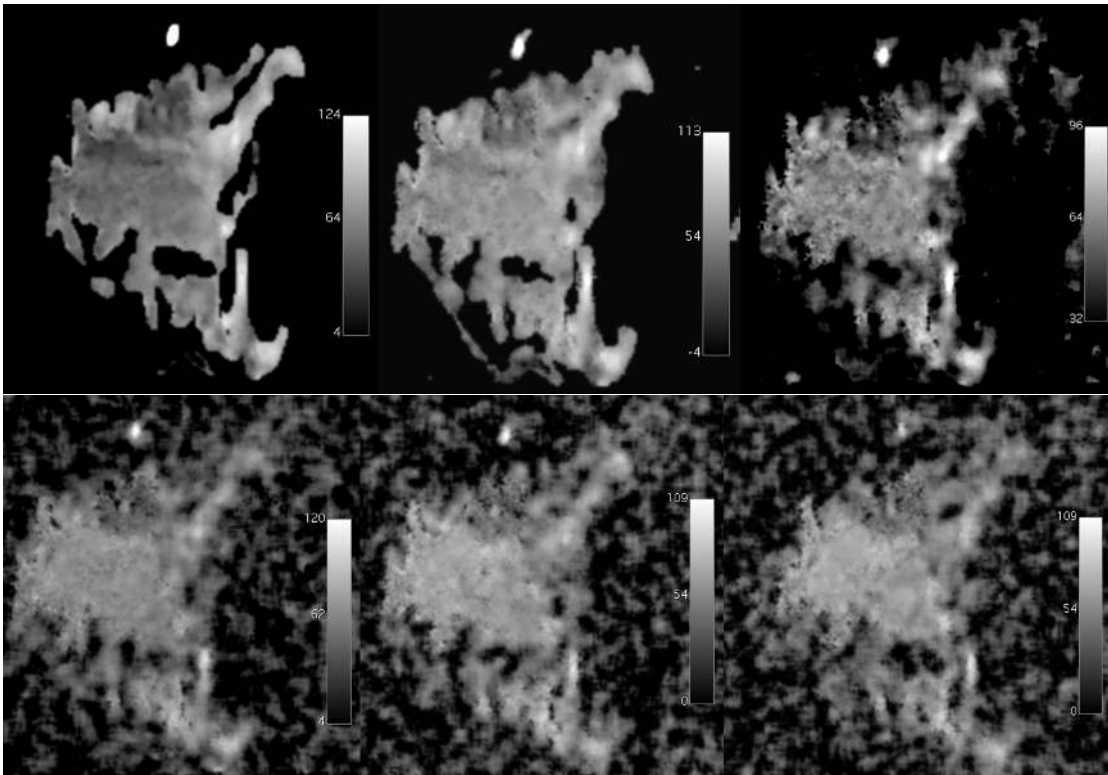


Figure 4.80:  $\sigma$  maps (scaling factor of  $1 \times 10^5$  and in  $\text{mm}^2/\text{s}$ ) of a breast with a malignant lesion (invasive ductal carcinoma) which show the quality increase when applied to images with 10%, 15%, 20%, 25%, 30% and 35% amount of noise, respectively.

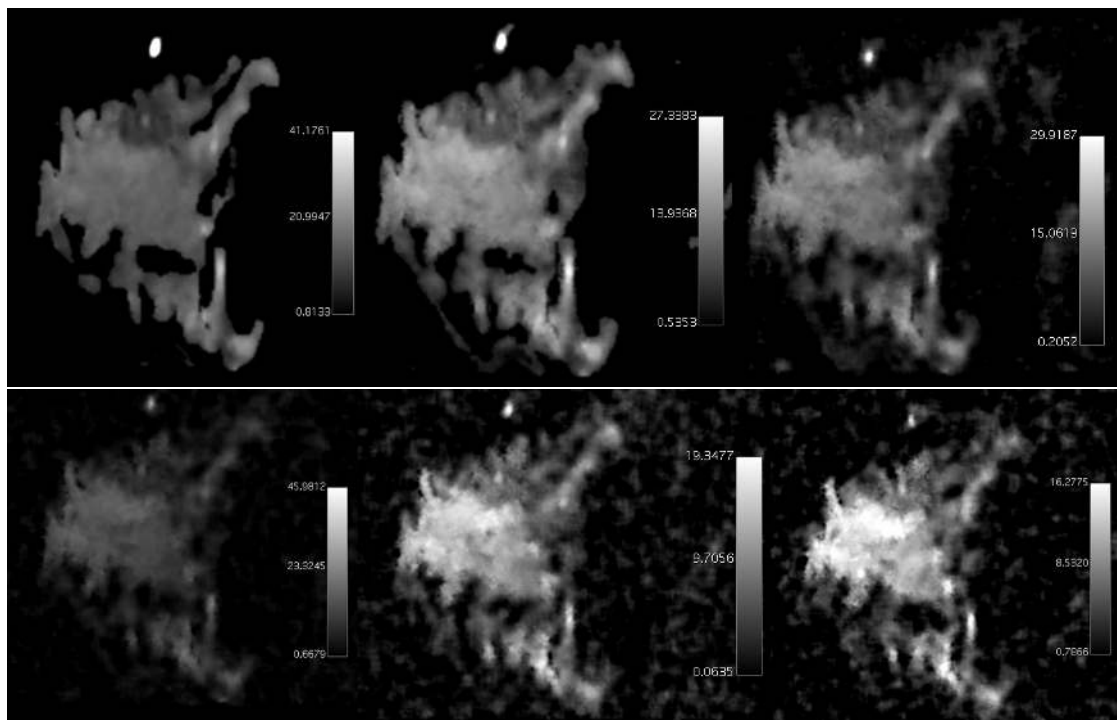


Figure 4.81: ADC maps (scaling factor of  $1 \times 10^4$  and in  $\text{mm}^2/\text{s}$ ) of a breast with a malignant lesion (invasive ductal carcinoma) which show the quality increase when are applied to images with 10%, 15%, 20%, 25%, 30% and 35% amount of noise, respectively.

#### 4.3.2.5 Stretched-Exponential distribution

The images that were obtained with the mentioned combination for the Stretched model are shown in Figures 4.82 ( $DDC$  map) and 4.83 ( $\alpha$  map). This was model that better handled the noise because when the amount of noise is at 35% the lesion is still detectable. However, in the case of the  $DDC$  map, a lot of information of the image is lost as the noise increases which is noticeable around the tumor area.

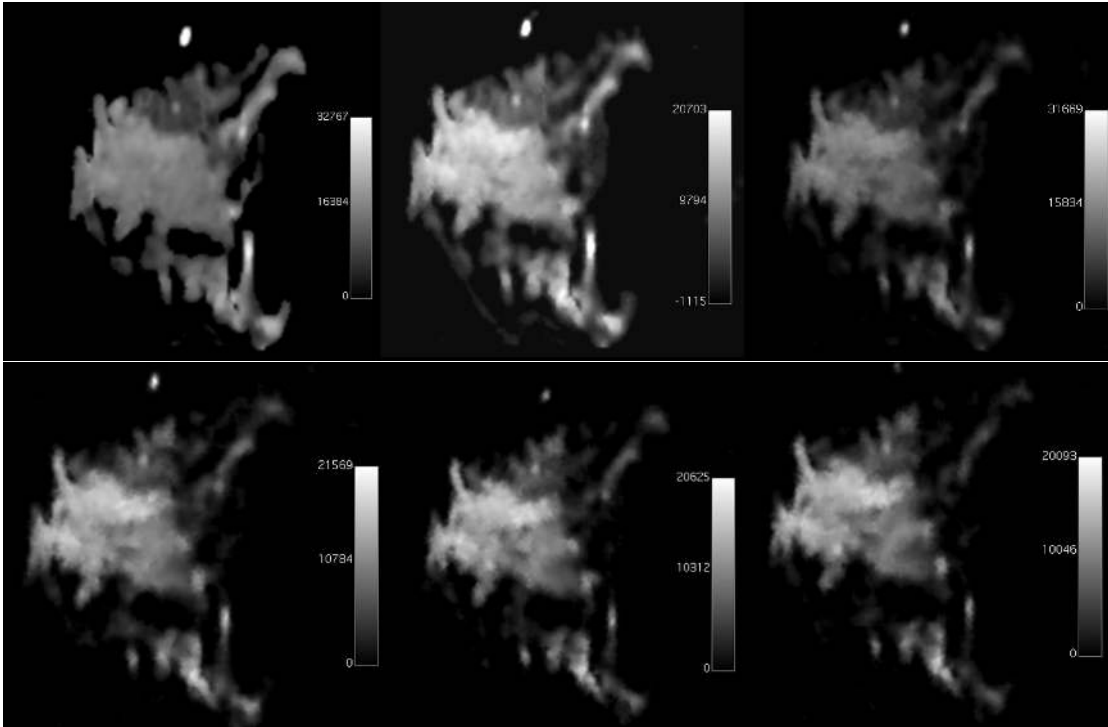


Figure 4.82:  $DDC$  maps (scaling factor of  $1 \times 10^7$  and in  $\text{mm}^2/\text{s}$ ) of a breast with a malignant lesion (invasive ductal carcinoma) which show the quality increase when are applied to images with 10%, 15%, 20%, 25%, 30% and 35% amount of noise, respectively.

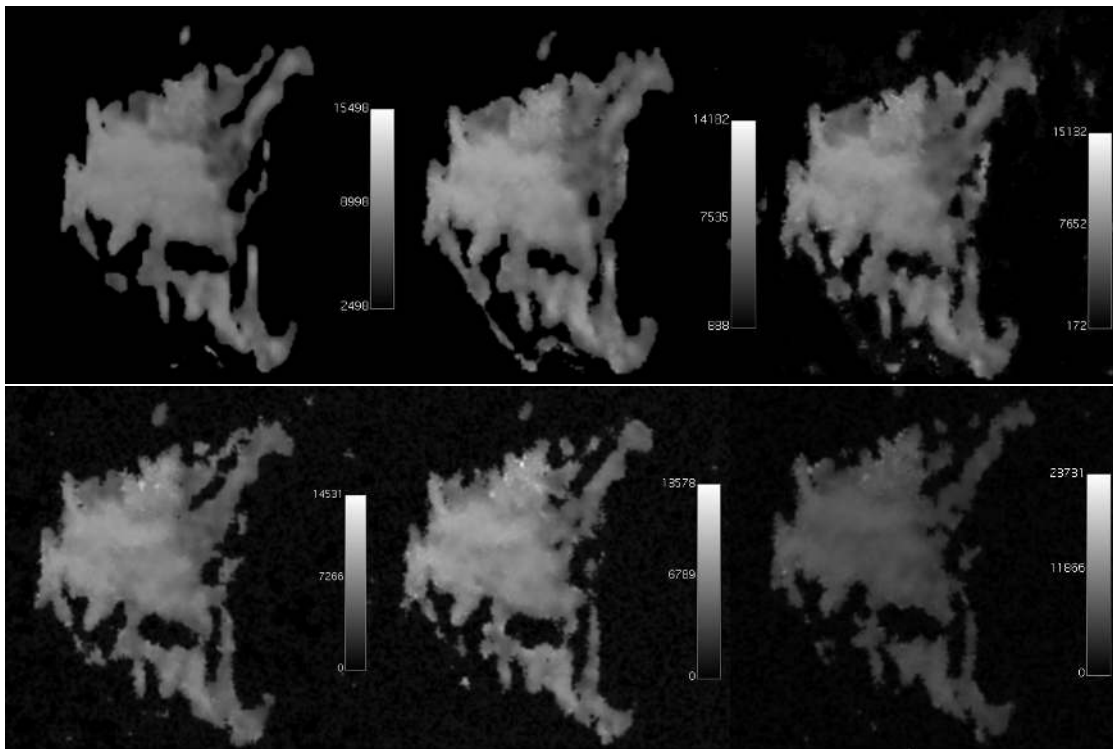


Figure 4.83:  $\alpha$  maps (scaling factor of  $1 \times 10^4$  and with no units since it is dimensionless) of a breast with a malignant lesion (invasive ductal carcinoma) which show the quality increase when applied to images with 10%, 15%, 20%, 25%, 30% and 35% amount of noise, respectively.

## CONCLUSIONS AND FUTURE WORK

In this chapter are the conclusion of the the dissertation along with final considerations and possible future work.

In this work it was proposed the development of an OsiriX plug-in, using non-Gaussian models in order to characterize lesions. In spite of existing other plug-ins for image processing, to our knowledge there hasn't been developed a plug-in for these particular models. Besides, the developed plug-in has the advantage to not only process one non-Gaussian model, but also four more, giving the user a more wider spectrum of choices and also the chance to compare between parametric maps.

In the beginning the plug-in only had to produce parametric maps, however, it was found useful to be able to obtain the parametric values of the models from a ROI drawn around the tumor area. Because of this, it was added a new section in order to obtain these values, which can also be an alternative for when the images that are being tested don't have the most appropriate protocol to produce parametric maps. For example, few  $b$ -values or a big amount of noise.

The resulting plug-in can detect successfully the difference between malignant and benign lesions through parametric maps and values. The goodness of fit and the plots with the curve fitting, show that the fitting of the models was correct and well done. The only model that didn't detect the difference as well was the IVIM model and this can be justified by not testing it with the most correct  $b$ -values.

In order to better inform the user on how to obtain the best images possible with the plug-in, it was tested with several different amounts of  $b$  values and added noise. The conclusions of this research will help the user to choose which images to use and also warn him that the quality of the maps can decrease if not payed attention them.

One of the biggest challenges on working on the plug-in was the lack of knowledge in Objective-C language and how to work with OsiriX methods and classes. It was a

challenge to learn a new language, however, it was very rewarding to see the ending result. The most difficult part was how to access the methods and classes of OsiriX in order to make the program work. For example, the plug-in applies full dynamic after the images are uploaded and to find the method to do it, it was needed to check the OsiriX source code. Almost every methods that were worked with were found in the source code since there isn't that many information online.

For future work, it would begin with getting IVIM images that are more suitable to test the IVIM and IVIM/DKI models on the plug-in. It would also be important to reduce the time of processing, in spite of already been tried in this work with parallel computing. Another step that can be added to the plug-in, would be to give the user the opportunity to choose which  $b$  values, that the series of images have, to run the models on. Also, the application of this plug-in on a bigger spectrum of images would be imperative in order to check if it really works on every single image with the right protocol.

Overall, the objectives of this dissertation were met. The application of the IVIM model wasn't as successful as for the other models, however, it showed potential to work.

As a final conclusion, I really enjoyed working on this dissertation and found the work very rewarding, specially when the main goals of it were all met.



## BIBLIOGRAPHY

- [1] R. L. Siegel, K. D. Miller, and A. Jemal. "Cancer statistics , 2015". In: *CA Cancer J Clin* 65.1 (2015), p. 21254. DOI: 10.3322/caac.21254.
- [2] Web. *Cancro da Mama : Liga Portuguesa Contra o Cancro*. URL: <https://www.ligacontracancro.pt/cancro-da-mama/> (visited on 01/26/2016).
- [3] L. Maher, M. McGarry, A. McMahon, Y. Slowey, and K. Stacey. "A Comparative Dataset of Six Cancers in the European Union". In: *Trinity Student Medical Journal* (2004), pp. 42–49.
- [4] N. Boyd, J. Byng, R. Jong, E. Fishell, L. Little, A. Miller, G. Lockwood, D. Tritchler, and M. Yaffe. "Quantitative classification of mammographic densities and breast cancer risk: results from the Canadian National Breast Screening Study." In: *Journal of the National Cancer Institute* 87.9 (1995), pp. 670–675. ISSN: 0027-8874. DOI: 10.1093/jnci/87.9.670.
- [5] H. Rahbar and S. C. Partridge. "Multiparametric MR Imaging of Breast Cancer". In: *Magnetic Resonance Imaging Clinics of North America* 24.1 (2016), pp. 223–238. ISSN: 10649689. DOI: 10.1016/j.mric.2015.08.012. URL: <http://linkinghub.elsevier.com/retrieve/pii/S1064968915001105>.
- [6] A. J. Murray and D. M. Davies. "The genetics of breast cancer". In: *Surgery (United Kingdom)* 31.3 (2013), pp. 1–3. ISSN: 02639319. DOI: 10.1016/j.mpsur.2012.10.019. URL: <http://dx.doi.org/10.1016/j.mpsur.2009.11.005>.
- [7] M. Alakhras, R. Bourne, M. Rickard, K. H. Ng, M. Pietrzyk, and P. C. Brennan. "Digital tomosynthesis: A new future for breast imaging?" In: *Clinical Radiology* 68.5 (2013), pp. 225–236. ISSN: 00099260. DOI: 10.1016/j.crad.2013.01.007.
- [8] A. Antoniou et al. "Average risks of breast and ovarian cancer associated with BRCA1 or BRCA2 mutations detected in case Series unselected for family history: a combined analysis of 22 studies." In: *American journal of human genetics* 72.5 (2003), pp. 1117–1130. ISSN: 0002-9297. DOI: 10.1086/375033.
- [9] B. W. Saslow D Boetes C. "American Cancer Society guide- lines for breast screening with MRI as an adjunct to mammography." In: *CA Cancer J Clin* 57.57 (2007), pp. 75–89.

- [10] C. H. Lee, D. D. Dershaw, D. Kopans, P. Evans, B. Monsees, D. Monticciolo, R. J. Brenner, L. Bassett, W. Berg, S. Feig, E. Hendrick, E. Mendelson, C. D’Orsi, E. Sickles, and L. W. Burhenne. “Breast Cancer Screening With Imaging: Recommendations From the Society of Breast Imaging and the ACR on the Use of Mammography, Breast MRI, Breast Ultrasound, and Other Technologies for the Detection of Clinically Occult Breast Cancer”. In: *Journal of the American College of Radiology* 7.1 (2010), pp. 18–27. ISSN: 15461440. DOI: 10.1016/j.jacr.2009.09.022. URL: <http://linkinghub.elsevier.com/retrieve/pii/S1546144009004803>.
- [11] R. H. Laurie Margolies. “Breast Magnetic Resonance Imaging: An Overview for Nonradiologists”. In: *The Mount Sinai journal of medicine, New York* 76.2 (2009), pp. 598–605. ISSN: 1931-7581. DOI: 10.1002/MSJ.
- [12] I. Thomassin-Naggara, C. De Bazelaire, J. Chopier, M. Bazot, C. Marsault, and I. Trop. “Diffusion-weighted MR imaging of the breast: Advantages and pitfalls”. In: *European Journal of Radiology* 82.3 (2013), pp. 435–443. ISSN: 0720048X. DOI: 10.1016/j.ejrad.2012.03.002. URL: <http://dx.doi.org/10.1016/j.ejrad.2012.03.002>.
- [13] L. Nogueira, S. Brandão, E. Matos, R. Gouveia Nunes, J. Loureiro, I. Ramos, and H. Alexandre Ferreira. “Application of the diffusion kurtosis model for the study of breast lesions”. In: *Eur Radiol* 24 (2014), pp. 1197–1203. DOI: 10.1007/s00330-014-3146-5.
- [14] C. Liu, C. Liang, Z. Liu, S. Zhang, and B. Huang. “Intravoxel incoherent motion (IVIM) in evaluation of breast lesions: Comparison with conventional DWI”. In: *European Journal of Radiology* 82.12 (2013), pp. 782–789. ISSN: 0720048X. DOI: 10.1016/j.ejrad.2013.08.006.
- [15] F. Borlinhas, L. Nogueira, S. Brandao, R. G. Nunes, J. Loureiro, I. Ramos, and H. A. Ferreira. “Gamma distribution model in breast cancer diffusion-weighted imaging”. In: *2015 IEEE 4th Portuguese Meeting on Bioengineering (ENBENG)* February (2015), pp. 1–1. DOI: 10.1109/ENBENG.2015.7088819. URL: <http://ieeexplore.ieee.org/lpdocs/epic03/wrapper.htm?arnumber=7088819>.
- [16] H. Shinmoto, K. Oshio, C. Tamura, S. Soga, T. Okamura, K. Yamada, T. Kaji, and R. V. Mulkern. “Diffusion-weighted imaging of prostate cancer using a statistical model based on the gamma distribution”. In: *Journal of Magnetic Resonance Imaging* 62 (2014), pp. 56–62. ISSN: 15222586. DOI: 10.1002/jmri.24761.
- [17] X. Liu, L. Zhou, W. Peng, H. Wang, and Y. Zhang. “Comparison of stretched-Exponential and monoexponential model diffusion-Weighted imaging in prostate cancer and normal tissues”. In: *Journal of Magnetic Resonance Imaging* 42.4 (2015), pp. 1078–1085. ISSN: 15222586. DOI: 10.1002/jmri.24872.

- [18] C.-Y. Lee and J. P. Debbins. “The sensitivities of the phenomenological DWI models in the presence of cellular compartments”. In: *Proc. Intl. Soc. Mag. Reson. Med.* 19 19 (2011), p. 414.
- [19] C. Hogg, Peter, Kelly, Judith, Mercer. *Digital mammography: A Holistic Approach*. 2015, pp. 5–8. ISBN: 9783319048307.
- [20] American Cancer Society. *If You Have Breast Cancer*. 2016. URL: <http://www.cancer.org/cancer/breastcancer/if-you-have-breast-cancer> (visited on 09/07/2016).
- [21] G. M. Cooper. *The Cell: A Molecular Approach. 2nd edition. The Development and Causes of Cancer*. Sinauer Associates, 2000.
- [22] S. Edelman, Robert R., Warach. “Magnetic Resonance Imaging”. In: *The New England Journal of Medicine* 328.10 (1993), pp. 708–716.
- [23] D. et al McRobbie. *MRI: From Picture to Proton*. Vol. 85. 4. 2003, pp. 504–505. ISBN: 9780521865272. DOI: 10.1097/00004032-200310000-00020.
- [24] C. Wan, C. Lee, C. Lui, C. Fong, and K. Lau. “Apparent diffusion coefficient in differentiation between malignant and benign breast masses: does size matter?” In: *Clinical Radiology* 71.2 (2015), pp. 170–177. ISSN: 00099260. DOI: 10.1016/j.crad.2015.11.006. URL: <http://linkinghub.elsevier.com/retrieve/pii/S0009926015004432>.
- [25] S. J. Veraart Jelle. “Diffusion kurtosis imaging”. In: *MRI in Psychiatry* 1 (2014), pp. 77–86. ISSN: 08908567. DOI: 10.1097/01.chi.0000246064.93200.e8.
- [26] M. Rowe, B. Siow, D. C. Alexander, and U. Ferizi. “Concepts of diffusion in MRI”. In: *Diffusion Tensor Imaging* (2016), pp. 23–35. DOI: 10.1007/978-1-4939-3118-7.
- [27] D. Wu, G. Li, J. Zhang, S. Chang, J. Hu, Y. Dai, D Wu, G Li, J Zhang, S Chang, J Hu, and A. Leemans. “Characterization of Breast Tumors Using Diffusion Kurtosis Imaging (DKI)”. In: *PLoS ONE* 9.11 (2014), pp. 1–8. DOI: 10.1371/journal.pone.0113240.
- [28] S. C. Partridge and E. S. McDonald. “Diffusion Weighted Magnetic Resonance Imaging of the Breast: Protocol Optimization, Interpretation, and Clinical Applications”. In: *Magnetic Resonance Imaging Clinics of North America* 21.3 (2013), pp. 601–624. ISSN: 10649689. DOI: 10.1016/j.mric.2013.04.007. arXiv: NIHMS150003.
- [29] S. K. Mukherji, T. L. Chenevert, and M. Castillo. “Diffusion-Weighted Magnetic Resonance Imaging”. In: *J Neuro-Ophthalmol* 22.2 (2002), pp. 118–122. DOI: 10.1097/01.WNO.0000019698.15867.57.
- [30] L.-J. M. M. Le Bihan D, Breton E, Lallemand D, Grenier P, Cabanis E. “MR imaging of intravoxel incoherent motions: application to diffusion and perfusion in neurologic disorders.” In: *Radiology* 161 (1986), pp. 401–407.

- [31] S. M. A. Panek Rafal, Borri Marco, Orton Matthew, O'Flynn Elizabeth, Morgan Veronica, Giles Sharon L., deSouza Nandita, Leach Martin O. "Evaluation of diffusion models in breast cancer". In: *Medical physics* 42.8 (2015), pp. 4833–4839. DOI: 10.1118/1.4927255.
- [32] H. Lu, J. H. Jensen, A. Ramani, and J. A. Helpert. "Three-dimensional characterization of non-gaussian water diffusion in humans using diffusion kurtosis imaging". In: *NMR in biomedicine* 19 (2006), pp. 236–247. DOI: 10.1002/nbm.1020.
- [33] J. H. Jensen, J. A. Helpert, A. Ramani, H. Lu, and K. Kaczynski. "Diffusional Kurtosis Imaging: The Quantification of Non-Gaussian Water Diffusion by Means of Magnetic Resonance Imaging". In: *Magnetic Resonance in Medicine* 53 (2005), pp. 1432–1440. DOI: 10.1002/mrm.20508.
- [34] J. H. Jensen and J. A. Helpert. "MRI quantification of non-Gaussian water diffusion by kurtosis analysis". In: *NMR in Biomedicine* 23 (2010), pp. 698–710. DOI: 10.1002/nbm.1518.
- [35] R. N. Henriques, M. M. Correia, R. G. Nunes, and H. A. Ferreira. "Exploring the 3D geometry of the diffusion kurtosis tensor—Impact on the development of robust tractography procedures and novel biomarkers". In: *NeuroImage* 111 (2015), pp. 85–99. DOI: 10.1016/j.neuroimage.2015.02.004.
- [36] K. Sun, X. Chen, W. Chai, X. Fei, C. Fu, X. Yan, Y. Zhan, K. Chen, K. Shen, and F. Yan. "Breast cancer: Diffusion Kurtosis MR Imaging—Diagnostic Accuracy and Correlation with Clinical-Pathologic Factors 1". In: *Radiology* 000 (2015).
- [37] M. Iima, K. Yano, M. Kataoka, M. Umehana, K. Murata, S. Kanao, K. Togashi, and D. Le Bihan. "Quantitative Non-Gaussian Diffusion and Intravoxel Incoherent Motion Magnetic Resonance Imaging Differentiation of Malignant and Benign Breast Lesions". In: *Investigative Radiology* • 50.4 (2015), pp. 205–211.
- [38] D. M. Koh, D. J. Collins, and M. R. Orton. "Intravoxel incoherent motion in body diffusion-weighted MRI: Reality and challenges". In: *American Journal of Roentgenology* 196.6 (2011), pp. 1351–1361. ISSN: 0361803X. DOI: 10.2214/AJR.10.5515.
- [39] K. Oshio, H. Shinmoto, R. V. Mulkern, and R. V. Mulkern. "Interpretation of Diffusion MR Imaging Data using a Gamma Distribution Model". In: *Magnetic Resonance in Medical Sciences* 13.3 (2014), pp. 191–195. ISSN: 1347-3182. DOI: 10.2463/mrms.2014-0016. URL: <http://jlc.jst.go.jp/DN/JST.JSTAGE/mrms/2014-0016?lang=en{\&}from=CrossRef{\&}type=abstract>.
- [40] D. A. Yablonskiy, G. L. Bretthorst, and J. J. H. Ackerman. "Statistical model for diffusion attenuated MR signal". In: *Magnetic Resonance in Medicine* 50.4 (2003), pp. 664–669. ISSN: 07403194. DOI: 10.1002/mrm.10578.

- [41] K. M. Bennett, K. M. Schmainda, R. Bennett, D. B. Rowe, H. Lu, and J. S. Hyde. “Characterization of continuously distributed cortical water diffusion rates with a stretched-exponential model”. In: *Magnetic Resonance in Medicine* 50.4 (2003), pp. 727–734. ISSN: 07403194. DOI: 10.1002/mrm.10581.
- [42] T. C. Kwee, C. J. Galb??n, C. Tsien, L. Junck, P. C. Sundgren, M. K. Ivancevic, T. D. Johnson, C. R. Meyer, A. Rehemtulla, B. D. Ross, and T. L. Chenevert. “Comparison of apparent diffusion coefficients and distributed diffusion coefficients in high-grade gliomas”. In: *Journal of Magnetic Resonance Imaging* 31.3 (2010), pp. 531–537. ISSN: 10531807. DOI: 10.1002/jmri.22070. arXiv: NIHMS150003.
- [43] B. Hansen, T. E. Lund, R. Sangill, and N Sune. “Experimentally and Computationally Fast Method for Estimation of a Mean Kurtosis”. In: 1760 (2013), pp. 1754–1760. DOI: 10.1002/mrm.24743.
- [44] Y. Pang, B. Turkbey, M. Bernardo, J. Kruecker, S. Kadoury, M. J. Merino, B. J. Wood, P. A. Pinto, and P. L. Choyke. “Intravoxel incoherent motion MR imaging for prostate cancer: An evaluation of perfusion fraction and diffusion coefficient derived from different b-value combinations”. In: *Magnetic Resonance in Medicine* 69.2 (2013), pp. 553–562. ISSN: 07403194. DOI: 10.1002/mrm.24277.
- [45] E. E. Sigmund, G. Y. Cho, S. Kim, M. Finn, M. Moccaldi, J. H. Jensen, D. K. Sodickson, J. D. Goldberg, S. Formenti, and L. Moy. “Intravoxel incoherent motion imaging of tumor microenvironment in locally advanced breast cancer”. In: *Magnetic Resonance in Medicine* 65.5 (2011), pp. 1437–1447. ISSN: 07403194. DOI: 10.1002/mrm.22740.
- [46] G. Sharma and J. Martin. “MATLAB®: A Language for Parallel Computing”. In: *International Journal of Parallel Programming* 37.1 (2009), pp. 3–36. ISSN: 0885-7458. DOI: 10.1007/s10766-008-0082-5. URL: <http://link.springer.com/10.1007/s10766-008-0082-5>.
- [47] C. Iacconi. “Diffusion and perfusion of the breast”. In: *European Journal of Radiology* 76.3 (2010), pp. 386–390. ISSN: 0720048X. DOI: 10.1016/j.ejrad.2010.03.009. URL: <http://dx.doi.org/10.1016/j.ejrad.2010.03.009>.



TESTING  $b$  VALUES AND NOISE

A.0.3 Goodness of fit maps for the first combination of  $b$  values removal

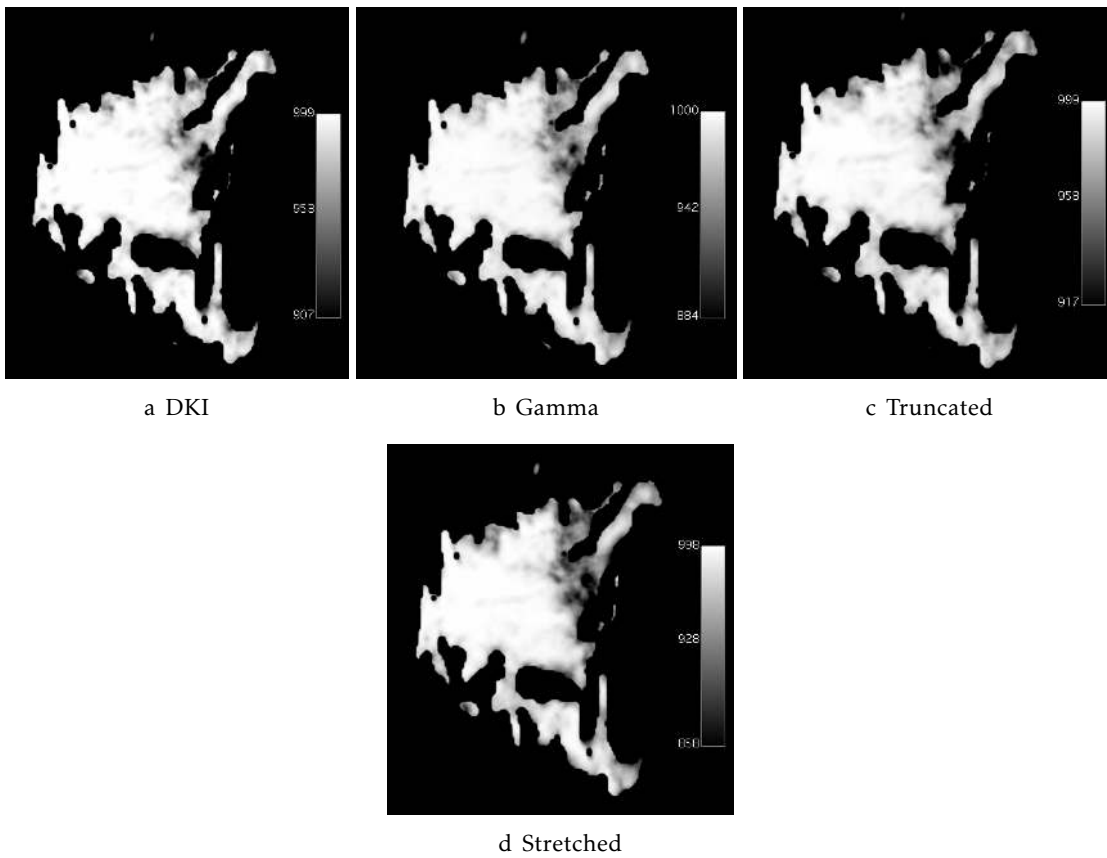


Figure A.1: Goodness-of-fit map (Goodness-of-fit maps (scaling factor of  $1 \times 10^3$ ) for DKI, Gamma, Truncated and Stretched models applied to a breast with a malignant lesion (invasive ductal carcinoma) when the image with the  $b$  value  $600 \text{ s/mm}^2$  was removed.

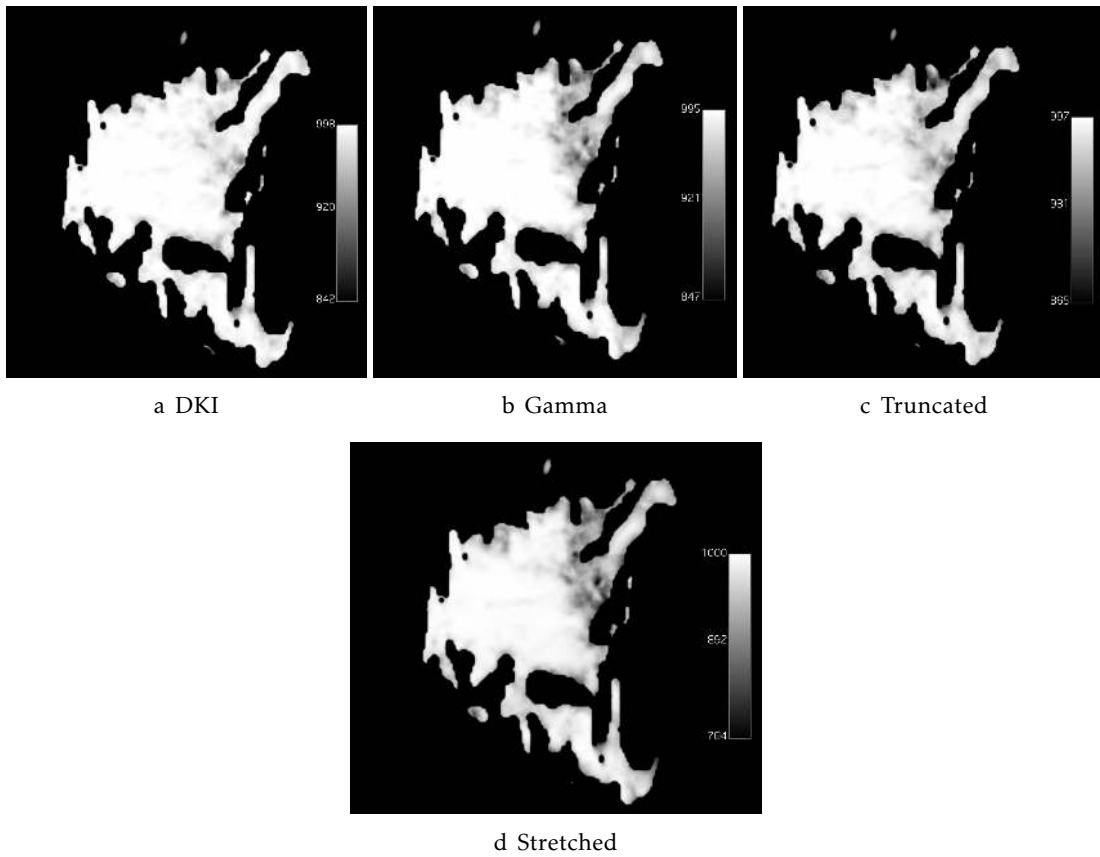


Figure A.2: Goodness-of-fit map (Goodness-of-fit maps (scaling factor of  $1 \times 10^3$ ) for DKI, Gamma, Truncated and Stretched models applied to a breast with a malignant lesion (invasive ductal carcinoma) when the image with the  $b$  value  $2000 \text{ s/mm}^2$  was removed.

#### A.0.4 Goodness of fit maps of the maps with the noise added



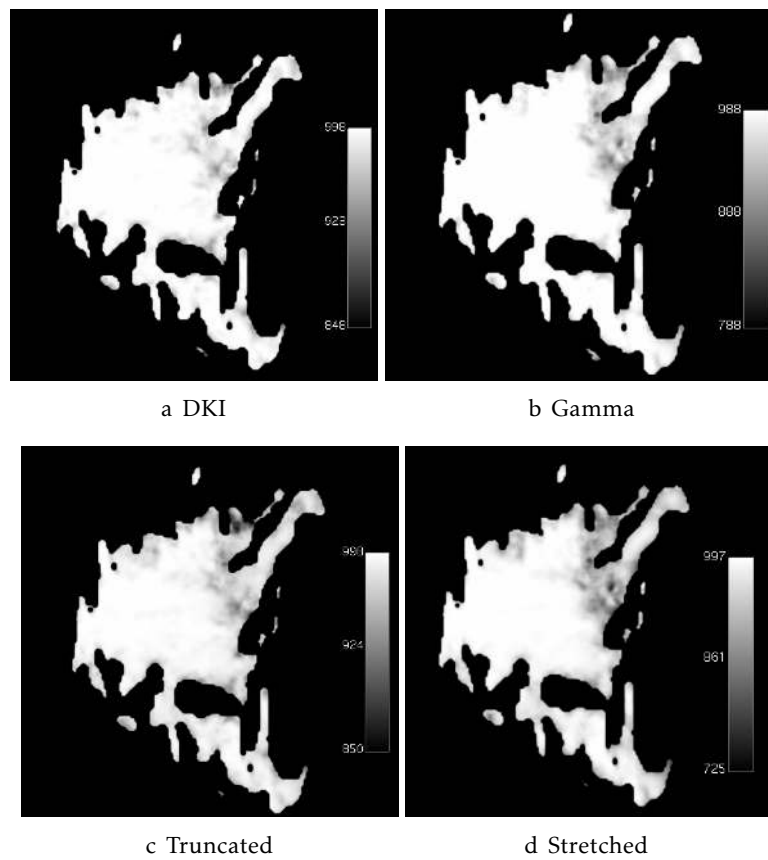


Figure A.3: Goodness-of-fit map (Goodness-of-fit maps (scaling factor of  $1 \times 10^3$ ) for DKI, Gamma, Truncated and Stretched models applied to a breast with a malignant lesion (invasive ductal carcinoma) when the image with the  $b$  value  $200 \text{ s/mm}^2$  was removed.

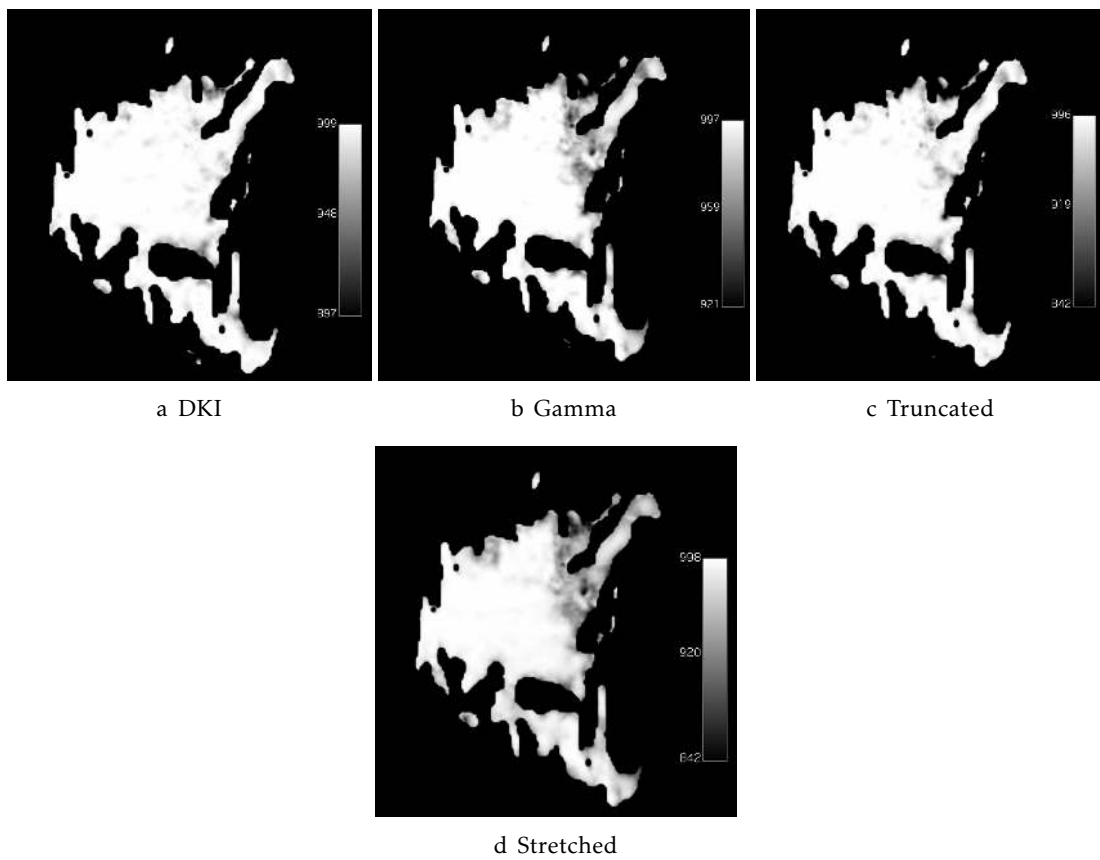


Figure A.4: Goodness-of-fit map (Goodness-of-fit maps (scaling factor of  $1 \times 10^3$ ) for DKI, Gamma, Truncated and Stretched models applied to a breast with a malignant lesion (invasive ductal carcinoma) when the image with the  $b$  value  $800 \text{ s/mm}^2$  was removed.

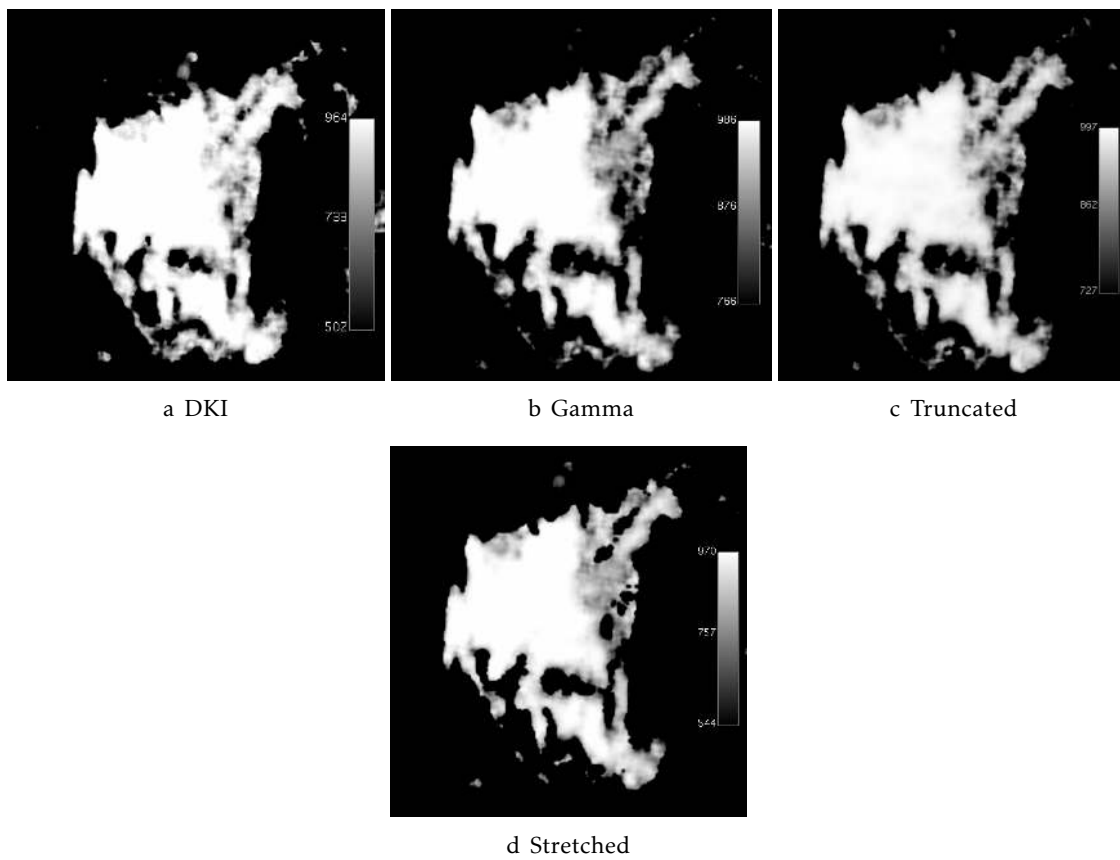


Figure A.5: Goodness-of-fit map (Goodness-of-fit maps (scaling factor of  $1 \times 10^3$ ) for DKI, Gamma, Truncated and Stretched models applied to a breast with a malignant lesion (invasive ductal carcinoma) when noise (10%) is added to the image.

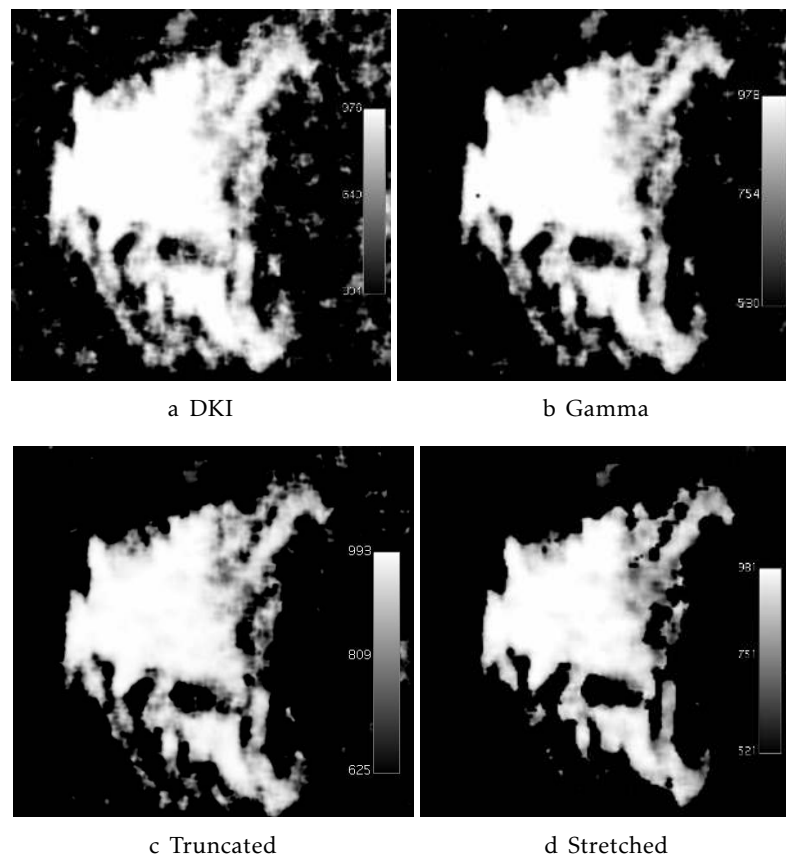


Figure A.6: Goodness-of-fit map (Goodness-of-fit maps (scaling factor of  $1 \times 10^3$ ) for DKI, Gamma, Truncated and Stretched models applied to a breast with a malignant lesion (invasive ductal carcinoma) when noise (15%) is added to the image.

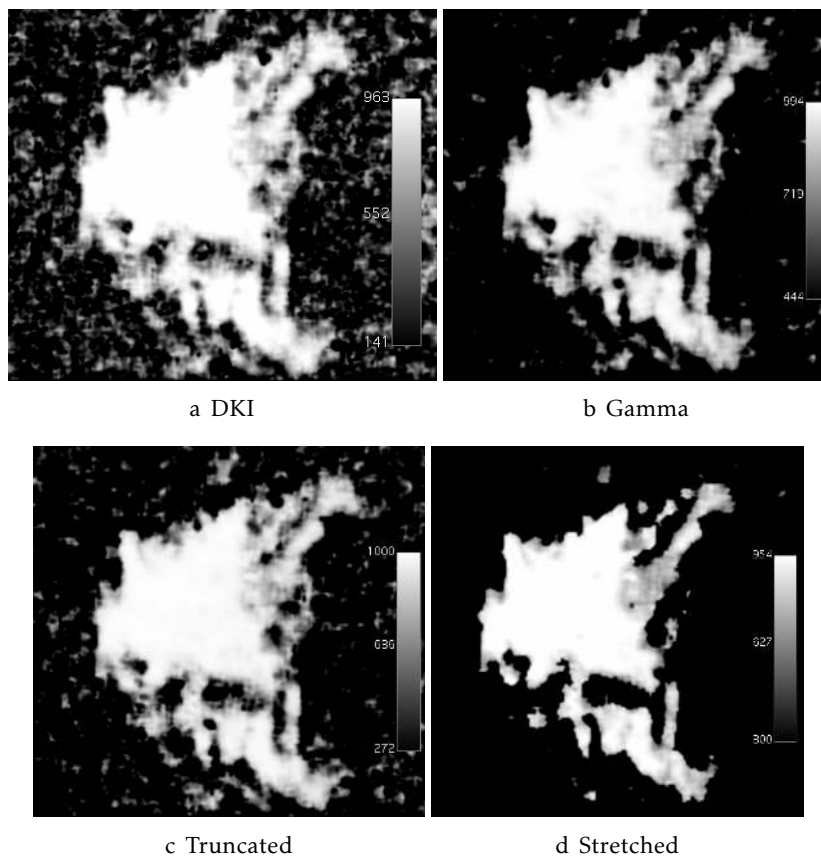


Figure A.7: Goodness-of-fit map (Goodness-of-fit maps (scaling factor of  $1 \times 10^3$ ) for DKI, Gamma, Truncated and Stretched models applied to a breast with a malignant lesion (invasive ductal carcinoma) when noise (20%) is added to the image.

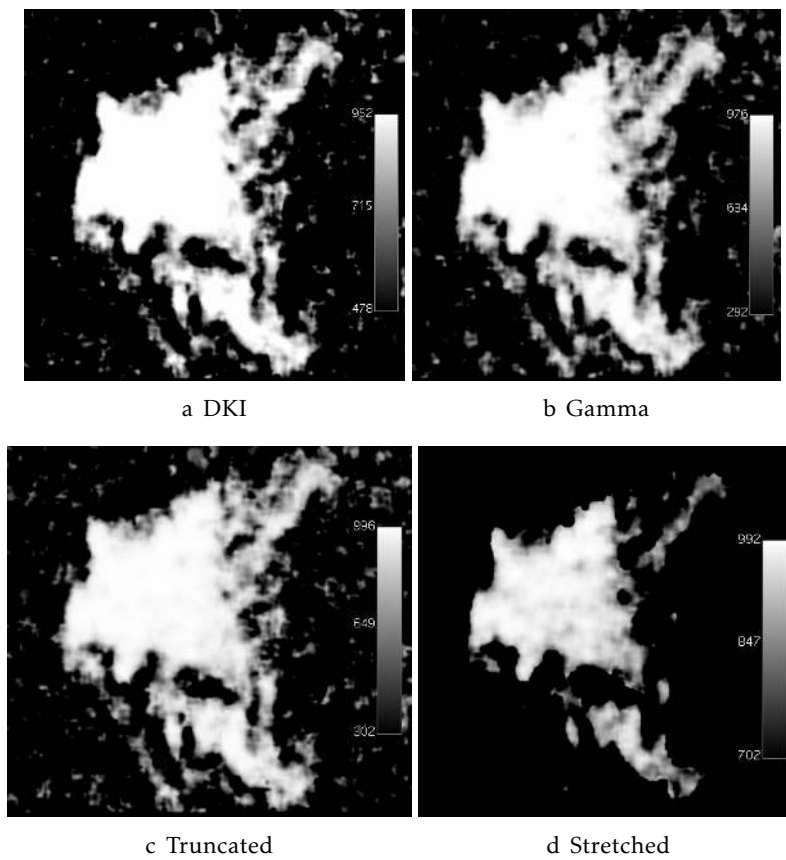


Figure A.8: Goodness-of-fit map (Goodness-of-fit maps (scaling factor of  $1 \times 10^3$ ) for DKI, Gamma, Truncated and Stretched models applied to a breast with a malignant lesion (invasive ductal carcinoma) when noise (25%) is added to the image.

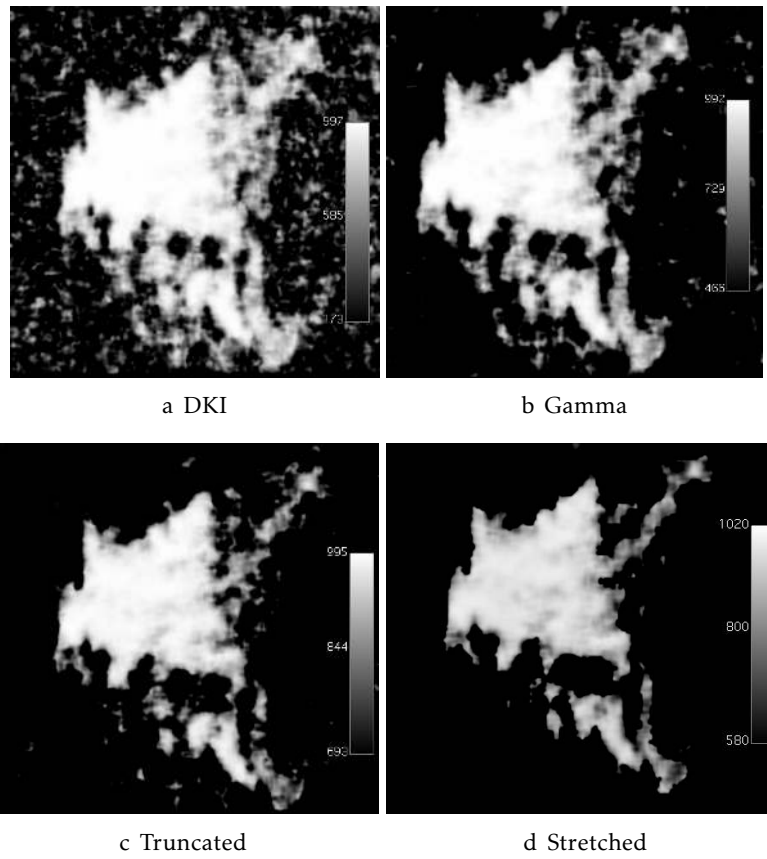


Figure A.9: Goodness-of-fit map (Goodness-of-fit maps (scaling factor of  $1 \times 10^3$ ) for DKI, Gamma, Truncated and Stretched models applied to a breast with a malignant lesion (invasive ductal carcinoma) when noise (30%) is added to the image.

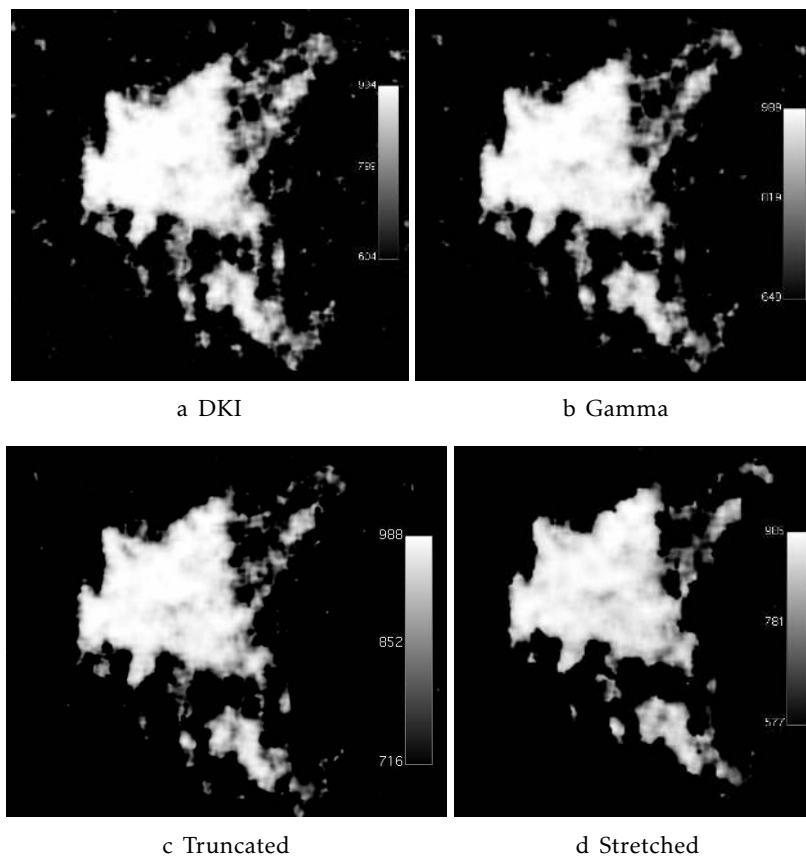


Figure A.10: Goodness-of-fit map (Goodness-of-fit maps (scaling factor of  $1 \times 10^3$ ) for DKI, Gamma, Truncated and Stretched models applied to a breast with a malignant lesion (invasive ductal carcinoma) when noise (35%) is added to the image.



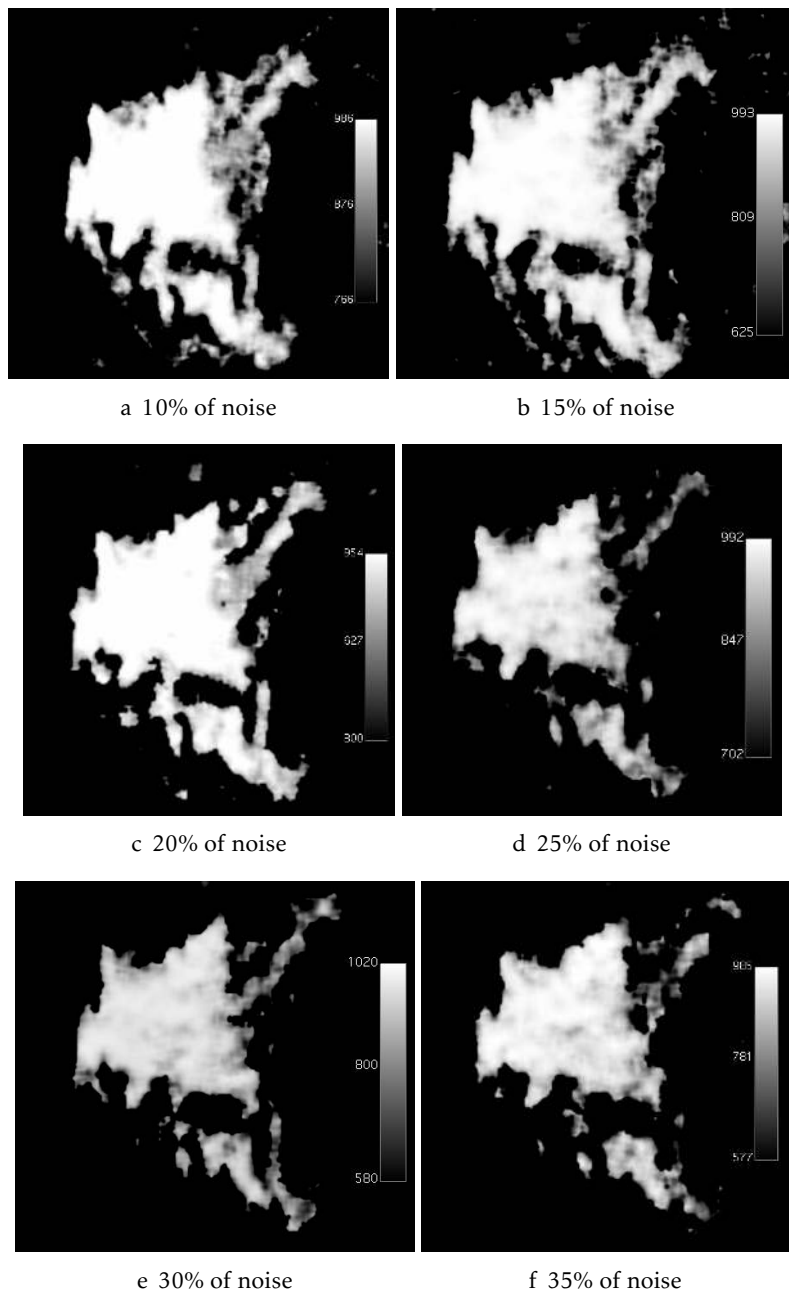


Figure A.11: Goodness-of-fit map (Goodness-of-fit maps (scaling factor of  $1 \times 10^3$ ) for IVIM applied to a breast with a malignant lesion (invasive ductal carcinoma) when several amounts of noise (10%, 15%, 20%, 25%, 30% and 35%) is added to the image.



A P P E N D I X



## POSTER

This appendix contains the poster that was displayed in the 8th Workshop on Biomedical Engineering (WBME) and in the 1st NOVA Biomedical Workshop. This poster was developed in an early stage of the work which explains why the Truncated and Stretched models aren't mentioned.

# Development of an Osirix plug-in for fitting non-gaussian models to diffusion MRI data: application to Breast imaging.

Carolina Amorim<sup>1</sup>, Rita G. Nunes<sup>1</sup>, F. Borlinhas<sup>1</sup>, L. Nogueira<sup>2</sup>, S. Brandão<sup>3</sup>, Hugo A. Ferreira<sup>1</sup>

<sup>1</sup>Instituto de Biofísica e Engenharia Biomédica, Faculdade de Ciências, Universidade de Lisboa, Portugal, <sup>2</sup> Department of Radiology, School of Health Technology of Porto/Polytechnic Institute of Porto, Vila Nova de Gaia, Portugal; <sup>3</sup> MRI Unit, Department of Radiology, Hospital de São João, Porto, Portugal

a.amorim@campus.fct.unl.pt • hugoferreira@campus.ul.pt • rgnunes@fc.ul.pt

## Question

Can we distinguish between malignant and benign tumors using non-gaussian models for diffusion MRI?

## Method

- The non-Gaussian models that will be tested are: diffusional kurtosis imaging (DKI), which is based on the kurtosis excess index which is used to quantify the deviation of the probability displacement function (PDF) from the Gaussian shape (this deviation is directly proportional to tissue microstructure complexity) [4]; intravoxel incoherent motion (IVIM), which is a model which includes the contribution from tissue micro-perfusion and diffusivity requiring multiple diffusion-weighting levels to perform a bi-exponential curve fit [5]; and gamma distribution models, which takes into account the statistical dispersion of the distribution, and the probability distribution shape [6]; among others.
- The models were adapted for Matlab which will work as a standalone application that will be called by the OsiriX plug-in. At first a Wiener filter is applied to help reduce the noise in the image. Then, by applying the Levenberg-Marquardt algorithm to the same image slice with several different b-values, [50,200,400,600,800,1000,2000,3000 s/mm<sup>2</sup>], several parameters can be obtained. These parameters can then be visualized in a parametric map. Parametric maps visually emphasize breast lesions and enable lesion quantitative characterization.

## Background

- Diffusion-weighted imaging (DWI) has become an important tool for breast cancer diagnosis [1].
- Diffusion parameters have been shown to help distinguish between normal fibroglandular tissue and lesions. The standard mono-exponential model is based on the premise that the water molecule displacement in the microenvironment follows a Gaussian distribution. However, biological tissues present compartmentalization that restricts the free displacement of water molecules. As non-Gaussian models can describe the deviation from free diffusion, the study of these models becomes crucial for *in vivo* DWI [2].
- This work aims to develop a plugin for OsiriX, a well-known clinical medical imaging software, to allow the analysis of non-Gaussian diffusion magnetic resonance imaging (MRI) data [3].**

## Parametric Maps

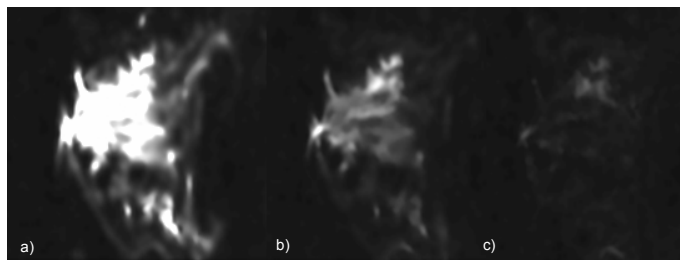


Figure 1: Breast MRI images with the application of a Wiener filter to reduce noise. a) b=50 s/mm<sup>2</sup> b) b=1000 s/mm<sup>2</sup> c) b=3000 s/mm<sup>2</sup>

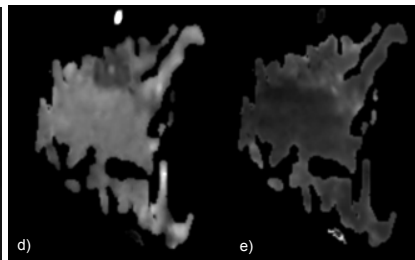


Figure 2: Maps of the parameters of the kurtosis model. d) MD map e) MK map

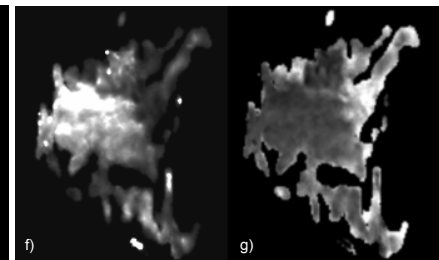


Figure 3: Maps of the parameters of the gamma distribution model. f)  $\theta$  (scale) map g)  $k$  (shape) map

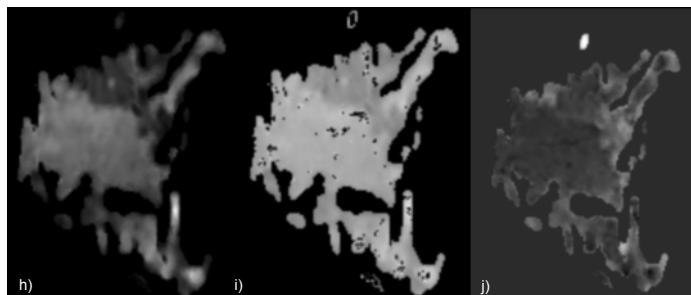


Figure 4: Maps of the parameters of the IVIM model. h) D map i) D\* map j) perfusion fraction map

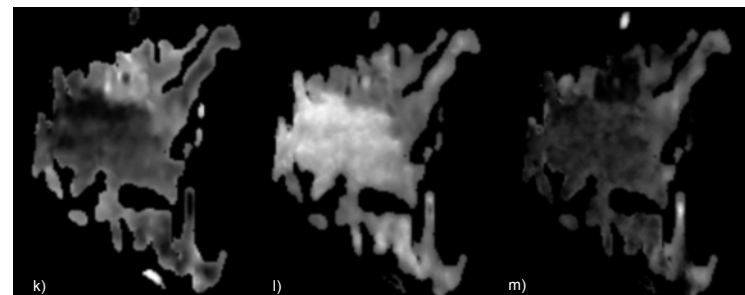


Figure 5: Gamma distribution-derived maps. k) intracellular diffusion, l) extracellular diffusion, and m) perfusion fractional maps.

## Results

- Both the kurtosis and gamma distribution models are detecting the malignant lesion in the images that were tested. Additionally, the gamma distribution of ADC values in each voxel was used to estimate three maps (Figure 5). The first one represents the intracellular diffusion fraction, the second one represents the extracellular diffusion fraction and the last one represents the perfusion fraction.
- Because the IVIM model takes into account tissue micro-perfusion, the b values of the MRI images should be lower than the ones that were used here. Nevertheless, the D\* map and the perfusion fraction map were still able to identify the lesion.
- In order to determine quantitatively whether the model fits were adequate, we resorted to the R squared measure of goodness of fit. This method returns a value from 0 to 1 of the goodness of fit per pixel. Resulting matrices were observed to hold values no smaller than 0.50.

## Conclusions

- Based on non-gaussian models, the plugin is capable of calculating various parametric maps that help identify lesions and quantify differences between benign and malignant breast lesions.**

## References

- [1] Partridge, Savannah C., and Elizabeth S. McDonald. "Diffusion Weighted Magnetic Resonance Imaging of the Breast." *Magnetic Resonance Imaging Clinics of North America* 21.3 (2013): 601-24. Web.
- [2] Wu, Dongmei, Guanwu Li, Junxiang Zhang, Shixing Chang, Jiani Hu, and Yongming Dai. "Characterization of Breast Tumors Using Diffusion Kurtosis Imaging (DKI)." *PLoS ONE* 9.11 (2014)
- [3] Pixmeo SARL, "OsiriX - DICOM Viewer." [Online]. Available: <http://www.osirix-viewer.com/index.html>. [Accessed: 30-Jan-2015].
- [4] Nogueira, Luísa, Sofia Brandão, Eduarda Matos, Rita Gouveia Nunes, Joana Loureiro, Isabel Ramos, and Hugo Alexandre Ferreira. "Application of the Diffusion Kurtosis Model for the Study of Breast Lesions." *Eur Radiol European Radiology* 24.6 (2014): 1197-203.
- [5] Liu, Chunling, Changhong Liang, Zaiyi Liu, Shuixing Zhang, and Biao Huang. "Intravoxel Incoherent Motion (IVIM) in Evaluation of Breast Lesions: Comparison with Conventional DWI." *European Journal of Radiology* 82.12 (2013)
- [6] Borlinhas, Filipa, Luísa Nogueira, Sofia Brandão, Rita G. Nunes, Joana Loureiro, Isabel Ramos, and Hugo A. Ferreira. "Gamma Distribution Model in Breast Cancer Diffusion-weighted Imaging." 2015 IEEE 4th Portuguese Meeting on Bioengineering (ENBENG) (2015)

## Acknowledgements

Research supported by Fundação para a Ciência e Tecnologia (FCT) and Ministério da Ciência e Educação (MCE) Portugal (PIDDAC) under the grant UID/BIO/00645/2013.